ELECTRON FIELD EMISSION IN NANOSTRUCTURES:
A FIRST-PRINCIPLES STUDY

By

Joseph Andrew Driscoll

Dissertation

Submitted to the Faculty of the

Graduate School of Vanderbilt University

in partial fulfillment of the requirements

for the degree of

DOCTOR OF PHILOSOPHY

in

Physics

May, 2011
Nashville, Tennessee

Approved:

Professor Kálmán Varga

Professor Charles Brau

Professor Sokrates Pantelides

Professor Ronald Schrimpf

Professor Sait Umar

To my daughter, Abigail

ACKNOWLEDGEMENTS

Many people deserve thanks for helping me to complete this work. I thank my family for the love and support they have given me throughout my life. I especially thank my wife, Alice, for her encouragement and understanding during this long process. My advisor Prof. Kálmán Varga has given me years of support and advice, for which I am very grateful. From him I have learned a great deal. I also thank Dr. Sergiy Bubin and Brandon Cook for our collaborations and friendship. Working with the group of Prof. Sokrates Pantelides has been a privilege, and I have learned much from them. I thank Prof. Ronald Schrimpf and Prof. Sait Umar for serving on my committee and providing very useful advice. Finally, I want to thank Prof. Charles Brau and Dr. Jonathan Jarvis for many valuable discussions related to their experimental work on field emission. This work has been supported by NSF grants ECCS0925422 and CMMI0927345.

TABLE OF CONTENTS

Page

DEDICATION . . . iii

ACKNOWLEDGEMENTS . . . iv

LIST OF TABLES . . . viii

LIST OF FIGURES . . . ix

Chapter

I. INTRODUCTION . . . 1

- 1.1. Electron sources . . . 1
- 1.2. Electron field emission . . . 2

II. ELECTRONIC STRUCTURE CALCULATIONS . . . 6

- 2.1. The electronic structure problem . . . 6
- 2.2. Density functional theory . . . 9
  - 2.2.1. Pseudopotentials . . . 14
  - 2.2.2. The Kohn-Sham procedure . . . 14
    - 2.2.2.1. Convergence of the ground state . . . 16
- 2.3. Time-dependent density functional theory (TDDFT) . . . 17
- 2.4. Time propagation . . . 19
- 2.5. Calculation of the current . . . 21
- 2.6. Limitations . . . 22

III. BASIS FUNCTIONS . . . 24

- 3.1. Plane waves . . . 25
- 3.2. Atomic orbitals . . . 27
- 3.3. Real space grids . . . 30
  - 3.3.1. Finite differences . . . 32
  - 3.3.2. Lagrange functions . . . 38
  - 3.3.3. Extension to three dimensions . . . 46
- 3.4. Box basis functions . . . 50
- 3.5. Basis set dependence in quantum transport calculations . . . 51
  - 3.5.1. Calculation of the transmission coefficient . . . 55
  - 3.5.2. Results . . . 58
- 3.6. Summary . . . 67

IV. COMPLEX ABSORBING POTENTIALS 68
    4.1. An introduction to complex potentials via 1D scattering . . 68
        4.1.1. Calculating the wavefunction and transmission coefficient 72
        4.1.2. Form of the complex potentials 76
    4.2. Further tests of complex potentials: calculation of self-energy matrices for transport calculations 77
        4.2.1. Self energies of the leads with CAP 80
        4.2.2. Results 83
            4.2.2.1. Conductance of monoatomic aluminium wire 84
            4.2.2.2. Conductance of monoatomic C wire between Al leads 86
            4.2.2.3. Conductance of carbon nanotubes 87
    4.3. Summary 89

V. NANOSTRUCTURES AND FIELD EMISSION 90
    5.1. Field emission 90
        5.1.1. Types of electron emission 90
        5.1.2. Theoretical models 91
            5.1.2.1. Fowler-Nordheim theory 91
            5.1.2.2. Beyond Fowler-Nordheim 94
        5.1.3. Geometric field enhancement 95
        5.1.4. Resonant tunneling and adsorbates 98
    5.2. Nanotubes 100
        5.2.1. Adsorbate effects in nanotube field emission 104
            5.2.1.1. Positions of the adsorbates 105
            5.2.1.2. Methods 106
            5.2.1.3. Results 107
            5.2.1.4. Summary 112
        5.2.2. Laser-enhanced field emission 113
            5.2.2.1. Adding a laser to TDDFT 114
            5.2.2.2. Results 116
            5.2.2.3. Summary 124
        5.2.3. Nanotubes of varying composition 124
            5.2.3.1. Generation of coordinates 125
            5.2.3.2. Results 126
            5.2.3.3. Summary 133
        5.2.4. Spin-polarized field emission from nanotubes 136
            5.2.4.1. Extension of the code for spin-polarization . 140
            5.2.4.2. Structural coordinates 141
            5.2.4.3. Results 142
            5.2.4.4. Summary 145
    5.3. Field emission from nanowires 146

5.4. Graphene 152
    5.4.1. Field emission from graphene nanoribbons 154

VI. SUMMARY 159

5.1. Comparison with experiment 162

REFERENCES 164

LIST OF TABLES

Table Page

III.1. Higher-order finite difference coefficients for the first derivative . . . 36

III.2. Higher-order finite difference coefficients for the second derivative . 36

III.3. Convergence of conductance (in units of G_0). N_C and N_L denotes the basis dimension in the central region and in the unit cell of the lead. 60

V.1. Field emission current for (5,5) capped nanotubes with various adsorbate atoms in a 1 V/Å electric field. 107

V.2. Maximum current values obtained with a static field of 0.1 V/Å only and with the static field and a laser pulse of 1.0 V/Å amplitude. All values are in μA. 124

V.3. Peak field emission currents (in μA) for (5,5) capped nanotubes with differing composition in varying electric fields. 129

LIST OF FIGURES

Figure Page

I.1. Field emission pattern from [1]. 3

I.2. Field emission energy spectrum. From [2]. 3

II.1. Flowchart of the DFT calculation 15

II.2. Change in total energy and density vs. iteration, showing convergence. 17

III.1. Lagrange functions of Equation 3.58 for N=10. The upper panel show the basis functions for $i = 1$ (solid line) and $i = 5$ (dashed line). The lower panel shows the complete set of functions. 47

III.2. Computational cell with a 3D grid. 49

III.3. Structure of the Al-C-Al system, showing division into boxes for the box basis. 50

III.4. Organization of the system into left/right leads (L/R) and a central device (C). The self-consistent potential is calculated for the central region between the planes. Only a few layers of the leads need to be included to obtain a converged potential for the central region. . . 55

III.5. Structure of the Au-CO system. The division into lead and device regions, displayed generally in Figure III.4, is shown. 58

III.6. Transmission vs. relative energy using an atomic orbital basis. In this plot, both the ground state and the conductance calculations were performed on the same AO basis ($p_{max} = 1$ blue dot-dashed line, $p_{max} = 2$ red dashed line, $p_{max} = 3$ black solid line). 60

III.7. Transmission vs. relative energy using an atomic orbital basis. In contrast with Figure III.6, here the ground state potentials for all curves were the same, calculated with a Lagrange basis for high accuracy. 62

III.8. Same as Figure III.7, except that the atomic orbital bases used were spatially smaller. 63

III.9. Transmission calculation with the Gaussian-augmented AO basis. For $p_{max} = 2$ the transmission is calculated with (dashed red line) and without (solid black line) the addition of a uniform grid of Gaussian basis functions. 64

III.10. Convergence of the transmission using box basis states. The curves correspond to the number of box basis states as defined by sets 1 (blue dot dashed line), 2 (red dashed line) and 3 (black solid line) in Table III.3 (Case III). The results obtained by using larger basis sets (4 and 5 in Table III.3) are identical with the black solid line within the resolution of the figure. 65

III.11. Comparison of the results obtained by the box basis (solid black line) and the AO (dashed red line). 65

III.12. Comparison of the box basis calculation (solid black line) to benchmark results. The blue dot dashed line is the Wannier, the red dashed line is the AO calculation of Ref. [3]. 66

IV.1. Use of complex potentials with a scattering potential. The solid line represents a scattering potential, while the dashed lines indicate pure imaginary potentials. These imaginary potentials absorb the wavefunction in asymptotic regions, allowing a finite representation of the scattering problem. 69

IV.2. Complex absorbing potential in a one-dimensional scattering example. 77

IV.3. Schematic diagram of a two-probe device. The device is modeled by two semi-infinite electrodes (L and R) and a central region (C). The electrodes are divided into principal layers (blocks) that interact only with the nearest-neighbor layers. 78

IV.4. Transmission probability of a monoatomic Al wire. The result obtained by the decimation method (solid black line) is compared to the CAP of different ranges (blue dashed line two blocks, red dotted line four blocks). The CAP results using six blocks is indistinguishable from the decimation results within the line width on the figure. 85

IV.5. Transmission probability of a 7 atom monoatomic C wire sandwiched between Al(100) electrodes. The result obtained by the decimation method (solid red line) is compared to the CAP result (solid blue line) obtained by using 6 lead blocks. 86

IV.6. Transmission probability of a (10,10) carbon nanotube. The decimation and CAP results are in perfect agreement. 87

IV.7. Transmission probability of a (5,5) carbon nanotube using the Hückel Hamiltonian. 88

V.1. One-dimensional confining potential under different electric field strengths. 92

V.2. Field emission current vs. time for a multiwall nanotube, with and without adsorbates. The presence of adsorbates causes the current to increase, and a corresponding bright spot on a phosphor screen is visible. From [4]. 99

V.3. A multiwall nanotube with and without adsorbates. The presence of adsorbates causes the current to increase, and a corresponding bright spot on a phosphor screen is visible. From [5]. 99

V.4. Real space lattice vectors of graphene. The shaded area marks the unit cell. 101

V.5. Examples of nanotubes with varying chirality. 102

V.6. Hexagonal structure of graphene before being rolled up into a nanotube. 103

V.7. A capped (5,5) carbon nanotube with an adsorbate atom. 105

V.8. Enlargement of the cap region of a carbon nanotube with a tungsten adsorbate. 106

V.9. Current vs. electric field magnitude for no tip and a W tip. 109

V.10. Current vs. energy, relative to Fermi energy 109

V.11. Two-dimensional spatial pattern of field emission intensity at an electric field magnitude of 1.0 V/Å, for various tips. 110

V.12. Current vs. energy, relative to Fermi energy, for the no-tip case. . . 111

V.13. Fowler-Nordheim plot for no tip and a W tip. 112

V.14. The $C_{12}H_{14}$ molecule used in the calculations. 116

V.15. Simulation box containing a $C_{12}H_{14}$ molecule. The emission current is measured through planes some distance away from the molecule. The space on the right of the measurement planes is the region where the complex absorbing potential acts. 116

V.16. Field emission from a $C_{12}H_{14}$ molecule due to static electric and laser fields acting together (top) and the laser pulse as a function of time (bottom). The currents shown are computed 10 Å from the right end of the molecule. 118

V.17. The (3,3) nanotube used in the calculations. 120

V.18. The (5,5) nanotube used in the calculations. 120

V.19. Change in density vs. time around the (5,5) nanotube, at a field strength of 1.00 V/Å. 121

V.20. Change in density around the (5,5) nanotube vs. time, using a larger box. Red indicates increases in density while blue shows decreases. 122

V.21. Field emission from a (5,5) carbon nanotube due to static electric and laser fields acting together (top) and the laser pulse as a function time (middle). The bottom figure shows the energy of the highest occupied orbital as a function of time. 123

V.22. Relaxed structures for the (a) BN and (b) C nanotube used in the calculations. 127

V.23. Relaxed structures for the (a) GaN and (b) Si nanotube used in the calculations. 128

V.24. Relaxed structure for the SiC nanotube used in the calculations. . . 129

V.25. Current vs. time for nanotubes of varying composition at the field strength of 1.00 V/Å. 130

V.26. Potential profile for 120 atom C nanotube at different electric field strengths. 131

V.27. Potential profile for various nanotubes at the field strength of 1.00 V/Å. 132

V.28. Density profile for the different nanotubes at the field strength of 1.00 V/Å. 133

V.29. Current vs. energy, relative to Fermi energy, for the (a) BN and (b) C nanotubes at the field strength of 1.00 V/Å. The spectral peaks were broadened with Gaussians, using a full width at half-maximum of 0.2 eV. 134

V.30. Current vs. energy, relative to Fermi energy, for the (a) GaN and (b) Si nanotubes at the field strength of 1.00 V/Å. The spectral peaks were broadened with Gaussians, using a full width at half-maximum of 0.2 eV. 135

V.31. Current vs. energy, relative to Fermi energy, for the SiC nanotube at the field strength of 1.00 V/Å. The spectral peaks were broadened with Gaussians, using a full width at half-maximum of 0.2 eV. . . . 136

V.32. Orbital localization vs. energy, relative to Fermi energy, for the (a) BN and (b) C nanotubes at a field strength of 1.00 V/Å. 137

V.33. Orbital localization vs. energy, relative to Fermi energy, for the (a) GaN and (b) Si nanotubes at a field strength of 1.00 V/Å. 138

V.34. Orbital localization vs. energy, relative to Fermi energy, for the SiC nanotube at a field strength of 1.00 V/Å. 139

V.35. Structure of the Fe_4 cluster used in the calculations. The coordinates used were obtained from Ref. [6]. 141

V.36. Structure of a (3,3) carbon nanotube without iron adsorbates. . . . 141

V.37. Structure of a (3,3) carbon nanotube with an Fe atom adsorbed on the side. 142

V.38. Structure of a (3,3) carbon nanotube with an Fe_4 cluster adsorbed on the side. 142

V.39. Spin-polarized field emission current vs. time for a (3,3) carbon nanotube with no adsorbates. The applied electric field magnitude was 1.0 V/Å. The up and down currents are indistinguishable for this non spin-polarized structure. 143

V.40. Spin-polarized field emission current vs. time for a (3,3) carbon nanotube with an adsorbed Fe atom. The applied electric field magnitude was 1.0 V/Å. 144

V.41. Spin-polarized field emission current vs. time for a (3,3) carbon nanotube with an Fe_4 cluster adsorbate. The applied electric field magnitude was 1.0 V/Å. 144

V.42. Difference between spin-up and spin-down field emission current vs. time for a (3,3) carbon nanotube with an Fe atom and an Fe_4 cluster adsorbed on the side. The applied electric field magnitude was 1.0 V/Å. 145

V.43. Total field emission current vs. time for a (3,3) carbon nanotube with and without iron adsorbates. The applied electric field magnitude was 1.0 V/Å. 146

V.44. Spin-up field emission current vs. time for a (3,3) carbon nanotube with an Fe atom and an Fe_4 cluster adsorbed on the side. The applied electric field magnitude was 1.0 V/Å. 147

V.45. Spin-down field emission current vs. time for a (3,3) carbon nanotube with an Fe atom and an Fe_4 cluster adsorbed on the side. The applied electric field magnitude was 1.0 V/Å. 148

V.46. A carbon nanowire passivated with hydrogen atoms. 148

V.47. The $C_{12}H_{14}$ molecule used in the calculations. 151

V.48. Field emission current from a $C_{12}H_{14}$ molecule at varying electric fields. 152

V.49. A portion of a graphene sheet. The structure continues far away in the in-plane directions. 153

V.50. Structure of a (3,3) carbon nanotube with passivating hydrogens. . 154

V.51. Structure of a (3,3) carbon nanotube without passivating hydrogens. 155

V.52. Structure of a (3,3) graphene nanoribbon with passivating hydrogens. 155

V.53. Structure of a (3,3) graphene nanoribbon without passivating hydrogens. 155

V.54. Field emission current vs. time for a (3,3) hydrogen-terminated graphene nanoribbon. Curves for three different applied electric fields are shown. 156

V.55. Field emission current vs. time for a (3,3) hydrogen-terminated carbon nanotube. Curves for three different applied electric fields are shown. 156

V.56. Field emission current vs. time for a (3,3) graphene nanoribbon. Curves for three different applied electric fields are shown. 157

V.57. Field emission current vs. time for a (3,3) carbon nanotube. Curves for three different applied electric fields are shown. 157

CHAPTER I

INTRODUCTION

The rapidly developing field of nanoscience has revealed new physical phenomena and encouraged the development of novel technological applications. Both require development of new theoretical frameworks to describe them, and computational advances to effectively use them. This dissertation presents a first-principles study of electron field emission in various nanostructures using time-dependent density functional theory (TDDFT) [7]. In addition to the theoretical calculations, the work has included substantial computational developments necessary to allow these first-principles methods to be applied to systems which include many atoms and are simulated for relatively long time periods. The next section introduces the major types of electron sources. This is followed by a discussion of issues specific to electron field emission. The chapter concludes with an outline of the rest of the dissertation.

1.1 Electron sources

Electrons in a material are confined to it by a potential. In order for electrons to escape the material, they must somehow move beyond the potential barrier. If this barrier is lowered by the application of an external electric field, the electrons can then tunnel out of the material. This process is called electron field emission (FE) [8]. Thermionic electron emission [9] relies on heating a material to the point at which electrons gain enough energy to be emitted. Schottky emitters [10, 11] combine thermionic emission with electric field-based lowering of the material's work function. This lowering, called the Schottky effect [12], makes it easier for thermally excited electrons to escape the material.

Disadvantages with thermionic emission include large power consumption and potential damage to the device due to heating [13]. While field emitters do not directly use heating to emit electrons, typical materials used in field emission can become damaged due to current-induced heating. Using a material such as a carbon nanotube helps [13], since it is more robust to such effects. In addition, field emitters can respond to varying electric fields much faster than a thermionic emitter can alter its output, meaning that field emitters are capable of operation at higher frequencies [14].

Compared with thermionic emission, nanotube field emitters produce a narrow beam size [15], which is important for high-resolution displays and spatial microscopy. When projected onto a screen, the spatial pattern contains pentagonal structures [1], as shown in Figure I.1. In addition, interference fringes can be seen that may be due to interfering electron waves. The electrons emitted from a nanotube exhibit a narrow energy spectrum [2] which is important in, e.g., energy-resolved microscopy; see Figure I.2. Here the measured spectral width (central plot) is significantly narrower than theoretical predictions (other lines).

1.2 Electron field emission

Field emission of electrons from nanostructures is the subject of intense experimental and theoretical research [8, 16, 17, 18, 19, 20, 15, 21]. The aim of these studies

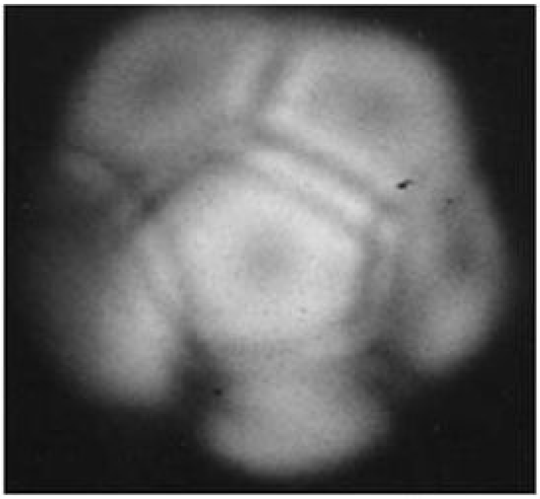

Figure I.1: Field emission pattern from [1].

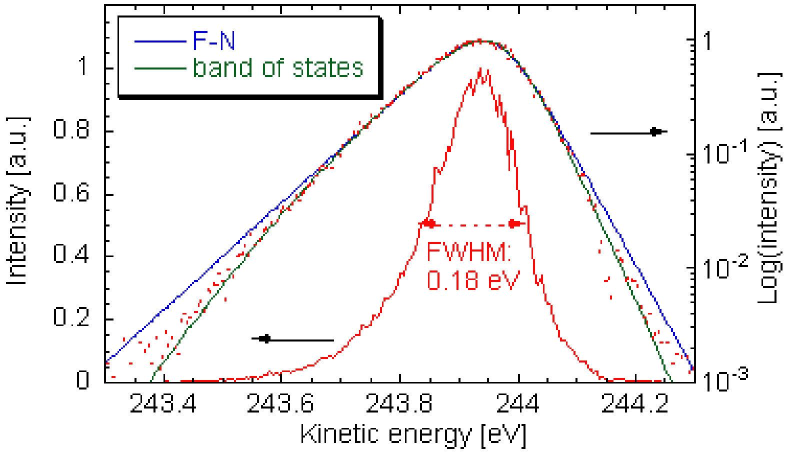

Figure I.2: Field emission energy spectrum. From [2].

is to explore the properties of nanoscale materials in electric fields and exploit these properties for technological applications. Emission from carbon nanotubes (CNs) is particularly important as CNs are candidates for next-generation displays, electron sources [8, 16, 17, 18], and high-resolution electron beam instruments [19, 20, 15, 21].

Structural defects, adsorbates, encapsulated atoms and other variations in the atomic structure significantly change the FE properties of CNs [22, 23, 24, 25, 26, 27, 28, 29]. Experimental studies investigating the effects of adsorbates on field emission have shown that adsorbates strongly influence the field emission current [22, 23, 24, 25, 26, 27]. For example, experiments have shown that a Cs adsorbate can significantly increase the FE current [28, 29]. Other adsorbates such as CH_4 and CO molecules can increase or decrease the field emission current [26, 27]. Effects such as these can be useful for applications, and much theoretical work (see below) is devoted to understanding these properties and predicting new ones.

The theoretical study of field emission dates back to the early days of quantum mechanics. The standard approach to modeling field emission is the Fowler-Nordheim (FN) theory [30] which describes the emission of electrons from a flat metal surface in the presence of an electric field. The FN approach allows one to calculate the current density of field emitted electrons. Applied to nanotubes, some aspects of the experimental data can be modeled in this way [31]. But in other cases, for example with high fields or adsorbates, the theory fails to describe the phenomena [32]. This is not surprising, since FN is a model with various assumptions (e.g., clean metal surface) that do not match the situation with nanotubes.

More rigorous methods that take into account atomic geometry and electronic structure have been developed in recent years [33, 34, 35, 36] including first-principles calculations [37, 38]. The first-principles approaches calculate the self-consistent electronic structure of the field emitter and connect the wave function to the asymptotic scattering wave function of the electrons in the external field [34, 35]. An important step beyond the static calculations is the introduction of the time-dependent description of FE [37, 38]. The time-dependent description so far has been limited to time propagation of the wave functions with a time-independent ground state Hamiltonian.

The present work goes beyond previous time-dependent approaches [37, 38] and simulates the entire field emission process in a real time, real space framework. In the time-dependent approach the wave function is time propagated to describe the effect of the electric field. This approach has several advantages. In the time-independent approach, the wave function has to be matched to the asymptotic wave function. The asymptotic wave function, the wave function of electrons in an electric field, is not known. It is usually approximated by Airy functions, the wave functions of independent, non-interacting electrons in an electric field. This approximation is avoided in the time-dependent approach: the field-emitted electrons and the electrons of the nanotube are described on an equal footing. The asymptotic form of the wave function is not needed in the calculation, and the time evolution of the wave function is used to describe the emitted current.

This dissertation presents theoretical studies of electron field emission from various nanostructures. Following this introduction, Chapter II presents the theoretical framework for our calculations. To implement this framework computationally, a basis must be chosen: These considerations are discussed in the Chapter III. Since we chose to use a real-space basis, an important issue is reflections from the boundaries. Our approach to handling this is presented in Chapter IV. Chapter V provides the necessary background in nanostructures and field emission, as well as our results. This chapter describes our computational procedure, including how we slowly turn on the electric field with a linear ramp (see Section 5.2.1.2) to avoid transient effects. Finally, a summary is presented in Chapter VI.

CHAPTER II

ELECTRONIC STRUCTURE CALCULATIONS

Our theoretical approach is to obtain the ground state wavefunction Ψ of the system by solving the time-independent Schrödinger equation

$$H\Psi = E\Psi \tag{2.1}$$

where H is the system's Hamiltonian. We then use time propagation operators (discussed below) to develop the system forward in time and extract quantities of interest, such as the field emission current. This chapter provides an overview of the theoretical methods used to accomplish this.

After a brief review of alternative methods, the chapter presents density functional theory (DFT), which is the core theoretical framework used here. DFT provides the ground state of the system. To move beyond the ground state into time-dependent phenomena such as field emission, we use time-dependent DFT (TDDFT) and the associated time propagation methods. The chapter concludes with a description of how field emission current is calculated from the time-propagated wavefunction.

2.1 The electronic structure problem

A fully quantum mechanical treatment of a nanoscale system requires confronting the many-body Schrödinger equation for all particles. Fortunately, in many physical problems, we can restrict our focus to just the electrons in the system. This is because electrons are much less massive than nuclei and so respond to forces much faster. In addition, the time simulations considered in this dissertation are much shorter than the time scales of nuclear motion. In this case we can use the Born-Oppenhemier approximation [39] which states that the wavefunction of the entire system (electrons and nuclei) is separable into an electron-only part and a nuclei-only part. This allows us to work with just the electronic wavefunction, and this approximation is used for all calculations in this dissertation. If the motion of the nuclei are needed (e.g., when relaxing a molecule's structure), there are approaches that separate the dynamics of the electrons and nuclei, thus preserving the theoretical and computational advantages of this approach.

Even with the fixed-nuclei approximation, we still have a many-electron Schrödinger equation to solve. Solving this equation is impossible in all but simple systems, and the only way to make progress in realistic systems is to make approximations. The various approaches to electronic structure calculations represent different approximations that one may make. We now briefly review some of these methods before turning to a more detailed treatment of density functional theory, which is the approach used here.

In the Hartree method, the many-electron wavefunction Ψ is approximated as a product of N single-electron wavefunctions:

$$\Psi(\mathbf{r_1}, \mathbf{r_2}, \ldots, \mathbf{r_N}) = \phi_\mathbf{1}(\mathbf{r_1})\phi_\mathbf{2}(\mathbf{r_2}) \cdots \phi_\mathbf{N}(\mathbf{r_N}) \tag{2.2}$$

where N is the number of electrons. Using a product assumes that the electrons are independent of each other. More significantly, this approach neglects the fermionic nature of the electrons by not antisymmetrizing the wavefunctions.

The Hartree-Fock method extends the Hartree approach by using an antisymmetrized product of single-electron wavefunctions. Slater [40] showed that an elegant way to accomplish this is to arrange the single-particle wavefunctions in a determinant:

$$\Psi(\mathbf{r_1}, \mathbf{r_2}, \ldots, \mathbf{r_N}) = \frac{\mathbf{1}}{\sqrt{\mathbf{N!}}} \begin{vmatrix} \phi_1(\mathbf{r_1}) & \phi_1(\mathbf{r_2}) & \cdots & \phi_1(\mathbf{r_N}) \\ \phi_2(\mathbf{r_1}) & \phi_2(\mathbf{r_2}) & \cdots & \phi_2(\mathbf{r_N}) \\ \vdots & \vdots & & \vdots \\ \phi_N(\mathbf{r_1}) & \phi_N(\mathbf{r_2}) & \cdots & \phi_N(\mathbf{r_N}) \end{vmatrix} . \tag{2.3}$$

The determinant enforces the antisymmetry requirement since interchanging a row or column of a determinant (which is equivalent to exchanging the positions of the corresponding electrons) changes the sign of the result.

Both the Hartree and Hartree-Fock methods neglect electron correlation [41]. Post Hartree-Fock methods are those approaches that extend the Hartree-Fock method to include electron correlation effects. Two well-known examples are the configuration interaction [42] and coupled cluster [43] methods. With the incorporation of correlation effects, these methods are able to produce impressively accurate results, but at a high computational cost. Due to this, they are not presently practical for use in systems beyond a few tens of atoms. Density functional theory (DFT), discussed next, is able to handle much larger systems.

2.2 Density functional theory

To predict the properties of a quantum system, various observables are calculated. This typically requires the wavefunction, which is obtained by solving the Schrödinger equation. Unfortunately, for a system with multiple electrons such a solution is very difficult due to the coupling in the many-electron Hamiltonian. If instead there was just a single electron interacting with some potential, the Hamiltonian (and the solution) would be simpler. DFT allows one to use this simpler approach and yet still obtain the observables corresponding to the actual many-electron system.

In mathematics, a functional is a function that takes another function as its argument. The name "density functional theory" comes from the fact that various terms in the system's Hamiltonian can be expressed as functionals of the density, as will be shown below.

The electron density $\rho(\vec{r})$ can be obtained from the wavefunction Ψ by integrating over all spatial coordinates except for one [44]:

$$\rho(\vec{r}) = N \int \cdots \int \left|\Psi(\mathbf{r_1}, \mathbf{r_1}, \ldots, \mathbf{r_N})\right|^2 d\mathbf{r_2} \ldots \mathbf{dr_N} \tag{2.4}$$

The central idea of DFT is that one does not need to calculate the many-body wavefunction Ψ. Instead, the electron density $\rho(\vec{r})$ is sufficient. This is a tremendous simplification: The wavefunction describing N electrons depends on $3N$ variables (the three spatial coordinates for each electron), while the electron density is a function of just the three spatial coordinates.

The justification for this simplification comes from the Hohenberg-Kohn (HK) theorems [45]. They prove that there is a one-to-one correspondence between the total electron density and the corresponding wavefunction (and therefore the potential). This means that the density contains the same information as the wavefunction, and so the observables can be calculated using just the density. This avoids the need to find the exact wavefunction.

The HK theorems establish that all one needs is the density, but do not give a method to obtain it. The Kohn-Sham (KS) method [46] provides such a procedure. Consider a simpler problem, in which the electrons do not interact with each other. Each of these “independent” electrons moves in a potential that represents the properties of the system in an average way.

Although this decoupled system has a Hamiltonian that makes the Schrödinger equation simpler to solve, the resulting eigenstates, called Kohn-Sham orbitals, are not eigenstates of the real system. However, the KS method constrains these orbitals such that the density calculated from them matches the actual system’s density, which is all that is needed to calculate system observables. Using the effective potential in the Schrödinger equation produces the Kohn-Sham equations (one equation for each orbital).

Hohenberg and Kohn also proved [45] that the total energy of the electron gas is a unique functional of the electron density. The minimum of the total energy functional is the ground state energy of the system and the density which gives this minimum is the exact single-particle density of the ground state.

The Kohn-Sham total energy functional is

$$E[\phi_i] = 2\sum_i \int \phi_i \left(-\frac{\hbar^2}{2m}\right) \nabla^2 \phi_i d^3\mathbf{r} + \int V^{ion}(\mathbf{r}) n(\mathbf{r}) d\mathbf{r} + \frac{e^2}{2} \int \frac{n(\mathbf{r})n(\mathbf{r}')}{|\mathbf{r}-\mathbf{r}'|} d\mathbf{r} d\mathbf{r}' + E_{XC}[n(\mathbf{r})] + E_{nn}, \quad (2.5)$$

where ϕ_i are electron states,

$$E_{nn} = \sum_{ij} \frac{Z_i Z_j}{|\mathbf{R}_i - \mathbf{R}_j|} \quad (2.6)$$

is the Coulomb energy of the nuclei, V^{ion} is the electron-ion potential, $n(\mathbf{r})$ is the electron density

$$n(\mathbf{r}) = 2 \sum_{i=1}^{N_{occupied}} |\Psi_i(\mathbf{r})|^2, \quad (2.7)$$

and $E_{XC}[n(\mathbf{r})]$ is the exchange-correlation functional. E_{nn} is the energy due to mutual nuclear repulsion. Since we assume fixed nuclei, this energy is constant. In Eq. 2.7 the factor of 2 includes contributions from both up and down spins. We will see in Section 5.2.4 how to extend this formalism for the case of spin polarization. Only the minimum of the energy functional has physical meaning, and at the minimum it gives the ground state energy of the system. By minimizing the above functional one can derive the Kohn-Sham equations. At the minimum, the electronic states ϕ_i are self-consistent solutions of the Kohn-Sham equation

$$H_{KS}\phi_i(\mathbf{r}) = E_i \phi_i(\mathbf{r}), \qquad H_{KS} = -\frac{\hbar^2}{2m}\nabla^2 + V^{KS}[n(\mathbf{r})] \quad (2.8)$$

with

$$V^{KS} = V^{ion}(\mathbf{r}) + V^{H}(\mathbf{r}) + V^{XC}(\mathbf{r}), \tag{2.9}$$

where E_i is the Kohn-Sham eigenvalue, and V^H is the Hartree-potential of the electrons defined as

$$V^{H}(\mathbf{r}) = e^2 \int \frac{n(\mathbf{r}')}{|\mathbf{r} - \mathbf{r}'|} d\mathbf{r}'. \tag{2.10}$$

The exchange-correlation functional, V^{XC} is the functional derivative of the exchange-correlation energy

$$V^{XC}(\mathbf{r}) = \frac{\delta E_{XC}[n(\mathbf{r})]}{\delta[n(\mathbf{r})]}. \tag{2.11}$$

The potential may also contain an applied external field (e.g., from a laser). Note that the Hartree term V^H represents the Coulombic interaction between a single electron and the density due to all other electrons. This density looks the same to all of the electrons, and so this avoids many-body complications. This potential is found by solving the Poisson equation

$$\nabla^2 V^{H}(\mathbf{x}) = -4\pi\rho(\mathbf{x}) \tag{2.12}$$

The KS approach represents the electron-electron Coulombic interaction as a single electron interacting with an effective mean field. One problem with this is that in reality the electrons' movements are correlated: electrons repel one another. Consider a two-electron system; at the position of one electron, the probability of finding the other electron decreases, and vice-versa. The mean field approximation does not take this into account, and so it models a system of electrons that can get too close to one another.

Exchanging the spatial and spin coordinates of two electrons must change the sign of the many-body wavefunction. This leads to the Pauli principle, which causes electrons of like spins to avoid each other (i.e., not be in the same state). Unlike the correlation effect, this exchange effect only applies to electrons of like spins.

The exchange-correlation (XC) term in the potential, V^{XC}, is defined [47] to contain whatever is "left over". That is, the difference between the real and effective potentials, which are mainly quantum effects due to electron exchange and correlation. The theory would be exact if the exchange-correlation energy was explicitly known. In practice, one has to rely on some approximate expression of the exchange-correlation energy. The first, and most simple approximation is the local density approximation (LDA). In the LDA the exchange-correlation energy is assumed to be [41]

$$E_{XC}^{LDA} = \int d\mathbf{r}\ \epsilon[n(\mathbf{r})]n(\mathbf{r}), \tag{2.13}$$

where $\epsilon[n(\mathbf{r})]$ is the exchange-correlation energy per unit volume of a homogeneous electron gas of density $n(\mathbf{r})$.

Once the KS orbitals are determined, the total energy can be obtained from Eq. 2.5, but this formula can be simplified. By using the KS equation one can derive the following equation for the total energy:

$$E[\phi_i] = \sum_{i=1}^{N_{occupied}} E_i + \int d\mathbf{r} \left(\frac{1}{2}V^H(\mathbf{r}) + V^{XC}(\mathbf{r})\right) n(\mathbf{r}) + E_{XC}[n] + E_{nn}. \tag{2.14}$$

2.2.1 Pseudopotentials

The treatment of the many-electron system can be simplified further by introducing the pseudopotential concept. By dividing the electrons of the atoms into core electrons and valence electrons and assuming that the core electrons only play a passive role, the ion-valence electron interaction can be described in terms of pseudopotentials [48]. The pseudopotential concept removes the core electrons and replaces the strong ionic potential by a weaker potential called the "pseudopotential". The simplest and most popular form of pseudopotentials is the Kleinman and Bylander form [49]

$$V^{ion}(\mathbf{r}) = V^{ps,local}(\mathbf{r}) + \sum_{l} \sum_{m=-l}^{l} \frac{\phi_{lm}(\mathbf{r})\Delta w_l(r)\Delta w_l(r')\phi_{lm}(\mathbf{r}')}{\int d\mathbf{r}\phi_{lm}(\mathbf{r})\Delta w_l(r)\phi_{lm}(\mathbf{r})} \tag{2.15}$$

where $\Delta w_l(r) = w_l(r) - V^{ps,local}(r)$. The functions w_l, $V^{ps,local}$ and ϕ_{lm} are determined by solving the Schrödinger equation, projecting out the core states, and deriving a potential for the valence states. This potential should preserve the scattering properties and be transferable, that is, accurately describe the valence electrons in different chemical environments. Note that pseudopotentials are a general theoretical tool, and are not limited to use in DFT.

2.2.2 The Kohn-Sham procedure

In order to calculate the potential, one needs the density since parts of the potential are density functionals. The density is calculated from the KS orbitals. But the KS orbitals are found by solving the Schrödinger equation, whose Hamiltonian needs the potential. This coupling requires the use of a self-consistent iterative solution method. Fig. II.1 shows a typical flowchart of the self-consistent calculations of the

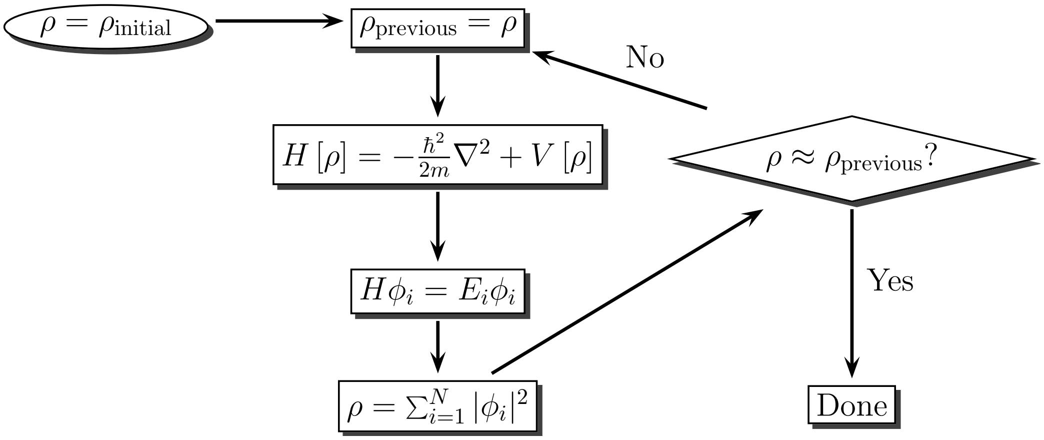

Figure II.1: Flowchart of the DFT calculation

Kohn-Sham states ϕ_i. The initial density $n_0(\mathbf{r})$ is usually taken as the sum of atomic densities. The KS equation is then solved self-consistently. The self-consistency cycle is stopped when some convergence criterion is reached. The two most common criteria are based on the difference of total energies or densities from iteration i and $i-1$, i.e., the cycle is stopped when $|E_i - E_{i-1}| < \eta$ or $\Delta n \equiv \int d\mathbf{r} |n_i(\mathbf{r}) - n_{i-1}(\mathbf{r})| < \eta$, where E_i and n_i are the total energy and density at iteration i, and η is a prescribed tolerance parameter. (The following section will discuss the importance of convergence.) If the self-consistency criteria are not satisfied then one continues the iteration. Ideally, the starting density in the new cycle would be the density obtained in the previous step. In solving the nonlinear KS equations, however, this leads to instabilities. Various density mixing schemes have been introduced to avoid this problem, with the simplest being linear mixing [50], which is what we use. In linear mixing, rather than directly using the new density, we slowly mix it in. To do this, the next iteration's density is a linear combination of the previous iteration's density and the new density:

$$n_{i+1} = \alpha n_{new} + (1 - \alpha) n_i \tag{2.16}$$

where n_{new} is obtained from Eq. (2.7) and α is a number in the range [0,1]. This value specifies how much the new density contributes in the mixing. For stable iterations, this value is typically less than 0.2 (determined empirically).

2.2.2.1 Convergence of the ground state

For time development, discussed below, it is very important to have a well-converged ground state. Otherwise, the time propagation of a poorly-converged density quickly amplifies the existing errors. In the context of the iterative Kohn-Sham procedure discussed above, convergence means that the iteration is terminated only after the density has converged to a stable state. As mentioned above, this can be conveniently assessed by monitoring the total system energy vs. time, or the change in density vs. time, as shown in Figure II.2 for a ground state calculation using benzene. Note that the vertical axes are logarithmic. In this figure, notice that both plots show a decrease, followed by an abrupt transition to a nearly flat region which has a small value. Empirically, we have found that this transition typically marks convergence. The oscillations visible are due to the Kohn-Sham procedure "hunting" for better values. Using the onset of the nearly-flat region as a marker of convergence, notice that the two plots in Figure II.2 seem to show different convergence times. This is reasonable; it is our experience that the energy and density can converge at different

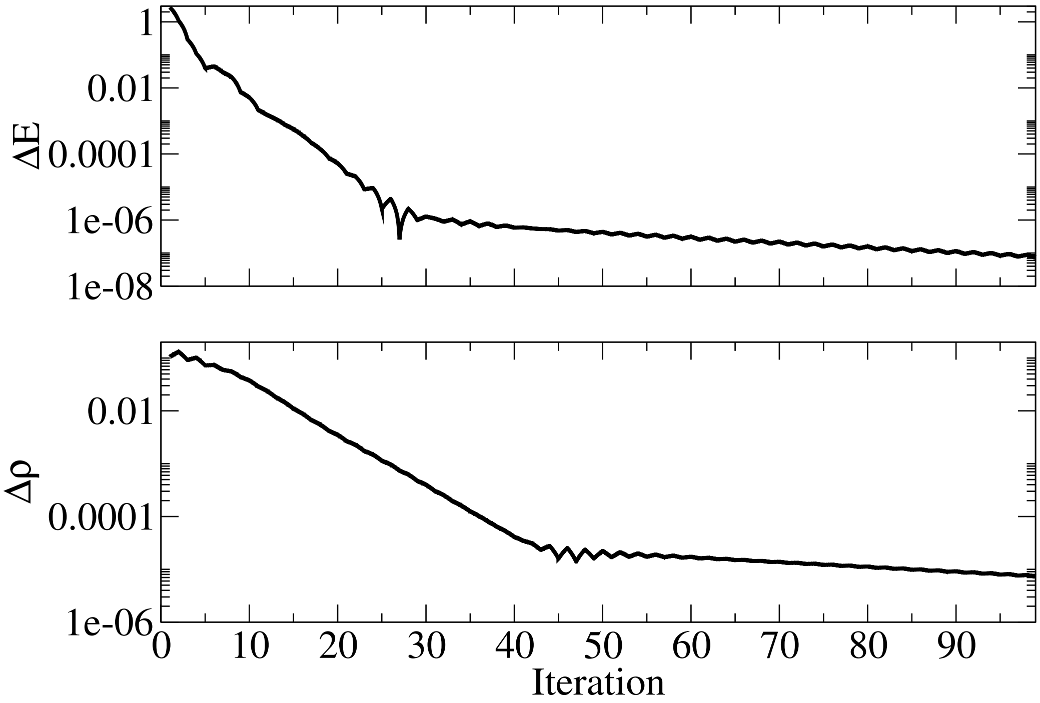

Figure II.2: Change in total energy and density vs. iteration, showing convergence.

times, and often the energy converges first. Our usual procedure (again empirically determined) is to allow both energy and density to converge before calling the system as a whole converged.

2.3 Time-dependent density functional theory (TDDFT)

Like the HK theorems for time-independent DFT, the Runge-Gross theorem [51] puts TDDFT on solid theoretical ground by establishing the one-to-one correspondence between a time-dependent external potential and a time-dependent charge density. One way to proceed is to simply include the time-dependent potential in the Kohn-Sham equations and then solve them. The addition of time, however, makes these equations difficult to solve in general. If the external field is weak, another approach is to use perturbation theory, e.g. in the form of linear response theory

[52]. In this method the ground state of the system is perturbed to calculate the first-order response. We avoid the restrictions of linear assumptions and solve the time-dependent Kohn-Sham (TDKS) equations by time propagating the orbitals, as described below.

In the TDDFT framework [53] the electronic motion is described by the following time-dependent Kohn-Sham equation for single particle orbitals ϕ_i

$$i\hbar\frac{\partial}{\partial t}\phi_i(\mathbf{r},t) = H\phi_i(\mathbf{r},t) \tag{2.17}$$

with

$$H = H_{KS} + V_{ext} \tag{2.18}$$

$$H_{KS} = -\frac{\hbar^2}{2m}\nabla_{\mathbf{r}} + V_A(\mathbf{r},t) + V_H(\mathbf{r},t) + V_{XC}[\rho](\mathbf{r},t), \tag{2.19}$$

where $V_{ext}(\mathbf{r},t)$ is the time-dependent external potential, $V_A(\mathbf{r},t)$ is the atomic potential, $V_H(\mathbf{r},t)$ is the Hartree potential, and $V_{XC}(\mathbf{r},t)$ is the exchange-correlation potential. The pseudopotential approach [54] is used to represent the atomic potentials $V_A(\mathbf{r},t)$. The exchange-correlation potential $V_{XC}(\mathbf{r},t)$ is constructed using the adiabatic local density approximation [55] and the Hartree potential is calculated by solving the Poisson equation. The electron charge density is given by $\rho(\mathbf{r},t) = \sum_i |\Psi_i(\mathbf{r},t)|^2$ and the current is defined as

$$\mathbf{j}(\mathbf{r},t) = \frac{e\hbar}{2im}\sum_i \left(\phi_i^*\nabla\phi_i - \phi_i\nabla\phi_i^*\right) = \frac{e\hbar}{m}Im\left(\phi^*(\vec{r})\nabla\phi(\vec{r})\right). \tag{2.20}$$

2.4 Time propagation

The time-dependent Kohn-Sham equation can be solved by time propagating the Kohn-Sham orbitals. Once a well-converged ground state density of the system is obtained, it is used as the initial state in the time development of the orbitals. This yields the time evolution of the density and allows calculation of time-dependent observables such as the current.

We use $\phi(\mathbf{x}, 0)$ to represent an orbital's known initial state at $t = 0$. The orbital at any future time $t + \Delta t$ is

$$\phi(\mathbf{x}, t + \Delta t) = e^{-iH\Delta t/\hbar}\phi(\mathbf{x}, t). \tag{2.21}$$

However, this is only exact for a time-independent Hamiltonian [56]. A good approximation is to keep Δt smaller than the characteristic time of the time-dependent part of the Hamiltonian, so that the Hamiltonian varies little during Δt.

Once $\phi(\mathbf{x}, t + \Delta t)$ is found, it is used to calculate the next step's orbital $\phi(\mathbf{x}, t + 2\Delta t)$, and so on. This iterative procedure yields the orbitals for each time step. Once this is done for all of the KS orbitals ϕ_i, the density can be calculated as

$$\rho(\mathbf{x}, t) = \sum_{i=1}^{N} |\phi_i(\mathbf{x}, t)|^2. \tag{2.22}$$

To actually implement the procedure defined in Equation 2.21, an expression must be found for $e^{-iH\Delta t/\hbar}$. There are several approaches to this, and they typically vary in terms of computational effort, numerical stability, and unitarity. The latter property is important in order to preserve the orthonormality of the orbitals as they are time developed [56].

One such method is to simply Taylor expand the exponential [57], and then apply each expansion term to the orbital:

$$e^{-iH\Delta t/\hbar} \approx \sum_{i=0}^{N-1} \left[\frac{(-i\Delta t)^n H/\hbar}{n!} \right] \tag{2.23}$$

where N_t is the number of terms in the expansion. To achieve reasonable accuracy, several (~ 4) expansion terms are needed, which makes this method computationally demanding. In addition, the method is numerically unstable for large Δt and so only small time steps may be used, resulting in more computations for a given time range.

We can also use the Crank-Nicholson method [58] which, compared to the Taylor method, requires less computational effort per time step. In addition, larger time steps are allowed due to the method's numerical stability. In this approach, the exponential is approximated as

$$e^{-iH\Delta t/\hbar} \approx \frac{1 - \frac{i\Delta t}{2\hbar} H}{1 + \frac{i\Delta t}{2\hbar} H} \tag{2.24}$$

The Crank-Nicholson approach requires the calculation of a matrix inverse which, for large bases, can be prohibitively expensive. For this reason, when using a real-space grid basis, we use the Taylor propagator. The Crank-Nicholson operator is used for smaller bases such as atom-centered atomic orbitals.

2.5 Calculation of the current

The current density at position $\vec{r}$ due to an eigenfunction $\phi(\vec{r})$ is (cf. Equation 2.20)

$$\vec{j}(\vec{r}) = \frac{e\hbar}{m} Im\left(\phi^*(\vec{r})\nabla\phi(\vec{r})\right) \tag{2.25}$$

where e and m are the electron's charge and mass, respectively. Assume that we want to find the $\hat{x}$ component of the current density (the other components are calculated in the same way). In Cartesian coordinates the $\hat{x}$ component is

$$j_x(x, y, z) = \frac{e\hbar}{m} Im\left(\phi^*(x, y, z)\frac{\partial\phi(x, y, z)}{\partial x}\right) \tag{2.26}$$

Approximating the first derivative by a first-order finite difference,

$$j_x(x_i, y, z) \approx \frac{e\hbar}{m} Im\left(\phi^*(x_{i+1}, y, z)\frac{\phi(x_{i+1}, y, z) - \phi(x_i, y, z)}{\Delta_x}\right) \tag{2.27}$$

where using Δ_x is the spatial step size in the $\hat{x}$ direction. Here a first-order finite difference is used for brevity, while in practice a higher-order form (e.g., fourth order) would be more appropriate.

To get the total current passing through a surface S normal to the $\hat{x}$ direction,

$$I = \int_S \vec{J} \cdot d\vec{A} = \int\int j_x dy dx \tag{2.28}$$

where $\vec{dA}$ is the differential area and is normal to the surface S. In discrete form this integral becomes a sum

$$I = \Delta_y \Delta_z \sum_m \sum_n j_x(x_i, y_m, z_n) \tag{2.29}$$

In this expression i is the $\hat{x}$ direction grid coordinate of the surface S, and m and n range over all grid coordinates in the $\hat{y}$ and $\hat{z}$ directions, respectively. Now inserting Equation 2.27,

$$I = \left(\frac{\hbar \Delta_y \Delta_z}{m}\right) \left(\frac{e}{\Delta_x}\right) Im \left(\sum_m \sum_n \phi^*(x_{i+1}, y_m, z_n) \left[\phi(x_{i+1}, y_m, z_n) - \phi(x_i, y_m, z_n)\right] \right)$$

(In calculations we use $\hbar = 0.658211899 \ eV \cdot fs$, $m = 510998.910 \ eV \cdot c^{-2}$, and $c = 2997.92458 \ \text{Å} / fs$, which gives $\hbar/m = 11.5767635$.)

2.6 Limitations

The limitations of our framework can be divided into two areas: limitations of the computational methods and limitations of DFT. The computational limitations for our methods are time and memory. As the number of atoms in a system increases, the calculation time increases. In addition, the computer memory required to store the large data structures also becomes large. However, as described further in Ref. [59], our approach provides an accurate method for electronic structure calculations that scales with system size in a manner better than other approaches. We can currently use systems consisting of several hundred atoms in a relatively short time.

As for DFT, the theory is exact [60], and inaccuracies appear only because of approximations in the exchange-correlation functional [61]. For this reason, for systems of just a few (e.g., 5-10) atoms, post Hartree-Fock methods are preferable [62], as they can be more accurate. However, for larger systems (such as those considered in this dissertation), DFT is better able to handle large systems. For the exchange-correlation functional, we use the local density approximation (LDA) from Perdew and Zunger [63]. Some of the known weaknesses include an overestimation of hydrogen bond strength [64, 65], an underestimation of band gaps [66], and errors in the Raman spectra [67]. For other properties, such as those relevant to the calculations here, LDA performs very well. Such properties include geometry calculations [68] and dipole moments [69].

CHAPTER III

BASIS FUNCTIONS

To calculate the field emission of a system, we have to numerically solve the electronic structure problem described in Chapter II. While a mathematical function may be defined at an infinite number of points, a computer can only store a finite number of these values. To perform numerical computations we must therefore find a way to approximate a function, to some desired accuracy, by a finite set of values. These values are defined on some basis of functions. Many types of basis exist, and each has advantages and disadvantages for different applications. The goal of this chapter is to present several of the major types of basis, and evaluate them in such a way that a good basis can be chosen for field emission calculations.

There are several issues to consider when considering a basis. From a practical point of view, the size of a basis is a critical parameter. Here we define the size N to be the number of states in a given basis. Part of our calculations involve matrix diagonalizations, which scale as $O(N^3)$ [70], so even small increases in N can quickly slow down calculations. On the other hand, too few states in a basis can make it incomplete and therefore inaccurate.

Another issue is locality. A local basis is one such as atomic orbitals, where subsets of the basis functions are centered on different atoms. This means that certain regions of space are well-covered, while other regions (i.e., between the atoms) are not. In such cases quantities such as wavefunctions can be represented more accurately in some regions than in others. In contrast, a nonlocal basis is one that is not tied to atomic centers or other objects. The basis functions are uniformly distributed. The most common example of this type of basis is the simple real space grid of lattice points.

3.1 Plane waves

Plane wave basis sets are most useful in systems where the potential is periodic, such as in a crystal. Here the potential can be written as

$$V(\mathbf{r}+\mathbf{R}) = V(\mathbf{r}), \tag{3.1}$$

where $\mathbf{R} = n_1\mathbf{a}_2 + n_2\mathbf{a}_2 + n_3\mathbf{a}_3$, n_1, n_2 and n_3 are integers and $\mathbf{a}_j$ is the jth lattice vector of the crystal. Using the Bloch theorem, the wave function of the electrons $\Psi_{i\mathbf{k}}(\mathbf{r})$ in the crystal can be written as a product of a periodic part

$$u_{i,\mathbf{k}}(\mathbf{r}+\mathbf{R}) = u_{i,\mathbf{k}}(\mathbf{r}),$$

and a wave-like part $\mathrm{e}^{i\mathbf{kr}}$

$$\Psi_{i\mathbf{k}}(\mathbf{r}) = \mathrm{e}^{i\mathbf{kr}} u_{i,\mathbf{k}}(\mathbf{r}) \tag{3.2}$$

for each crystal momentum $\mathbf{k}$. Due to its periodicity, $u_{i,\mathbf{k}}(\mathbf{r})$ can be expanded in terms of plane waves

$$u_{i,\mathbf{k}}(\mathbf{r}) = \sum_{\mathbf{G}} c_{i,\mathbf{G}+\mathbf{k}} \mathrm{e}^{i\mathbf{G}\cdot\mathbf{r}}. \tag{3.3}$$

These functions are orthogonal

$$\int_\Omega d\mathbf{r}\, u_{i,\mathbf{k}}(\mathbf{r})^* u_{j,\mathbf{k}}(\mathbf{r}) = \Omega\, \delta_{i,j}. \tag{3.4}$$

where Ω is the volume of the periodically repeated cell. The $\mathbf{G}$ vectors in the plane wave expansion can be expressed in terms of reciprocal lattice vectors. The reciprocal lattice vectors $\mathbf{b}$ are defined by

$$\mathbf{b}_i \mathbf{a}_j = 2\pi\delta_{ij}. \tag{3.5}$$

Equivalently, the reciprocal vectors can be expressed by a 3×3 matrix

$$(\mathbf{b}_1, \mathbf{b}_2, \mathbf{b}_3) = 2\pi(A^T)^{-1}, \qquad A = (\mathbf{a}_1, \mathbf{a}_2, \mathbf{a}_3). \tag{3.6}$$

With that definition the plane wave basis vectors are

$$\mathbf{G} = 2\pi(A^T)^{-1}\mathbf{g}, \qquad \mathbf{g} = (i, j, k) \tag{3.7}$$

where i, j and k are integers.

A plane wave basis is a natural choice for periodic systems. In the systems studied in this work, however, the systems are molecular-sized and surrounded by vacuum, and so are not periodic. One approach is to enclose the nanotube and vacuum in a "supercell", and then periodically repeat this throughout space. This makes a periodic system, but there are disadvantages. Within the supercell the lack of periodicity requires the use of a large number of plane wave basis states. Also, during time development, one must be careful to avoid interactions with the periodically repeated nanotubes, since they are not a physical reality. Since all of the field emitting structures in this dissertation are small, finite structures, plane waves were not considered further as a potential basis.

3.2 Atomic orbitals

In the linear combination of atomic orbitals (LCAO) approach, the wave function of the system is expanded as

$$\Phi(\mathbf{r}) = \sum_{i=1}^{N_{atom}} \sum_{k_i=1}^{n_i} \sum_{l_i=0}^{l_i^{max}} \sum_{m_i=-l_i}^{l_i} c_{ik_il_im_i} \phi_{k_il_im_i}(\mathbf{r} - \mathbf{R}_i) \tag{3.8}$$

where $\mathbf{R}_i$ is the position of the ith atom, N_{atom} is the number of atoms in the system, n_i is the number of orbitals for a given orbital momentum, $c_{ik_il_im_i}$ are the linear combination coefficients, and l_i^{max} is the maximum orbital momentum used for a given atom. The basis functions are defined as

$$\phi_{klm}(\mathbf{r}) = \varphi_{kl}(r) Y_{lm}(\hat{\mathbf{r}}) \tag{3.9}$$

where $\varphi_{kl}(r)$ is the radial part of the wave function.

The variational solution of the Kohn-Sham equation using the atomic orbital basis leads to the generalized eigenvalue problem

$$HC = ESC \tag{3.10}$$

where

$$H_{ij} = \langle \phi_i(\mathbf{r} - \mathbf{R}_i) | H | \phi_j(\mathbf{r} - \mathbf{R}_j) \rangle, \qquad \phi_i \equiv \phi_{k_i l_i m_i} \tag{3.11}$$

is the Hamiltonian,

$$O_{ij} = \langle \phi_i(\mathbf{r} - \mathbf{R}_i) | \phi_j(\mathbf{r} - \mathbf{R}_j) \rangle \tag{3.12}$$

is the overlap matrix,

$$C^T = (c_1, \ldots, c_N) \qquad c_i \equiv c_{ik_i l_i m_i} \tag{3.13}$$

are the linear variational coefficients, and N is the dimension of the basis.

There are many different ways to construct efficient atomic basis functions. The construction depends on whether one wants to do an all-electron or a pseudopotential calculation. The all-electron calculation is significantly more demanding as tightly bound, oscillating core states have to be approximated.

One can represent the radial part of the atomic basis function numerically or by a basis function expansion. In the numerical case, as the name implies, the radial shape $\varphi_{kl}(r)$ is numerically tabulated and therefore fully flexible (i.e., not dependent on a particular expansion basis). This allows the creation of optimized element-dependent basis sets that are as compact as possible while retaining a high and transferable accuracy in production calculations up to meV-level total energy convergence. On the other hand, one can also expand the radial wave function using an appropriate basis set,

$$\varphi_{kl}(r) = \sum_i a_i^{kl} \psi_i(r), \tag{3.14}$$

where ψ_i is often chosen to be Gaussian or exponential function. To determine $\varphi_{kl}(r)$

one usually solves the radial Schrödinger equation

$$\left(-\frac{1}{2}\frac{d^2}{dr^2}+\frac{l(l+1)}{r^2}+v(r)+v_{conf}(r)\right)\varphi_{kl}(r)=\epsilon_{kl}\varphi_{kl}(r) \tag{3.15}$$

where $v(r)$ is the atomic potential and v_{conf} is a confining potential. The role of the confining potential is to cut off the long range and slowly decaying tails of the basis functions. Many different confining potentials have been developed [71, 72, 73, 74]; the best choice is a smooth cutoff potential to ensure the smooth decay of the wave function and its first derivative at the cutoff radii r_{cutoff}. The cutoff radius, together with the number of basis functions per atom will be the two main parameters controlling the convergence.

If one uses numerical orbitals, the solution of the radial Schrödinger equation immediately provides the basis functions, $\varphi_{kl}(r)$. In case of a basis function expansion (see Equation 3.14) the linear combination coefficients can be determined by either fitting the numerical solution or by solving the radial Schrödinger equation variationally.

Atomic orbitals [75, 76, 77, 78, 79, 80] are a popular choice of basis in electronic structure calculations. Compared to other bases such as plane waves and real-space grids (see below), methods based on LCAO are more efficient in terms of basis size, because atomic orbitals are much better suited to represent molecular or Bloch wavefunctions. Another advantage of localized atomic orbitals is that the Hamiltonian matrix becomes sparse as the system size increases. This has recently renewed interest in LCAO bases because the sparsity makes them suitable for order-N methods

[81, 82, 83, 84] in which computational effort scales linearly with system size. Local atomic orbital bases also offer a natural way of quantifying magnitudes like atomic charge, orbital population, bond charge, charge transfer, etc.

Disadvantages of LCAO include the fact that the functions can become overcomplete (linear dependence can occur in a calculation if two similar functions are centered at the same atom), that they are difficult to program (especially if high angular momentum functions are needed), and that it is difficult to test or to demonstrate absolute convergence since there are many parameters.

Another problem is that since the atomic orbitals are centered at atoms, they are localized. This presents a challenge when trying to represent wavefunctions between atoms or in a field emission region outside of the molecule, as there are simply not enough basis states in those regions. One can continue to add more and more orbitals to the basis set in order to improve accuracy. However, the localized nature of the orbitals means that adding more states increases overlap between states, leading to loss of orthogonality and possible numerical issues (e.g. overcompleteness, mentioned above).

3.3 Real space grids

A grid consists of a finite set of locations in space and/or time, and is the discrete analog to a continuous coordinate system. The various quantities that we will be working with will only be defined at these points. In this way, the grid provides a method to obtain a discrete sampling of continuous quantities. Grids can be used for problems with any number of dimensions, but here we introduce the concepts using the simple case of one dimension; the extension to more dimensions is straightforward, and will be demonstrated later in this section.

To set up a one-dimensional grid, we need to know the start coordinate a, the ending coordinate b, and the "step size" (i.e., distance between points) h. Given these values, the total number of grid points N is

$$N = 1 + \frac{b-a}{h} \tag{3.16}$$

Notice that $\frac{b-a}{h}$ gives the number of intervals of size h that will fit into the space between a and b. The grid points are defined at the borders of these intervals, and so the number of grid points is one more than the number of these intervals. For example, in the simple case of a single interval, there are two grid points (the two ends of the interval).

The location of the i^{th} grid point is

$$x_i = a + (i-1) \times h \tag{3.17}$$

where i runs from 1 to N. For some applications it is more convenient to specify the total number of grid points N rather than the step size. In this case, one obtains h as

$$h = \frac{b-a}{N-1}. \tag{3.18}$$

Now that we have defined a grid, we can use it to represent various quantities. Potentials are simply sampled at the grid locations, but it is less clear how to handle the derivative in the kinetic energy term of the Schrödinger equation. In the next section we show how to represent derivatives on a grid using finite differences. After this, the Lagrange function approach is described. This is more complicated than finite differences, but is also more accurate.

3.3.1 Finite differences

The finite difference method replaces the derivatives in differential equations by approximations. These approximations are made up of weighted sums of function values. This results in a large system of equations to be solved, in place of the differential equation.

Suppose we want to calculate the first derivative of some function $\varphi(x)$. The obvious choice, using the definition of the first derivative, is

$$\varphi'(x) = \frac{\varphi(x+h) - \varphi(x)}{h} \tag{3.19}$$

for some suitably small h. For a given expression, smaller values of h lead to more accurate approximations. This is a "one-sided" and "forward" approximation because $\varphi'(x)$ is calculated only at values that are larger than or equal to x. Another one-sided possibility is the "backward" difference

$$\varphi'(x) = \frac{\varphi(x) - \varphi(x-h)}{h}. \tag{3.20}$$

Each of these finite difference formulas gives an approximation to $\varphi'(x)$ that is accurate to first order, meaning that the size of the error is roughly proportional to h itself.

Another possibility is to use a centered approximation

$$\varphi'(x) = \frac{\varphi(x+h) - \varphi(x-h)}{2h}. \tag{3.21}$$

This expression is the average of the two one-sided approximations, and it gives a better approximation to $\varphi'(x)$. The error is proportional to h^2, which (for $h < 1$) is smaller than for the one-sided case.

The one-sided expressions involve two points (counting x itself), while the centered version uses three. For this reason they are called "two-point" and "three-point" expressions, respectively. By using expressions with even more points, one can continue to improve accuracy. Notice that these expressions have the same basic structure: a linear combination of function values from different positions. The Taylor expansion of $\varphi(x)$ gives the coefficients for these linear combinations, as we now show.

As an example, let's say we want to find expressions involving five points. From a fourth-order Taylor expansion we get

$$\varphi(x \pm h) = \varphi(x) \pm \varphi'(x)h + \frac{1}{2}\varphi''(x)h^2 \pm \frac{1}{6}\varphi'''(x)h^3 + \frac{1}{24}\varphi''''(x)h^4$$

and

$$\varphi(x \pm 2h) = \varphi(x) \pm \varphi'(x)2h + \frac{1}{2}\varphi''(x)(2h)^2 \pm \frac{1}{6}\varphi'''(x)(2h)^3 + \frac{1}{24}\varphi''''(x)(2h)^4$$

This gives four equations for φ and its derivatives. Using these, along with the identity $\varphi(x) = \varphi(x)$, we have five equations. In matrix form this system of equations is

$$A\mathbf{x} = \mathbf{b}, \tag{3.22}$$

where

$$A = \begin{pmatrix} 1 & -2 & 2 & -\frac{4}{3} & \frac{2}{3} \\ 1 & -1 & \frac{1}{2} & -\frac{1}{6} & \frac{1}{24} \\ 1 & 0 & 0 & 0 & 0 \\ 1 & 1 & \frac{1}{2} & \frac{1}{6} & \frac{1}{24} \\ 1 & -2 & 2 & -\frac{4}{3} & \frac{2}{3} \end{pmatrix} \tag{3.23}$$

$$\mathbf{x} = \begin{pmatrix} \varphi(x) \\ \varphi(x)' \\ \varphi(x)'' \\ \varphi(x)''' \\ \varphi(x)'''' \end{pmatrix}, \qquad \mathbf{b} = \begin{pmatrix} \varphi(x-2h) \\ \varphi(x-h) \\ \varphi(x) \\ \varphi(x+h) \\ \varphi(x+2h) \end{pmatrix}. \tag{3.24}$$

This is a system of linear equations that can be solved to find an expression for the derivatives. For the second derivative, for example, we have

$$\varphi''(x) = -\frac{1}{12}(\varphi(x+2h) + \varphi(x-2h)) + \frac{4}{3}(\varphi(x+h) + \varphi(x-h)) - \frac{5}{2}\varphi(x)$$

One can easily generalize the above example to higher orders. The starting point is the general Taylor expansion

$$\varphi(x+nh)=\sum_{i=0}^{\infty}\frac{1}{i!}\varphi^{(i)}(x)(nh)^i \qquad n=-m,...,m, \tag{3.25}$$

where $\varphi^{(i)}$ is the i^{th} derivative of φ and we truncate the series at m^{th} order. Using the notation

$$x_j=\varphi^{(j-1)}(x), \qquad b_k=\varphi(x+(k-m-1)h) \quad (j,k=1,...,2m+1)$$

and

$$A_{kj}=\frac{(k-m-1)^{j-1}}{(j-1)!}, \tag{3.26}$$

we can now construct the terms in Equation 3.22. By inverting A one obtains the desired derivatives:

$$\varphi^{(j-1)}(x)=\sum_{k=1}^{2m+1}C_k^j\varphi(x+(k-m-1)h), \tag{3.27}$$

where

$$C_k^j=\frac{1}{h^{j-1}}A_{jk}^{-1}. \tag{3.28}$$

Tables III.1 and III.2 list some of these coefficients.

Now we are ready to put these expressions together and use them to solve the one-dimensional Schrödinger equation. Using three-point finite differences, the second

Table III.1: Higher-order finite difference coefficients for the first derivative. $C^k_{i-n} = -C^k_{i+n}$

	C^k_i	C^k_{i+1}	C^k_{i+2}	C^k_{i+3}	C^k_{i+4}	C^k_{i+5}	C^k_{i+6}
k=1	0	$\frac{1}{2}$					
k=2	0	$\frac{2}{3}$	$-\frac{1}{12}$				
k=3	0	$\frac{3}{4}$	$-\frac{3}{20}$	$\frac{1}{60}$			
k=4	0	$\frac{4}{5}$	$-\frac{1}{5}$	$\frac{4}{105}$	$-\frac{1}{280}$		
k=5	0	$\frac{5}{6}$	$-\frac{5}{21}$	$\frac{5}{84}$	$-\frac{5}{504}$	$\frac{1}{1260}$	
k=6	0	$\frac{6}{7}$	$-\frac{15}{56}$	$\frac{5}{63}$	$-\frac{1}{56}$	$\frac{1}{385}$	$-\frac{1}{5544}$

Table III.2: Higher-order finite difference coefficients for the second derivative.

	C^k_i	$C^k_{i\pm1}$	$C^k_{i\pm2}$	$C^k_{i\pm3}$	$C^k_{i\pm4}$	$C^k_{i\pm5}$	$C^k_{i\pm6}$
k=1	-2	1					
k=2	$-\frac{5}{2}$	$\frac{4}{3}$	$-\frac{1}{12}$				
k=3	$-\frac{49}{18}$	$\frac{3}{2}$	$-\frac{3}{20}$	$\frac{1}{90}$			
k=4	$-\frac{205}{72}$	$\frac{8}{5}$	$-\frac{1}{5}$	$\frac{8}{315}$	$-\frac{1}{560}$		
k=5	$-\frac{5269}{1800}$	$\frac{5}{3}$	$-\frac{5}{21}$	$\frac{5}{126}$	$-\frac{5}{1008}$	$\frac{1}{3150}$	
k=6	$-\frac{5369}{1800}$	$\frac{12}{7}$	$-\frac{15}{56}$	$\frac{10}{189}$	$-\frac{1}{112}$	$\frac{2}{1925}$	$-\frac{1}{16632}$

derivative of a function can be written as

$$\phi''(x) = \frac{\phi(x+h) + \phi(x-h) - 2\phi(x)}{h^2}. \tag{3.29}$$

Defining

$$\phi(i) = \phi(x_i) = \phi(a + i \times h), \qquad V(i) = V(x_i) \tag{3.30}$$

the Schrödinger equation can be written as

$$-\frac{\hbar^2}{2m}\frac{\phi(i+1)+\phi(i-1)-2\phi(i)}{h^2}+V(i)\phi(i)=E\phi(i) \tag{3.31}$$

for $i = 0, \ldots, N-1$. Notice that two exterior points x_{-1} and x_N appear in this equation. For bound states, the boundary conditions for these points are assumed to be

$$\phi(-1)=\phi(N)=0. \tag{3.32}$$

Equation 3.31 can be rewritten as a matrix eigenvalue problem

$$HC = EC, \tag{3.33}$$

where

$$H_{ij}=\begin{cases}\frac{\hbar^2}{2m}\frac{2}{h^2}+V(i) & \text{if } \; i=j \\ -\frac{\hbar^2}{2m}\frac{1}{h^2} & \text{if } \; i=j\pm 1 \\ 0 & \text{otherwise}\end{cases}, \tag{3.34}$$

and

$$C = \begin{pmatrix} \phi(0) \\ \phi(1) \\ \vdots \\ \phi(N-2) \\ \phi(N-1) \end{pmatrix}. \tag{3.35}$$

3.3.2 Lagrange functions

The simple grid used in finite difference calculations has all points equally spaced, and all points are equally important (i.e., equally weighted). In general, one can choose the location and weighting of the points in a way that enhances numerical accuracy and/or efficiency. The Lagrange functions (LFs) [70] are an example of this, and are described in this section.

The Lagrange functions $L_i(x)$, associated with a grid $\{x_i\}$ $(i = 1, \ldots, M)$, are defined as a product of a Lagrange interpolant [85] $\pi_i(x)$ and a weight function $w(x)$,

$$L_i(x) = \lambda_i \pi_i(x) \sqrt{w(x)}, \tag{3.36}$$

where the Lagrange interpolating polynomial is defined as

$$\pi_i(x) = \prod_{\substack{k=1 \\ k \neq i}}^{M} \frac{x - x_k}{x_i - x_k} \tag{3.37}$$

and the normalization factor λ_i will be specified below. The Lagrange interpolants are often used in numerical calculations because functions can be simply and accurately interpolated by their values at the grid points

$$f(x) = \sum_{i=1}^{M} f(x_i)\pi(x). \tag{3.38}$$

At this point we have complete freedom in choosing the grid points x_i $(i = 1, \ldots, M)$ and the weight function $w(x)$. The most advantageous choice is to use the Gaussian quadrature points (abscissas) associated with the weight function $w(x)$. This choice not only guarantees that numerical integrations over the LFs will be of Gaussian quadrature accuracy, but it also ensures that the LFs form an orthogonal basis. Gauss originally used continued fractions to find the most suitable abscissas x_i and weights w_i to calculate the integral

$$\int_a^b f(x)w(x)dx \approx \sum_{i=1}^{M} w_i f(x_i). \tag{3.39}$$

Christoffel later showed that the Gaussian quadrature points are the roots of the orthogonal polynomials associated with the weight function $w(x)$. These orthogonal polynomials are generated by a three-term recurrence relation [85]

$$b_{i+1}p_{i+1}(x) = (x - a_{i+1})p_i(x) - b_i p_{i-1}(x), \qquad (p_{-1}(x) = 0,\ p_0(x) = 1)$$

where

$$a_{i+1} = (p_i|x|p_i), \qquad b_i = (p_i|x|p_{i-1}) \tag{3.40}$$

and the scalar product of two functions is defined as

$$(f|g) = \int_a^b f(x)g(x)w(x)dx \quad \text{and} \quad \int_a^b w(x)dx = 1. \tag{3.41}$$

The recurrence relation can be rewritten in a more elegant matrix form

$$\begin{pmatrix} a_1 & b_1 & 0 & & & \\ b_1 & a_2 & b_2 & & & \\ & . & . & & & \\ & & & b_{M-2} & a_{M-1} & b_{M-1} \\ & & & 0 & b_{M-1} & a_M \end{pmatrix} \begin{pmatrix} p_0(x) \\ p_1(x) \\ . \\ p_{M-2}(x) \\ p_{M-1}(x) \end{pmatrix} = x \begin{pmatrix} p_0(x) \\ p_1(x) \\ . \\ p_{M-2}(x) \\ p_{M-1}(x) \end{pmatrix} - \begin{pmatrix} 0 \\ 0 \\ . \\ 0 \\ p_M(x) \end{pmatrix}. \tag{3.42}$$

This rearrangement shows that the most convenient way to find the roots x_i of $p_M(x)$ is to diagonalize the above matrix, which we will call J [86]. The eigenvalues x_i are the desired Gaussian quadrature points while the corresponding weights w_i are given by the squares of the first elements of the eigenvectors of J, defining the normalization of the LFs as

$$\lambda_i = \frac{1}{\sqrt{w_i}}. \tag{3.43}$$

By defining both x_i and λ_i the Lagrange functions are fully determined (see Eq. 3.36). Using the polynomials p_k one can give an equivalent definition. First define

$$\varphi_k(x) = \frac{1}{\sqrt{h_k}} p_k(x) \sqrt{w(x)} \tag{3.44}$$

where h_k is the norm of p_k. Using the Christoffel-Darboux formula [85] one can derive the relation

$$\sum_{k=0}^{M-1} \varphi_k(x)\varphi_k(y) = \frac{k_{M-1}}{k_M}\sqrt{\frac{h_M}{h_{M-1}}} \frac{\varphi_M(x)\varphi_{M-1}(y) - \varphi_{M-1}(x)\varphi_M(y)}{x-y}, \tag{3.45}$$

where k_n is the coefficient of x^n in $p_n(x)$. As the grid is defined by the zeros of $p_M(x_i) = 0$, using the above equation the Lagrange functions can be defined as

$$L_i(x) = \frac{1}{\varphi'_M(x_i)} \frac{\varphi_M(x)}{x - x_i} = \lambda_i \sum_{k=0}^{M-1} \varphi_k(x)\varphi_k(x_i) \tag{3.46}$$

with

$$\lambda_i = \frac{k_{M-1}}{k_M}\sqrt{\frac{h_M}{h_{M-1}}} \frac{1}{\varphi'_M(x_i)\varphi_{M-1}(x_i)}. \tag{3.47}$$

The most important properties of the Lagrange functions are

1. Orthogonality

$$\int_a^b L_i(x)L_j(x)dx = \delta_{ij}. \tag{3.48}$$

2. Cardinality

$$L_i(x_j) = \delta_{ij}. \tag{3.49}$$

3. A wave function using the LFs can be expanded as

$$\phi(x) = \sum_{i=1}^{M} \phi(x_i) L_i(x) \tag{3.50}$$

   that is, the variational parameters are the values of the wave function at the grid points.

4. The kinetic energy matrix (Laplacian) can be simply calculated by differentiating the LFs

$$L_i''(x) = \frac{d^2 L_i}{dx^2} = \sum_j D_{ij} L_j(x) \tag{3.51}$$

   D_{ij} can be calculated by higher-order Gaussian integration and in some cases analytically.

5. The matrix elements of the potential are simply the values of the potential at the grid points

$$\langle L_i | V | L_j \rangle = V(x_i)\delta_{ij}. \tag{3.52}$$

6. The Hilbert space of the LFs and the p_M polynomials is isomorphic: The Christoffel-Darboux relation connects the Lagrange functions to the orthogonal polynomials [87, 88, 89]

$$L_i(x) = \sum_{k=0}^{M-1} c_k p_k(x), \qquad c_k = \lambda_i p_k(x_i). \tag{3.53}$$

   This equation shows that the LFs have the same accuracy as the M-th order polynomials (with the same weight function) and this equation can also be used to define Lagrange functions in terms of orthogonal polynomials. From a practical point of view, however, the difference is enormous. In the case of the $p_i(x)\sqrt{w(x)}$ basis functions, both the kinetic energy and the potential energy matrix elements have to be calculated analytically or numerically and the Hamiltonian is dense. For the LFs the Hamiltonian is sparse and efficient iterative diagonalization techniques can be used.

7. Exponential convergence:

$$\text{Error} \approx O((1/M)^M). \tag{3.54}$$

   The error is decreasing faster than any finite power of M because the power in the error formula is always increasing, too. This is called "infinite order" or "exponential convergence" [90].

8. The position operator is diagonal: The J matrix is the matrix of the position operator x. In this way the Lagrange basis can also be considered to be a representation where the position operator is diagonal.

Using the Lagrange functions the Schrödinger equation can be written as

$$\sum_{i=0}^{M-1} \left(\frac{\hbar^2}{2m} D_{ji} + V(x_j)\delta_{ij} \right) \phi(x_i) = E\phi(x_j) \quad j = 0, \ldots, M-1. \tag{3.55}$$

We now introduce the fixed-node Lagrange functions [91], which are the form of LF used in this dissertation's calculations. These functions are defined on equidistant grid points and they are zero at the boundary. These functions are constructed by using

$$w(u) = \sqrt{1-u^2}, \qquad u(x) = \cos(x) \tag{3.56}$$

as weight function and mapping. This generates the orthogonal functions

$$p_k(x) = \sqrt{\frac{2}{\pi}} \sin(nx), \tag{3.57}$$

and using Eq. 3.53

$$L_i(x) = \frac{2}{N+1} \sum_{n=1}^{N} \sin(nx)\, \sin(nx_i), \qquad 0 \leq x \leq \pi, \tag{3.58}$$

with equally-spaced grid points

$$x_i = \frac{k\pi}{N+1}. \tag{3.59}$$

As is clear from the definition and can be seen in Fig. III.1, the basis functions are zero at the starting and ending points of the $[0, \pi]$ interval.

For an $[a, b]$ interval the grid becomes

$$x_i = a + \frac{(b-a)}{N+1} i, \qquad i = 1, \ldots, N, \tag{3.60}$$

and the Lagrange basis functions are

$$L_i(x) = \frac{2}{N+1} \sum_{k=1}^{N} \sin\left(\frac{k\pi(x-a)}{b-a}\right) \sin\left(\frac{k\pi(x_i-a)}{b-a}\right). \tag{3.61}$$

Note that for $(b-a) \to \infty$, $N \to \infty$

$$\Delta x = \frac{b-a}{N}, \tag{3.62}$$

$$L_i(x) = \frac{\sin\left(\pi(x-x_i)/\Delta x\right)}{\pi(x-x_i)}, \tag{3.63}$$

which is $1/\Delta x$ for $x = x_i$ and zero otherwise, and behaves like $\delta(x-x_i)$ for $\Delta x \to 0$.

For these LFs the kinetic energy is

$$T_{ij} = \left\langle L_i \left| -\frac{\hbar^2}{2m}\frac{d^2}{dx^2} \right| L_j \right\rangle = -\frac{\hbar^2}{2m}\sum_{k=1}^{N} L_k(x_i) L_k''(x_j), \tag{3.64}$$

where

$$L_k''(x_j) = k^2 \left(\frac{\pi}{b-a}\right)^2 \frac{2}{N+1} L_k(x_j). \tag{3.65}$$

This can be calculated analytically. The sum can be rewritten as:

$$\begin{aligned} &\sum_{k=1}^{N} k^2 \sin\left(\frac{ki\pi}{N+1}\right)\sin\left(\frac{kj\pi}{N+1}\right) \\ &\quad = \sum_{k=1} N\frac{k^2}{2}\left[\cos\left(\frac{k(i-j)\pi}{N+1}\right) - \cos\left(\frac{k(i+j)\pi}{N+1}\right)\right] \\ &\quad = \frac{1}{2}\left[-\frac{d^2}{dx^2} Re\left(\sum_{k=1}^{N} e^{ikx}\Bigg|_{x=\frac{(i-j)\pi}{N+1}}\right) - \frac{d^2}{dx^2} Re\left(\sum_{k=1}^{N} e^{ikx}\Bigg|_{x=\frac{(i+j)\pi}{N+1}}\right)\right]. \end{aligned} \tag{3.66}$$

The geometric series above can be calculated:

$$Re\left(\sum_{k=1}^{N} e^{ikx}\right) = -\frac{1}{2} + \frac{1}{2}\frac{\sin\left[\left(N+\frac{1}{2}\right)x\right]}{\sin\left(\frac{x}{2}\right)}. \tag{3.67}$$

One then obtains

$$T_{ij} = \begin{cases} \frac{\hbar^2}{2m}(-1)^{i-j}\frac{\pi^2}{2(b-a)^2}\left[\frac{1}{\sin^2\left(\frac{\pi(i-j)}{2(N+1)}\right)} - \frac{1}{\sin^2\left(\frac{\pi(i+j)}{2(N+1)}\right)}\right] & \text{for i}\neq\text{j} \\ \\ \frac{\hbar^2}{2m}\frac{\pi^2}{2(b-a)^2}\left[\frac{2(N+1)^2+1}{3} - \frac{1}{\sin^2\left(\frac{\pi i}{N+1}\right)}\right] & \text{for i=j.} \end{cases}$$

For an $(-\infty, \infty)$ interval, $a \to -\infty$, $b \to \infty$, and the grid spacing $\Delta x = (b-a)/N$ remains finite with $N \to \infty$. The grid is now specified as $x_i \to i\Delta x$ with $i = 0, \pm 1, \pm 2, \ldots$. The kinetic energy becomes

$$T_{ij} = \frac{\hbar^2}{2m}\frac{(-1)^{i-j}}{\Delta x^2}\begin{cases} \frac{2}{(i-j)^2} & \text{for i}\neq\text{j} \\ \\ \frac{\pi^2}{3} & \text{for i=j.} \end{cases} \tag{3.68}$$

In the case of a radial grid, one uses $n \in (0, \infty)$, $a = 0$, $b \to \infty$, and $N \to \infty$. The radial grid is $r_i = i\Delta r$, $i = 1, \ldots$, and

$$T_{ij} = \frac{\hbar^2}{2m\Delta r^2}(-1)^{i-j}\begin{cases} \frac{2}{(i-j)^2} - \frac{2}{(i+j)^2} & \text{for i}\neq\text{j} \\ \\ \frac{\pi^3}{3} - \frac{1}{2i^2} & \text{for i=j.} \end{cases} \tag{3.69}$$

3.3.3 Extension to three dimensions

In this subsection we generalize the one-dimensional real space grid approaches presented above to three-dimensional (3D) problems.

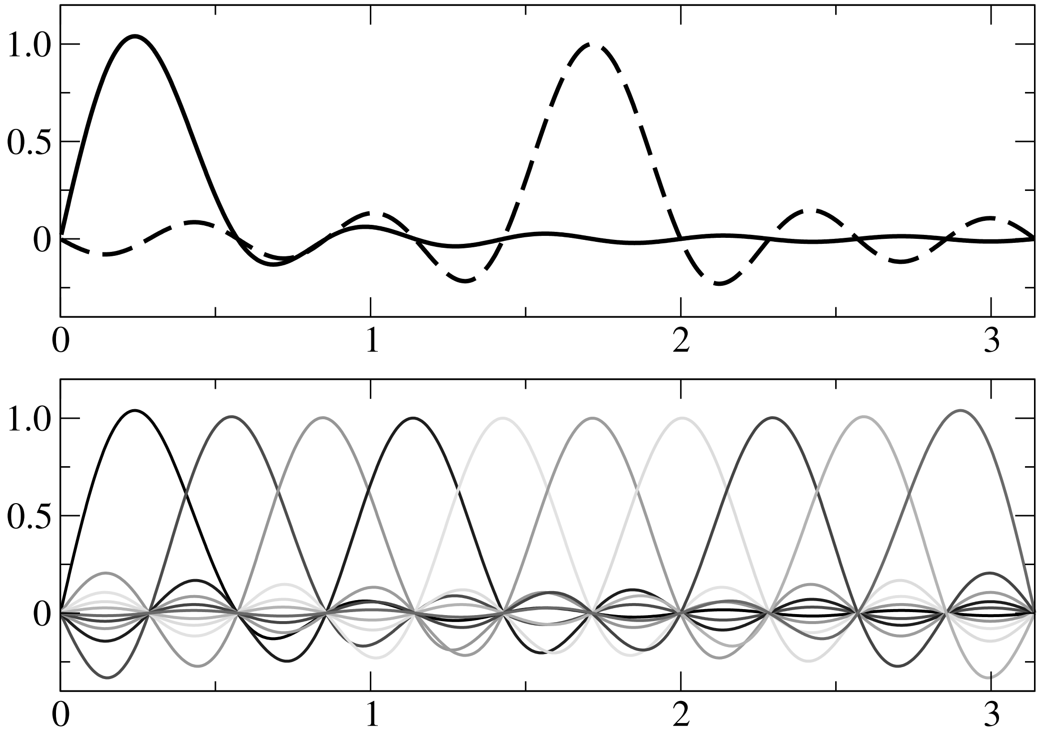

Figure III.1: Lagrange functions of Equation 3.58 for N=10. The upper panel show the basis functions for $i = 1$ (solid line) and $i = 5$ (dashed line). The lower panel shows the complete set of functions.

The computational cell is a rectangular box with sides L_1, L_2 and L_3 (see Fig. III.2). The following convention is used to label the grid points in 3D. Assuming that the 3D grid has N_1, N_2 and N_3 grid points in the x, y and z directions the index

$$k = N_1 \times N_2 \times (i_1 + 1 - 1) + N_2 \times (i_2 - 1) + i_3 \tag{3.70}$$

is used to define a given grid point, where i_1, i_2, and i_3 are the grid indices in the x, y, and z directions

$$i_1 = 1, \ldots, N_1, \qquad i_2 = 1, \ldots, N_2, \qquad i_3 = 1, \ldots, N_3, \tag{3.71}$$

and $k = 1, \ldots, N$, $N = N_1 \times N_2 \times N_3$. In an actual computation, the code must set up the grid index and assign the grid points in a real space mesh with discretization steps Δx,Δy and Δz. The code then defines a mapping

$$k \rightarrow (i_1, i_2, i_3)$$

and an inverse mapping

$$(i_1, i_2, i_3) \rightarrow k.$$

These mappings help to store the wave function and the potential in a vector rather than in a three dimensional matrix. The components of grid point $\mathbf{r}_k$ are

$$\begin{aligned}
x_k &= x_{i_1} = -\frac{L_1}{2} + (i_1 - 1)\Delta x, \qquad \Delta x = \frac{L_1}{N_1 - 1}, \\
y_k &= x_{i_2} = -\frac{L_2}{2} + (i_2 - 1)\Delta y, \qquad \Delta y = \frac{L_2}{N_2 - 1}, \\
z_k &= x_{i_3} = -\frac{L_3}{2} + (i_3 - 1)\Delta z, \qquad \Delta z = \frac{L_3}{N_3 - 1}.
\end{aligned} \tag{3.72}$$

To calculate the kinetic energy one has to evaluate the kinetic energy operator in 3D

$$-\frac{\hbar^2}{2m}\left(\frac{d^2}{dx^2} + \frac{d^2}{dy^2} + \frac{d^2}{dz^2}\right)\psi(x, y, z),$$

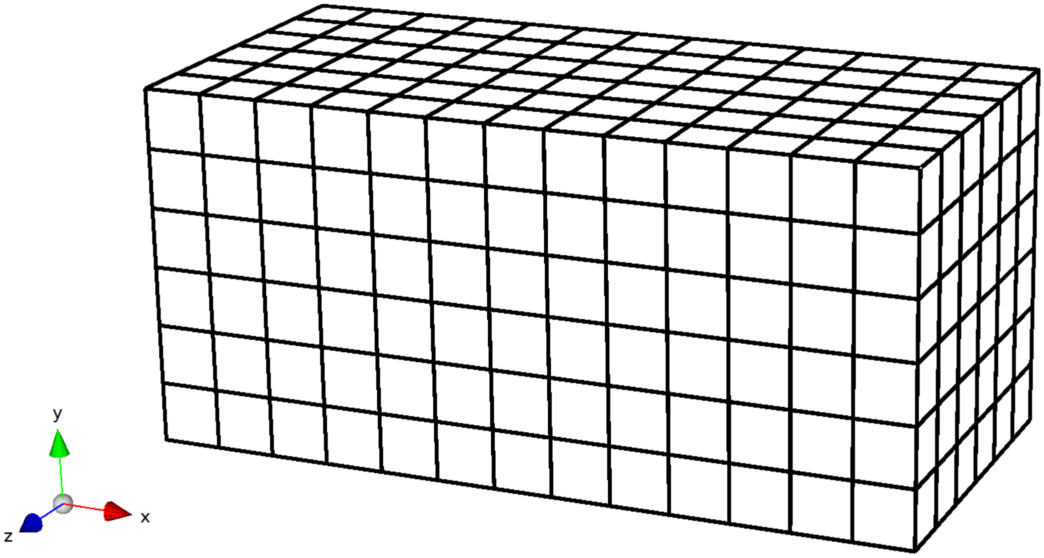

Figure III.2: Computational cell with a 3D grid.

which in the simplest three-point finite difference approximation takes the form

$$
\begin{aligned}
&-\frac{\hbar^2}{2m}\left(\frac{d^2}{dx^2}+\frac{d^2}{dy^2}+\frac{d^2}{dz^2}\right)\psi(x,y,z) = \\
-\frac{\hbar^2}{2m}\Bigg(\quad &\frac{\psi(i_1+1,i_2,i_3)+\psi(i_1-1,i_2,i_3)-2\psi(i_1,i_2,i_3)}{\Delta x^2}+ \\
&\frac{\psi(i_1,i_2+1,i_3)+\psi(i_1,i_2+1,i_3)-2\psi(i_1,i_2,i_3)}{\Delta y^2}+ \\
&\frac{\psi(i_1,i_2,i_3+1)+\psi(i_1,i_2,i_3-1)-2\psi(i_1,i_2,i_3)}{\Delta z^2}\Bigg).
\end{aligned}
\tag{3.73}
$$

Using the mapping introduced previously, the wave function can be represented as a vector $\psi(k) = \psi(i_1, i_2, i_3)$. Similarly, the potential on the grid is represented as a vector

$$V(x, y, z) = V(i_1, i_2, i_3) = V(k). \tag{3.74}$$

3.4 Box basis functions

In this section we define box basis functions. We begin by conceptually dividing the simulation volume into boxes. An example is shown in Figure III.3. Then, for the i^{th} box, we then diagonalize the Hamiltonian of the system just within that box. We keep the top N_b eigenstates, where N_b is a parameter that can be increased to improve accuracy, at the cost of computational speed. We repeat this for the other boxes. The sets of top eigenstates from each box are then combined to form the overall basis set for the calculations.

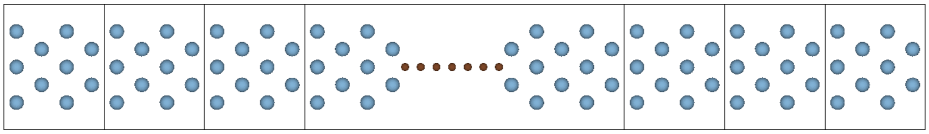

Figure III.3: Structure of the Al-C-Al system, showing division into boxes for the box basis.

Notice that we need to choose a basis for diagonalization within a box; we typically choose Lagrange functions, which were discussed in Section 3.3.2. The jth basis function in the ith box is expanded in terms of a tensorial product of Lagrange basis functions [92] as

$$\phi_j^{box,i}(\mathbf{r}) = \sum_{l=1}^{M_x^i} \sum_{m=1}^{M_y} \sum_{n=1}^{M_z} C^i_{j,lmn} L^i_l(x) L_m(y) L_n(z). \tag{3.75}$$

In the x direction, the Lagrange functions are defined on grid points $a_i - h < x_k^i < b_i + h$, where a_i is the left and b_i is the right boundary of box i, as

$$L_n^i(x) = \pi_n(x)\sqrt{w(x)} \qquad \pi_n(x) = \prod_{\substack{k=1 \\ k\neq n}}^{M_x} \frac{x - x_k^i}{x_n^i - x_k^i} \tag{3.76}$$

where $w(x)$ is the weight function and the index i indicates that the Lagrange function is defined in the ith box. The Lagrange functions in neighboring boxes can overlap and the region of overlap is determined by the parameter h. We use the same Lagrange basis $L_m(y)$ and $L_n(z)$ in the y and z directions in each box. By this construction there are $M_i = M_x^i \times M_y \times M_z$ Lagrange basis functions in box i. These functions are used to generate the box basis functions that are used in the transport calculations.

The box basis functions $\phi_j^{box,i}$ are selected by solving the eigenvalue problem

$$H_i C_j^i = E_j C_j^i \tag{3.77}$$

where H_i is the matrix of the Hamiltonian H_{KS} in the ith box in the orthogonal Lagrange function representation. After diagonalization this Hamiltonian has M_i eigenstates. By using a cutoff energy E_{cutoff} the lowest n_i eigenstates of this Hamiltonian are used as box basis states in the transport calculations. The convergence properties and accuracy of this approach has been studied in [93].

3.5 Basis set dependence in quantum transport calculations

Ideally we would proceed by identifying some benchmark field emission calculations and evaluating them in several bases. The results would be compared to the known benchmark results. We could then determine which basis performed best in terms of accuracy and efficiency. Unfortunately, no such benchmarks for field emission from nanostructures exist. Instead, we found a similar problem, quantum transport through nanostructures, which does have some benchmark results. The physics of the two situations are similar enough that the results from the transport tests can be extrapolated to the field emission case, and so allow us to choose an appropriate basis for field emission. Here we present a study of the basis set dependence of transport properties in nanostructures. The study varies both the type and size of basis sets and calculates transport properties for a nanoscale system.

The convergence and basis set dependence of quantum transport calculations is studied in the remainder of this chapter using localized atomic orbitals and nonlocalized basis sets. The non-equilibrium Green's function formalism and ground state density functional theory are used in the calculations.

The convergence of energy and other physical properties in ground state electronic structure calculations has been intensively studied in the past. Benchmark calculations have been established and state of the art electronic structure calculations are validated against them. Depending on the basis states used in the calculation there are various ways to control the convergence. In plane wave calculations [48] the convergence of the energy is controlled by the energy cutoff. In real-space grid calculations [94, 95, 96, 97, 98] convergence can be reached by increasing the number of grid points. Convergence of calculations using atomic orbitals are checked against the increase of the number of orbitals in the basis.

The convergence of the conductance or the transmission coefficient in quantum transport calculations [99, 100, 101, 102, 103, 104, 105, 106, 107, 108, 103, 109, 110, 111, 112] is more complicated. There is no simple minimum principle (like the minimum of the variational energy in ground state calculations) that can be used to judge the quality of the calculations. Most quantum transport calculations are based on the non-equilibrium Green's function (NEGF) formalism which, in its most common implementation, uses localized basis sets. The basis set dependence of these calculations is obviously a very important issue. Nevertheless, only a very few calculations have investigated the convergence of the transmission coefficient as a function of the basis size [113, 3]. In Ref. [113] Gaussian-based atomic orbitals were used and the convergence with respect to the number of Gaussian orbitals was investigated for a model gold-benzeneditholate-gold structure. In Ref. [3] several test systems were used and both atomic orbitals (SIESTA [81]) and Wannier function-based basis functions were tested. The slow convergence of the transport properties with localized atomic orbitals is apparent in both calculations. The main reason behind the slow convergence of atomic orbital-based calculations is that it is hard to represent the rapidly oscillating extended current-carrying states with localized orbitals centered on the atoms.

In this section the convergence of transport properties is investigated using different basis sets. Three different basis sets, (1) localized atomic orbitals (AOs), (2) AOs augmented with floating Gaussians, and (3) box basis functions are tested. The first set, the AO basis, is very popular in transport calculations and most transport codes use this representation. These basis functions are centered at atomic positions and give a very good description of the wave function near the atoms (where they are optimized), but the AO representation of the wave function between atoms is less flexible. The advantage of these basis sets is that they are localized and this localization property can be exploited to speed up large scale electronic structure calculations. On the other hand, these basis sets cannot be systematically enlarged in a simple way and the results are subject to basis set errors. To improve the description of the electron scattering wave function in the space between atoms one can augment the atomic orbitals in the interstitial region with suitably chosen basis functions. Here we add a grid of "floating" Gaussian functions to improve the representation of the wave function between atoms. The third set, the "box basis functions" consists of basis functions that are obtained by diagonalizing the Hamiltonian in an appropriately chosen region (box). Unlike the AOs these basis functions are not tied to atomic positions and are proven to be an efficient representation for electronic structure and transport calculations [93].

To calculate the transport properties the non-equilibrium Green's function (NEGF) formalism is used in the density functional theory (DFT) framework [99, 100, 101, 102, 104, 105, 106, 107, 108, 103, 109, 110, 111]. In the NEGF implementation one has to have basis states that do not connect the left and right leads and it is also advantageous to have basis functions that only connect the nearest periodically repeated layers in the lead. The basis function sets employed here satisfy both of these conditions.

The transport calculation has two steps. First the ground state density and potential are calculated self-consistently and then, using this self-consistent potential, the NEGF formalism is used to calculate the transmission as a function of energy. The accuracy of both of these steps depends on the basis set chosen. The basis set dependence of the ground state DFT calculation has been extensively researched in the past [114, 115]. The main objective of the calculations in this section is to investigate the basis set dependence of the second step, the transmission calculation,

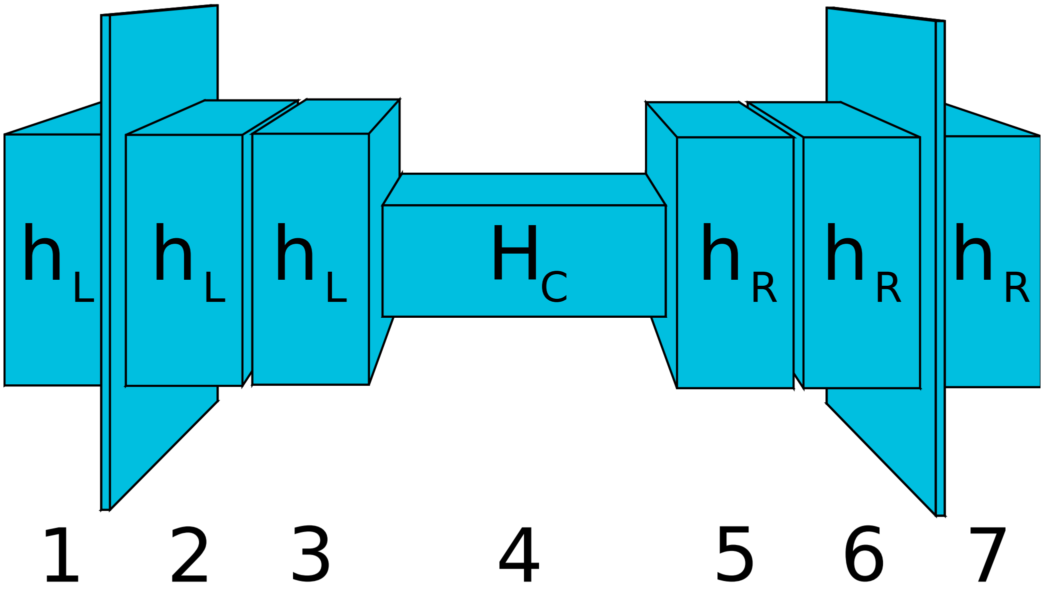

Figure III.4: Organization of the system into left/right leads (L/R) and a central device (C). The self-consistent potential is calculated for the central region between the planes. Only a few layers of the leads need to be included to obtain a converged potential for the central region.

which consists of the calculation of the Green's function of the system in a suitable basis representation. This will help to select the best basis for field emission as well.

3.5.1 Calculation of the transmission coefficient

In the NEGF framework the system is divided into left and right leads and a device part as shown in Figure III.4. The leads consist of periodically repeated layers (boxes). The Hamiltonian is defined as (cf. Equation 2.8)

$$H_{KS} = \frac{-\hbar^2}{2m}\nabla^2 + V_A(\mathbf{r}) + V_H[\rho](\mathbf{r}) + V_{xc}[\rho](\mathbf{r}), \tag{3.78}$$

where V_A is the Coulomb potential of the atomic nuclei, V_H is the Hartree potential, and V_{xc} is the exchange correlation potential.

Each region is represented by a set of basis functions Ψ^L, Ψ^C and Ψ^R. Here the index $X = L, C, R$ refers to the fact that these basis functions are situated in the $X = L, C, R$ (left, center, right) regions. As has been discussed, only neighboring regions overlap, that is

$$\langle \Psi_i^L | \Psi_j^C \rangle \neq 0 \qquad \langle \Psi_i^R | \Psi_j^C \rangle \neq 0, \tag{3.79}$$

but there is no overlap between the leads' basis functions

$$\langle \Psi_R | \Psi_L \rangle = 0. \tag{3.80}$$

In this basis representation the Hamiltonian and the overlap matrices of the left-lead–device–right-lead system, under the assumption that there is no interaction between the leads, takes the form

$$H = \begin{pmatrix} H_L & H_{LC} & 0 \\ H_{LC}^\dagger & H_C & H_{RC}^\dagger \\ 0 & H_{RC} & H_R \end{pmatrix} \qquad O = \begin{pmatrix} O_L & O_{LC} & 0 \\ O_{LC}^\dagger & O_C & O_{RC}^\dagger \\ 0 & O_{RC} & O_R \end{pmatrix}$$

where H_L (O_L), H_C (O_C), and H_R (O_R) are the Hamiltonian (overlap) matrices of the leads and the device. H_{LC} (O_{LC}) and H_{RC} (O_{RC}) are the coupling matrices between the central region and the leads defined as

$$H_{ij}^{XY} = \langle \Psi_i^X | H_{KS} | \Psi_j^Y \rangle \qquad O_{ij}^{XY} = \langle \Psi_i^X | \Psi_j^Y \rangle. \tag{3.81}$$

By defining the self energies of the leads ($X = L, R$) as

$$\Gamma_X(E) = i\left(\Sigma_X(E) - \Sigma_X^\dagger(E)\right) \tag{3.82}$$

where

$$\Sigma_X(E) = (EO_{XC} - H_{XC})g_X(E)(EO_{XC} - H_{XC}) \tag{3.83}$$

and where

$$g_X(E) = (EO_X - H_X)^{-1} \tag{3.84}$$

is the Green's function of the semi-infinite leads, and defining the Green's function of the central region

$$G_C(E) = (EO_C - H_C - \Sigma_L(E) - \Sigma_R(E))^{-1} \tag{3.85}$$

the transmission probability is given by [99]

$$T(E) = Tr\left[G_C(E)\Gamma_L(E)G_C^\dagger(E)\Gamma_R(E)\right]. \tag{3.86}$$

In this equation the transmission coefficient, $T(E)$, is expressed by the Green's functions of the device and the semi-infinite leads. The Green's function of the semi-infinite leads, g_X, is calculated by the decimation [116] technique.

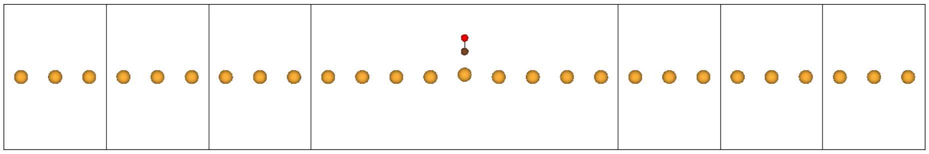

Figure III.5: Structure of the Au-CO system. The division into lead and device regions, displayed generally in Figure III.4, is shown.

3.5.2 Results

To study the convergence of transport calculations we used an Au-CO system. This is a linear chain of Au atoms to which a CO molecule has been adsorbed (see Figure III.5). This system has been studied in [3] and we adopted the geometry of the atoms from that source. These are relatively simple systems but they allow us to study the convergence properties using large basis sets. The increased computational cost associated with systems that contain more atoms would prevent us from a systematic enlargement of the bases. An additional system, Al-C-Al, was also used. For brevity, only the results for the Au-CO system are presented here; for the remainder, please see the published results in Ref. [117].

In the calculations we first determine the self-consistent potential by diagonalizing the Kohn-Sham Hamiltonian (Equation 3.78) in the region that includes three layers in the left, three layers in the right, and the central region (see Figure III.5) using periodic boundary conditions on the computational cell. Numerical tests show that adding these three layers is sufficient to obtain the converged self-consistent potential in the middle region containing layers 2-3, the device and layers 5-6 (between the planes in Figure III.5). The self-consistent potential obtained in this way does not change in the middle region if further layers are included in the computational cell. That is, this self-consistent potental is the same as it is in the infinite system containing the semi-infinite leads and the device. Using the self-consistent potential of this middle region one can calculate the matrix elements needed in the transmission calculations using the basis functions defined above.

First we calculated the transmission coefficient using AOs. In these calculations both the self-consistent ground state and the transmission coefficient are calculated using the same AO basis set; that is, the transmission coefficient has a twofold dependence on the basis set.

There are three parameters that influence the convergence behavior: R_{cutoff}, l_{max} and p_{max}. Out of the three, p_{max}, the number of orbitals per angular momentum, is the most sensible to vary and the easiest to change. We have kept $l_{max} = 2$ and $R_{cutoff} = 5$ Å as these are typical choices in AO calculations and give good ground state properties for these systems. Figure III.6 shows the transmission as a function of energy (relative to the Fermi energy) for $p_{max} = 1, 2, 3$. Considering the value of the transmission at the Fermi energy, the calculated conductances are shown in Table III.3 (Case I). The transmission curves obtained for different p_{max} values are quite different, and the convergence as a function of the number of basis states is slow, similar to what has been observed in previous calculations [113, 3]. For clarity Figure III.6 only shows the results up to $p_{max} = 3$, as the transmission for $p_{max} = 4$ and $p_{max} = 5$ is still changing; that is, convergence has not been reached. Adding more AOs is difficult because the computational time becomes prohibitively large. The slow convergence is especially noticable and is due to the fact that the d $l = 2$ states are not included in these calculations. Without the d states, a truncation that is often used in transport calculations, the convergence is much worse. The inclusion of the

Table III.3: Convergence of conductance (in units of G_0). N_C and N_L denotes the basis dimension in the central region and in the unit cell of the lead.

		Au-CO		
		N_C	N_L	G
Case I	$p_{max} = 1$	99	27	0.244
	$p_{max} = 2$	198	54	0.248
	$p_{max} = 3$	297	81	0.208
	$p_{max} = 4$	396	108	0.204
	$p_{max} = 5$	495	135	0.212
Case II	$p_{max} = 1$	99	27	0.185
	$p_{max} = 2$	198	54	0.078
	$p_{max} = 3$	297	81	0.039
	$p_{max} = 4$	396	108	0.017
	$p_{max} = 5$	495	135	0.001
Case III	1	50	25	0.001
	2	60	30	0.001
	3	70	35	0.001
	4	80	40	0.001
	5	100	50	0.001

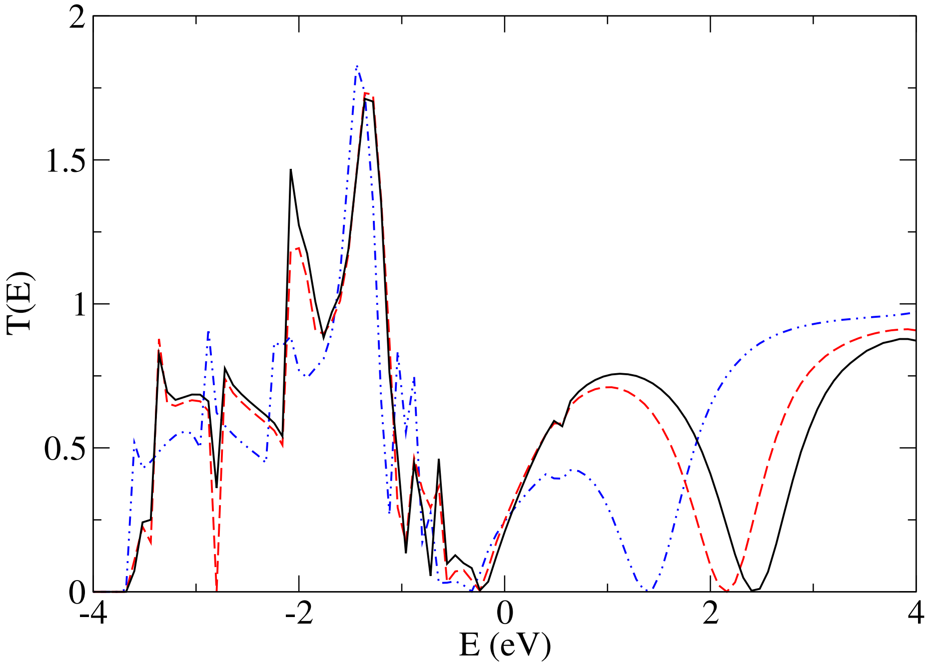

Figure III.6: Transmission vs. relative energy using an atomic orbital basis. In this plot, both the ground state and the conductance calculations were performed on the same AO basis ($p_{max} = 1$ blue dot-dashed line, $p_{max} = 2$ red dashed line, $p_{max} = 3$ black solid line).

d states is computationally demanding, and by omitting them the basis dimensions would decrease to less than half of what is shown in Table III.3. The convergence of the conductances in the table shows a very similar pattern to what has been discussed above concerning the transmission curves.

Next, we will study the effect of varying the basis just in the transmission calculation, and leaving the ground state basis fixed. To this end we calculate the self-consistent potential without employing AOs, instead using the Lagrange function method [92] which provides an accurate self-consistent potential. Any other approach, e.g. plane wave basis calculations could have been used for this purpose; the main point is that the self-consistent potential has been calculated independently of the basis function sets that are to be tested in the transmission calculations. For all subsequent calculations, we will fix the ground state potential to that obtained by the Lagrange function basis. This allows us to see just the influence of varying the AO basis in the transmission calculation.

Figure III.7 shows the basis set dependence of the AO-based calculation for the fixed self-consistent potential. Compared to the previous case, the convergence is much faster, and a much smaller basis set is sufficient to calculate accurate transport properties. The conductance values in Table III.3 (Case II) nicely converge with the number of basis states. One can notice that the converged values are different from those shown in Case I. This shows that a large part of the basis set error in the previous case is due to the basis set dependence of the self-consistent potential. This is mostly due to the difference of the Fermi energies obtained by the Lagrange basis grid and by the AO self-consistent potential calculations. Due to the Fermi energy

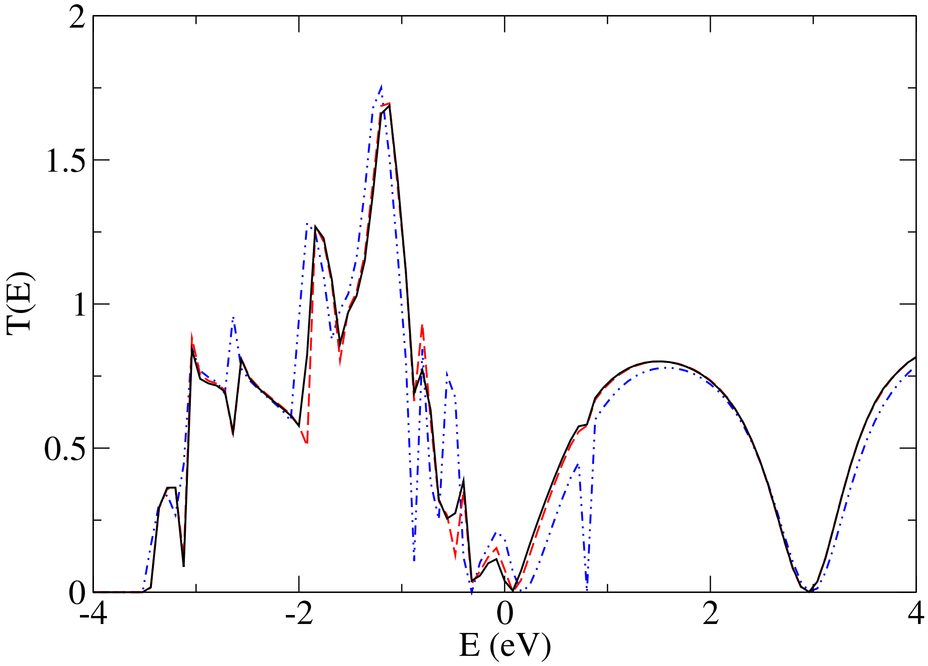

Figure III.7: Transmission vs. relative energy using an atomic orbital basis. In contrast with Figure III.6, here the ground state potentials for all curves were the same, calculated with a Lagrange basis for high accuracy.

difference the curves are slightly shifted leading to this shift in the conductances. It is interesting to note the strong dependence of the results on R_{cutoff}. Figure III.8 shows the same calculation as Figure III.7 using AOs with R_{cutoff}=3.5 Å. The smaller radius does not significantly affect the energy of the system, but the calculated transmission has substantially changed, especially in the higher energy region.

We have also investigated the effect of augmenting the AO with floating Gaussian states. The calculations show that these states do not significantly improve the convergence. For example, adding a grid of Gaussians to $p_{max} = 2$ (Figure III.9) does not substantially change the transmission coefficient. Adding a Gaussian grid to AOs which have a smaller cutoff radius changes the results somewhat more (these results are not shown here) but it is found to be hard to optimize their positions and

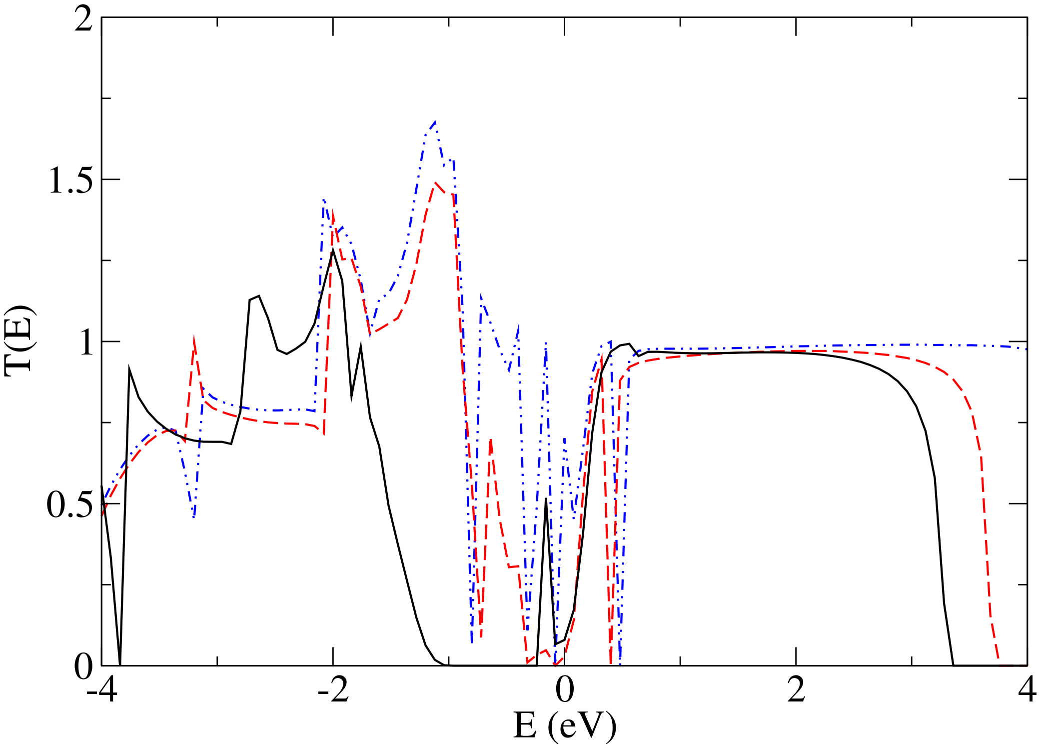

Figure III.8: Same as Figure III.7, except that the atomic orbital bases used were spatially smaller.

widths. Moreover, although adding floating Gaussians have somewhat changed the transmission coefficients, no clear convergence pattern could be found.

Next we show our results using the box basis states. The convergence of the transmission is shown in Figure III.10 and the conductances can be seen in Table III.3 (Case III). The most important result of this case is that the transmission converges rapidly and systematically as a function of the number of basis states. One can also note that the number of basis states needed for convergence is much less than in the AO calculations. The converged box basis calculation is compared to the best AO results in Figure III.11. The agreement is good; for a better agreement probably more AOs should be included, which as we have already emphasized, is computationally unfeasible.

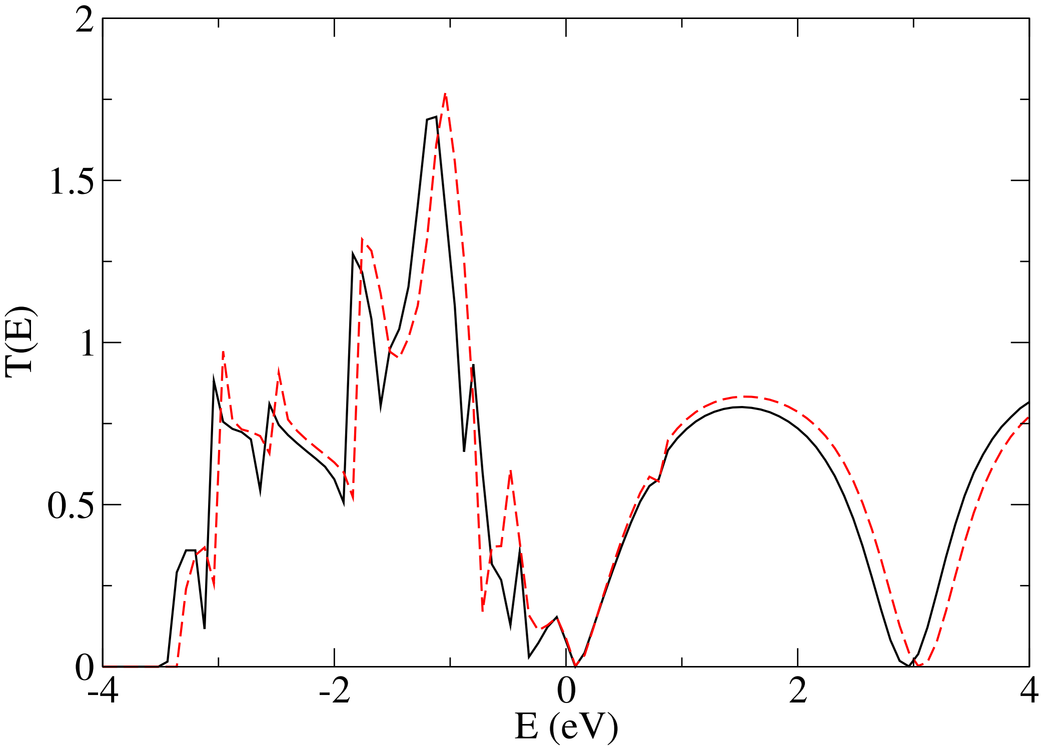

.

Figure III.9: Transmission calculation with the Gaussian-augmented AO basis. For $p_{max} = 2$ the transmission is calculated with (dashed red line) and without (solid black line) the addition of a uniform grid of Gaussian basis functions.

Finally, we compare our results to the benchmark calculation published in [3]. In the benchmark paper the transmission functions are calculated using two different density functional theory methods, an ultrasoft pseudopotential plane-wave code in combination with maximally localized Wannier functions and the norm-conserving pseudopotential code SIESTA which applies an atomic orbital basis set. Figure III.12 compares the results of the benchmark calculation to our box basis results. The agreement is very good.

The development of efficient quantum transport calculations [99, 100, 101, 102, 104, 105, 106, 107, 108, 103, 109, 110, 111, 112] is an area of very active research. These calculations have yet to reach the accuracy and efficacy of ground state DFT

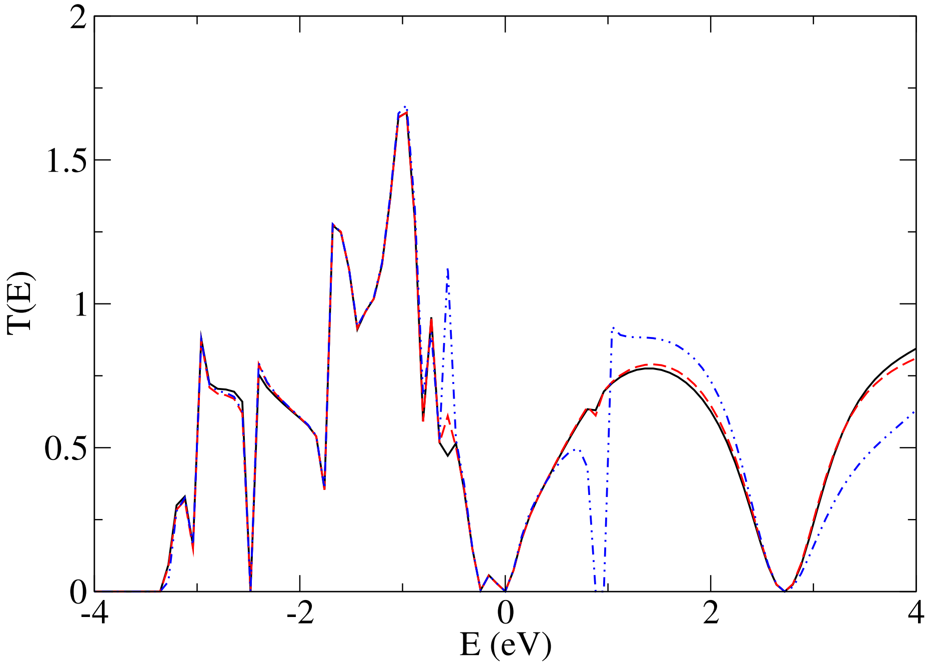

Figure III.10: Convergence of the transmission using box basis states. The curves correspond to the number of box basis states as defined by sets 1 (blue dot dashed line), 2 (red dashed line) and 3 (black solid line) in Table III.3 (Case III). The results obtained by using larger basis sets (4 and 5 in Table III.3) are identical with the black solid line within the resolution of the figure.

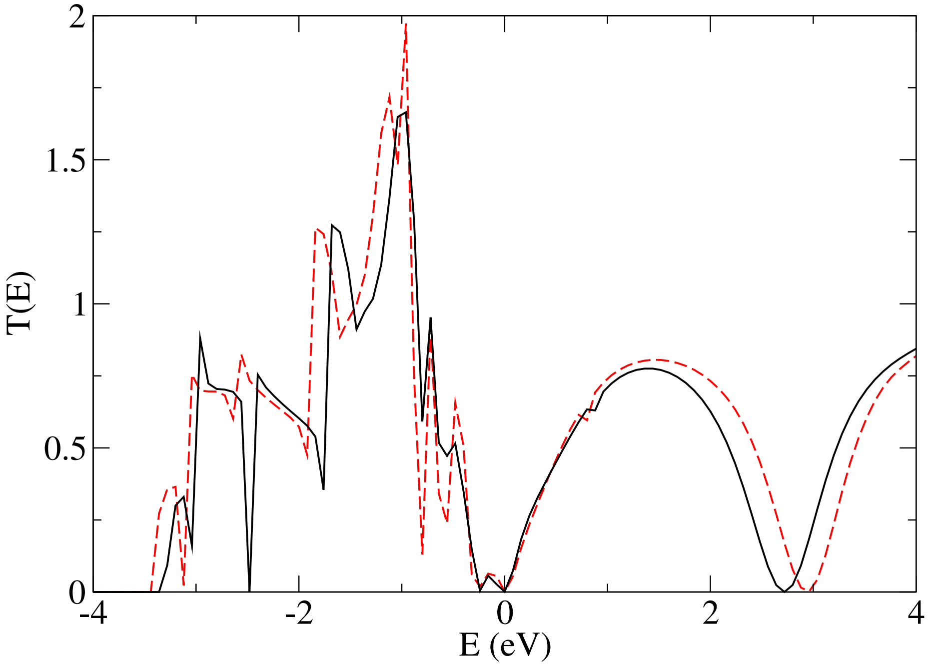

Figure III.11: Comparison of the results obtained by the box basis (solid black line) and the AO (dashed red line).

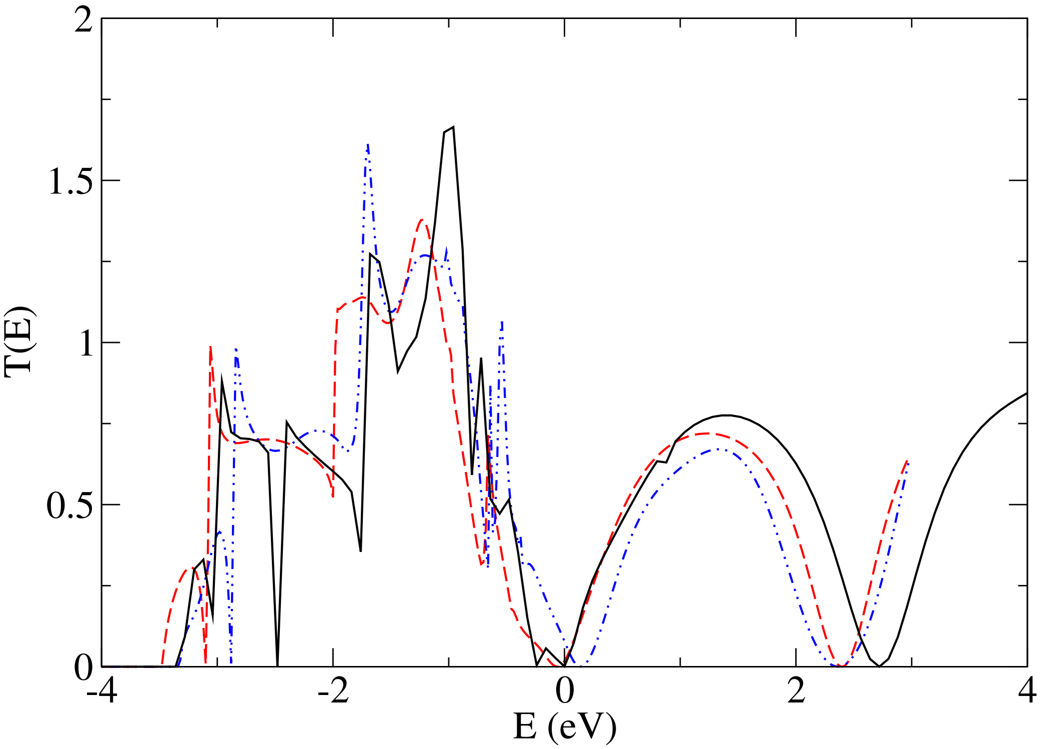

Figure III.12: Comparison of the box basis calculation (solid black line) to benchmark results. The blue dot dashed line is the Wannier, the red dashed line is the AO calculation of Ref. [3].

calculations. Using the combination of the non-equilibrium Green's function formalism and ground state density functional theory we have studied the convergence and basis set dependence of quantum transport calculations.

Atomic orbitals are widely used in NEGF implementations, but the convergence of transport properties with respect to the number of basis states is slow. Examples in this section show that this is partly due to the basis set dependence of the self-consistent potential. In other words, if the self-consistent potential is accurately calculated then much fewer AOs are needed in the calculation of the transport properties. The calculation of the transport coefficient is a time consuming part of the transport calculations because it involves many inversions of large matrices and this has to be repeated for many energy values.

The box basis orbitals lead to much faster convergence on a much smaller basis than the AOs. The typical number of basis states per electron orbital is about 2-3. This significantly reduces the computational cost. Another useful property of the box basis is that by increasing the number of basis states the Hilbert space is enlarged and the transport coefficients systematically converge. In the case of AOs the transport coefficients always change and due to computational limitations the same level of accuracy cannot be reached. The accuracy of box basis states is due to the facts that (1) they are spatially extended and can represent scattering states efficiently and (2) the box basis states are optimized for the converged self-consistent potential.

3.6 Summary

Based on the discussion and results of this chapter, it is clear that a localized basis such as atomic orbitals is a poor choice for field emission calculations. In field emission the electron density is continuous in the vacuum region, and so a delocalized basis is more appropriate. In addition, the finite size of our systems and lack of periodicity means that plane waves are also a bad choice. From this we choose to use a real-space grid basis. In particular, the Lagrange function grid is used, due to the advantages discussed in Section 3.3.2.

CHAPTER IV

COMPLEX ABSORBING POTENTIALS

This chapter provides an introduction to complex absorbing potentials. It is explained in the context of an example: one-dimensional scattering. The theory extends to more complex cases, as shown in the following section on the calculation of self-energy matrices using CAPs. Both of these examples provide important tests of the capabilites of complex absorbing potentials. These tests are vital since CAPs are used in all of the field emission calculations presented in this dissertation. The particular types of tests were chosen because they have well-known benchmarks in the literature to which the results can be compared. No such benchmarks yet exist for field emission. Even so, the tests presented in this chapter still validate the performance of CAPs in a range of calculations, and so provide confidence in their use for field emission.

4.1 An introduction to complex potentials via 1D scattering

In this section the usefulness of complex absorbing potentials for solving the one-dimensional time-independent Schrödinger equation is demonstrated. This simple approach may be used with arbitrary potentials. To illustrate the method, it is applied to the quantum scattering problem, using three potentials. In the scattering region, the method produces both wave functions and transmission coefficients that are in good agreement with analytical results.

Our goal here is to solve the time-independent Schrödinger equation

$$-\frac{\hbar^2}{2m}\frac{\partial^2\Psi(x)}{\partial x^2} + V\Psi(x) = E\Psi(x) \tag{4.1}$$

for the eigenstates $|\psi(x)\rangle$ with a definite energy E representing the continuous part of the spectrum. In typical physical applications the potential is nonzero only in a finite region around the origin (see Figure IV.1) and we are interested in the scattering wave function which describes the reflection and transmission probability of an incident particle on that potential. For the simplest potentials $V(x)$, (e.g., square well, potential step, etc.) these continuum eigenstates can be found exactly.

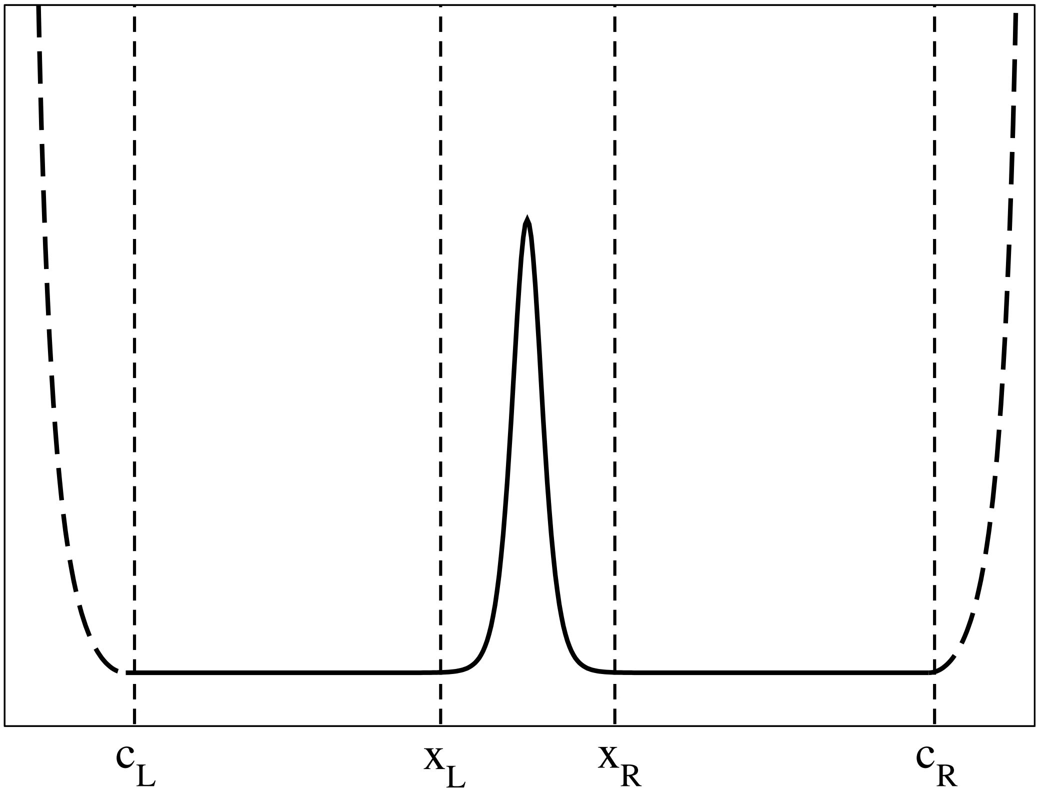

Figure IV.1: Use of complex potentials with a scattering potential. The solid line represents a scattering potential, while the dashed lines indicate pure imaginary potentials. These imaginary potentials absorb the wavefunction in asymptotic regions, allowing a finite representation of the scattering problem.

Beyond these few elementary exactly solvable problems, the determination of continuum states is difficult. The major source of the difficulty is that the wave function is nonzero in the entire space ($-\infty < x < \infty$) and basis function or finite difference expansions (see below) lead to infinite-dimensional representations.

In Equation 4.1, the wave function is complex; both its real and imaginary parts are in general nonzero in the entire space. The potential is usually (in most textbooks) a purely real function. Complex potentials can also be used and can be useful in the Schrödinger equation.

Assuming that the potential is real, the conservation of the probability current density $\mathbf{j}$ follows from the Hermiticity of the Hamiltonian. For a probability density $|\Psi|^2$ that is constant in time,

$$\nabla \cdot \mathbf{j} = 0, \qquad \mathbf{j} = \frac{\hbar}{2mi}(\psi^* \nabla \psi - \psi \nabla \psi^*) \tag{4.2}$$

If instead the potential is complex, the Hamiltonian is not Hermitian. As a result, using the same steps as in the standard textbooks to derive the current conservation now yields a different result. The time-dependent Schrödinger equation is

$$i\hbar \frac{\partial \Psi}{\partial t} = \frac{-\hbar^2}{2m} \nabla^2 \Psi + V\Psi \tag{4.3}$$

Multiplying Equation 4.3 by Ψ^*, its conjugate by Ψ, and subtracting the two resulting equations, one obtains

$$i\hbar\frac{\partial|\Psi|^2}{\partial t} = -\nabla \cdot \mathbf{j} + 2|\Psi|^2 Im(V) \tag{4.4}$$

If the probability density $|\Psi|^2$ is not changing in time,

$$\frac{\partial|\Psi|^2}{\partial t} = 0 \tag{4.5}$$

and so

$$\nabla \cdot \mathbf{j} = 2|\Psi|^2 Im(V). \tag{4.6}$$

This equation shows that the current is not conserved if the imaginary part of the potential is nonzero. Depending on the sign of the imaginary part, this can represent sinks and sources which allow probability density to be absorbed and injected into the system. The usefulness of this concept has been realized in different areas of physics. Examples include chemical reaction rate studies [118], time-dependent wave packet calculations of reactive scattering [119, 120], optical model calculations in nuclear physics [121], theory of atomic multiphoton ionization [122], simulations of scanning tunneling microscopy [123], and electron transport in nanostructures [124]. In the case of scattering, the addition of a pure imaginary potential to the scattering potential allows the wave function to be absorbed in the asymptotic regions, avoiding the need for infinite-dimensional representations.

4.1.1 Calculating the wavefunction and transmission coefficient

Referring again to Figure IV.1, we want to calculate the scattering wave function $\psi_c(x)$ in the central $[x_L, x_R]$ interval for a particle in a potential defined as

$$V(x) = \begin{cases} V_L & -\infty < x < x_L \\ v(x) & x_L \leq x \leq x_R \\ V_R & x_R < x < +\infty \end{cases} \tag{4.7}$$

where V_L and V_R are constant potentials in the asymptotic regions and $v(x)$ is the central scattering potential. The scattering wave function is the solution of the Schrödinger equation

$$H|\psi\rangle = E|\psi\rangle, \qquad H = T + V(x) \tag{4.8}$$

Assuming that an incident particle comes from the left, the scattering wave function is of the form

$$\psi(x) = \begin{cases} A\mathrm{e}^{ik_L x} + r\mathrm{e}^{-ik_L x} & -\infty < x < x_L \\ \psi_c(x) & x_L \leq x \leq x_R \\ t\mathrm{e}^{ik_R x} & x_R < x < +\infty \end{cases} \tag{4.9}$$

where

$$k_L = \sqrt{\frac{2m(E - V_L)}{\hbar^2}}, \qquad k_R = \sqrt{\frac{2m(E - V_R)}{\hbar^2}} \tag{4.10}$$

Once ψ_c is known, requiring the continuity of the wave function and its derivatives at x_L and x_R yields the reflected wave amplitude r and transmitted wave amplitude t. The scattering wave function ψ is then known for all x.

The calculation of the scattering wave function, however, is only possible for a few simple analytically solvable examples (e.g. step potential, square well potential, etc.). For a general $v(x)$ scattering potential the calculation of the wave function $\psi_c(x)$ is difficult because the boundary conditions at x_L and x_R are not known. That is the major complication in the scattering problems that is not present in bound state problems. In bound state problems (e.g., harmonic oscillator or hydrogen atom) the boundary conditions are given by $\psi_c(x_L) = 0$ and $\psi_c(x_R) = 0$ and simple finite difference or basis function expansions can be used.

As we are only interested in the wave function $\psi_c(x)$ in the $[x_L, x_R]$ interval we can modify the potential outside of that region, provided that we still obtain the same solution in $[x_L, x_R]$. In particular, we can add a pure imaginary potential to the Hamiltonian outside of the $[x_L, x_R]$ region to damp the wave function. In the imaginary potential the wave fuction will decay to zero at c_L and c_R (see Figure IV.1). We denote the imaginary potential as $-iW_L$ in the $[c_L, x_L]$ region and $-iW_R$ in the $[x_R, c_R]$ region. The spatial form of these potentials will be given below. The resulting Hamiltonian is

$$H = H_0 + V - iW_L - iW_R \tag{4.11}$$

where $H_0 = T$ is the free particle Hamiltonian. The advantage of this Hamiltonian is that due to the complex absorbing potentials the wave function decays to zero in the left and in the right regions. In other words, the complex absorbing potential forces the scattering solutions to behave like bound states. In this way (1) *instead of the infinite space we can work in a finite computational domain*; (2) *we can represent the scattering wave function in the same way as bound states, that is by expanding the* *scattering wave function on a finite basis.* In summary, with the complex absorbing potentials the scattering problem is transformed into a bound state problem.

We are looking for the wave function ψ for a given energy E as the solution of the time-independent Schrödinger equation

$$(H_0 + V - iW_L - iW_R)|\psi\rangle = E|\psi\rangle. \tag{4.12}$$

Now define a left incident solution in the left asymptotic region by

$$\phi(x) = \begin{cases} \mathrm{e}^{ik_L x} & -\infty < x < x_L \\ 0 & x_L \leq x < +\infty \end{cases} \tag{4.13}$$

This wave function obeys the time-independent Schrödinger equation, with free particle Hamiltonian $H_0 = T$ for a given energy E

$$H_0|\phi\rangle = E|\phi\rangle. \tag{4.14}$$

Subtracting equation 4.14 from equation 4.12 gives

$$(H_0 + V - iW_L - iW_R - EI)(|\psi\rangle - |\phi\rangle) = -(V - iW_L - iW_R)|\phi\rangle \tag{4.15}$$

where I is the identity matrix. Now we can extract the scattering wave function ψ with the help of the Green's function G, defined as

$$G \equiv (H_0 + V - iW_L - iW_R - EI)^{-1} \tag{4.16}$$

Multiplying both sides of equation 4.15 by G leads to

$$|\psi\rangle = |\phi\rangle - G(V - iW_L - iW_R)|\phi\rangle \tag{4.17}$$

which gives the desired wavefunction for the particle. In the region of interest $[x_L, x_R]$, $|\phi\rangle = 0$, $V|\phi\rangle = 0$ and $iW_R|\phi\rangle = 0$ and the above equation simplifies to

$$|\psi\rangle = G(iW_L)|\phi\rangle \tag{4.18}$$

The transmission coefficient T is given by

$$T = \frac{j_T}{j_I} \tag{4.19}$$

where j_T and j_I are the transmitted and incident currents, respectively.

It is convenient if the incoming current is set to be $j_I = 1$, since then $T = j_T$. To do this, note that we are free to choose the amplitude of the incident wave function. Since

$$j_I = |A|^2 \frac{\hbar k_0}{m} \tag{4.20}$$

the choice $A = \sqrt{m/\hbar k_0}$ gives $j_I = 1$. With this choice of A, all that remains is to find j_T using equation 4.2.

4.1.2 Form of the complex potentials

Complex potentials not only absorb the outgoing waves but can also produce reflections themselves. The construction and optimization of reflection-free CAPs is therefore pursued by many research groups. Many different forms of pure imaginary potential have been investigated, including linear [125], power-law [126, 127], polynomial [128] and other parametrized functional forms (see [129] for a recent review). Besides purely imaginary potentials, complex potentials have also been investigated [130]. Here (and elsewhere in the dissertation) we will adopt the CAP suggested in [131]. This negative, imaginary CAP is derived from a physically motivated differential equation and its form is

$$-iw(x) = -i\frac{\hbar^2}{2m}\left(\frac{2\pi}{\Delta x}\right)^2 f(y) \tag{4.21}$$

where x_1 is the start and x_2 is the end of the absorbing region, $\Delta x = x_2 - x_1$, c is a numerical constant, m is the electron's mass and

$$f(y) = \frac{4}{(c-y)^2} - \frac{4}{(c-y)^2}, \qquad y = \frac{c(x-x_1)}{\Delta x}. \tag{4.22}$$

This CAP goes to infinity at the end of the absorbing region and is therefore exactly transmission free. The CAP contains only one parameter, the width of the absorbing region Δx. Its reflection properties are guaranteed to improve as this parameter is increased.

Figure IV.2 shows the above CAP together with electron density calculated solving a one-dimensional model, scattering on a potential step. In the middle region, where the CAP is zero, the calculated and exact densities are equal. In the asymptotic region the wave function is absorbed by the CAP and the density gradually decreases to zero.

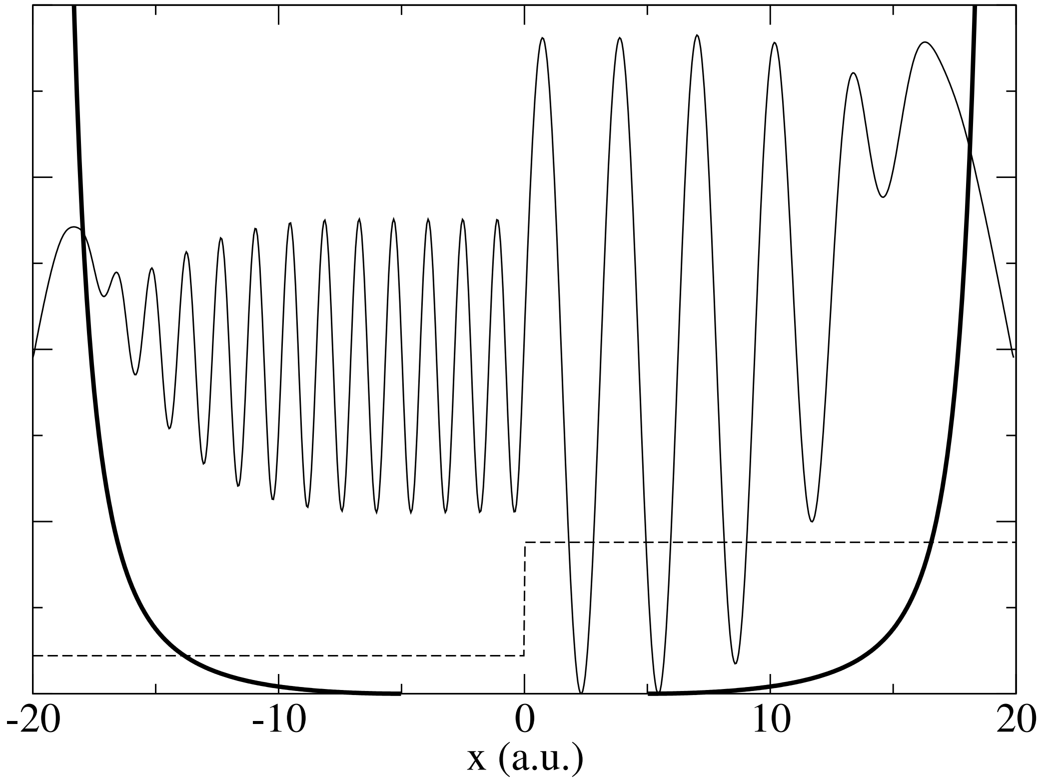

Figure IV.2: Complex absorbing potential in a one-dimensional scattering example.

4.2 Further tests of complex potentials: calculation of self-energy matrices for transport calculations

A method to evaluate self-energy matrices used in the Green's function formulation of transport calculations is now presented. Green's functions, self-energies, and the NEGF formalism were discussed in Section 3.5.1. By adding a complex absorbing potential to the Hamiltonian of the semi-infinite lead, the problem of inverting an infinite dimensional matrix is transformed into a finite dimensional eigenvalue problem. The self-energies are calculated for all energies at once and can be tabulated for a given system. Test examples are presented to show the accuracy of the approach.

Motivated by experimental advances, methods for quantum transport calculations have developed at a great pace in recent years. Most of the approaches are based on the Landauer-Büttiker formalism [132], where the central quantity is the electron transmission probability $T(E)$. There are various approaches used to calculate $T(E)$, e.g. the non-equilibrium Green's function (NEGF) method [101, 102, 104, 105, 106, 107, 108, 103, 109, 110, 111], the Lippmann-Schwinger approach [133] and the wave function matching technique [134].

Unlike conventional electronic structure calculations where one can use closed systems or periodic boundary conditions, in quantum transport calculations one has to deal with an open system where the device is connected to semi-infinite leads. The lead is usually built of periodically repeated cells and the system can be divided into left lead, device (which may include several layers or cells of the lead) and the right lead (see Fig. IV.3). The transmission probability can then be calculated using a finite

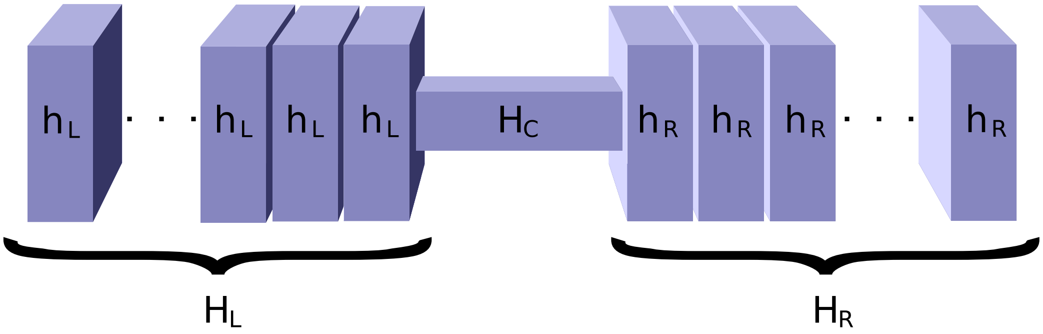

Figure IV.3: Schematic diagram of a two-probe device. The device is modeled by two semi-infinite electrodes (L and R) and a central region (C). The electrodes are divided into principal layers (blocks) that interact only with the nearest-neighbor layers.

computational cell containing the device, provided that the boundary conditions are known on the surfaces dividing the device and the leads. These boundary conditions can be given either by the wave function or by the Green's function of the leads. The problem is that these boundary conditions have to be known at any energy for which $T(E)$ is to be calculated.

In NEGF calculations these boundary conditions enter in the form of self-energies. Therefore the self-energy calculations are an indispensable part of transport calculations and various methods have been developed for this purpose in the past. The common feature of these methods is that they have to be repeated for each energy of interest. The simplest method to calculate the Green's function of the lead is the iterative method [135]. It starts with the calculation of the Green's function for a single cell of the periodic lead and adds more and more cells until convergence. The convergence however is extremely slow because the termination of the infinite lead at a finite distance generates reflections from the artificial boundary and this effect will only be negligible if the boundary is far away. The decimation method [116] is a clever variant of the iterative approach which greatly speeds up the convergence by increasing the lead in a recursive way. The decimation method is a very efficient way to calculate the Green's function of the lead and is used in many quantum transport codes. Other approaches calculate the Green's function by solving quadratic eigenvalue problems [111, 136, 137]. The review paper [135] gives a pedagogical introduction to these methods, shows the equivalence of the different approaches and an extensive source of references of self-energy calculations.

In this section we show that a complex absorbing potential, introduced in the previous section, can be used as a very efficient tool to calculate the Green's function and the self-energy of the leads. As the self-energies are needed at many different energies, their calculation is often the dominant part of transport calculations. In the approach suggested in this paper one can obtain the self-energy for all energies at once. This is achieved by adding a CAP to the Hamiltonian of the leads. The CAP transforms the infinite lead into a finite system. The Hamiltonian of the lead then can be diagonalized and the Green's function can be calculated using a spectral representation for any energy.

In a sense the approach shown here is the opposite of what the work in Ref. [138] pursued. In [138] a complex potential was derived approximately from the self-energies of the leads. The obtained complex potential was energy independent and nonlocal. By adding the the derived complex potential to the Hamiltonian of the device the need for self-energies is bypassed, greatly simplifying the calculations. In this section a complex potential is explicitly added to the leads *to calculate* the energy dependent self-energy matrices. The energy dependence of the calculated self-energy matrices is simple and the computation associated with the leads is decoupled from the calculation of the device, just like in [138].

4.2.1 Self energies of the leads with CAP

By adding the CAP from Equation 4.21 to the Hamiltonian of the leads one obtains

$$H'_L = H_L - iW_L(x) \qquad H'_R = H_R - iW_R(x), \tag{4.23}$$

where W_L and W_R are the matrix elements of the complex potential on the left and the right. Assuming that the basis states only connect the neighboring cells in the lead, these matrices will have the same block tridiagonal structure as the lead's Hamiltonian

$$H_R = \begin{pmatrix} h_R^{00} & h_R^{10\dagger} & 0 & 0 \\ h_R^{10} & h_R^{00} & h_R^{00\dagger} & 0 \\ 0 & h_R^{10} & h_R^{00} & \dots \\ 0 & 0 & \dots & \dots \end{pmatrix}, \tag{4.24}$$

but for the nonperiodic complex potential the matrices in the diagonals will not be identical:

$$W_R = \begin{pmatrix} w_R^{00} & w_R^{10\dagger} & 0 & 0 \\ w_R^{10} & w_R^{11} & w_R^{21\dagger} & 0 \\ 0 & w_R^{21} & w_R^{22} & \dots \\ 0 & 0 & \dots & \dots \end{pmatrix}. \tag{4.25}$$

These are finite dimensional Hamiltonians; beyond the range of the complex potential, the lead is effectively cut off. To simplify the calculations we assume that the complex potential starts one cell away from the central region on both sides of the central region. With this choice, assuming that the basis functions in the leads only connect neighboring cells, H_{LC} and H_{RC} will not contain contributions from the complex potential. The Hamiltonian of the system is now

$$H' = \begin{pmatrix} H'_L & H_{LC} & 0 \\ H^\dagger_{LC} & H_C & H^\dagger_{RC} \\ 0 & H_{RC} & H'_R \end{pmatrix}. \tag{4.26}$$

Recall from Section 3.5.1 that we define the self energies of the leads ($X = L, R$) as

$$\Gamma_X(E) = i\left(\Sigma_X(E) - \Sigma^\dagger_X(E)\right) \tag{4.27}$$

where

$$\Sigma_X(E) = (EO_{XC} - H_{XC})g_X(E)(EO_{XC} - H_{XC}) \tag{4.28}$$

and where

$$g_X(E) = (EO_X - H_X)^{-1} \tag{4.29}$$

is the Green's function of the semi-infinite leads. The transmission probability, the Green's function of the central region and other quantities can be calculated in the same way as before by replacing the leads' Green's functions in the self-energies in Equation 4.27 by

$$g'_X(E) = (EO_X - H'_X)^{-1}. \tag{4.30}$$

By adding the complex potential to the Hamiltonian of the lead the semi-infinite Hamiltonian is transformed into a finite Hamiltonian. The simplest way to calculate Green's functions of the leads is to diagonalize the complex Hamiltonians H'_L and

H'_R:

$$H'_X C_X = E_X O_X C_X \qquad (X = L, R). \tag{4.31}$$

The Green's function of the leads now can be calculated by the spectral representation

$$(g_L)_{ij} = \sum_k \frac{C_{Xik} C_{Xjk}}{E - E_{Xk}} \tag{4.32}$$

where C_{Xik} is the ith component of the k-th eigenvector belonging to eigenvalue E_{Xk}. As the Hamiltonian matrix of the lead is complex symmetric, the left and right eigenvalues are equal and the left and right eigenvectors are complex conjugates of each other. For a given lead this diagonalization only has to be done once in the beginning of the calculations and the self-energies are then available for any desired energy. The Hamiltonian and overlap matrices of the leads are in block-tridiagonal form and this special sparse property allows efficient iterative diagonalization. If the size of the eigenvalue problem becomes too large then one has to calculate the Green's function by direct inversion. Another possibility is to calculate only the eigensolutions whose contribution dominate the spectral representation and introduce some effective truncation procedure.

4.2.2 Results

In this subsection we present our test calculations for different systems. To demonstrate the effectiveness of our approach we have calculated the Green's functions of the leads by decimation [116] and by using the CAP approach and compared the transmission probabilities obtained by using the two different methods. As the CAP approach only affects the Green's functions of the leads, the device part is irrelevant and we have restricted our calculations to simple devices and tested the accuracy of the method for various leads.

In these tests we used density functional theory (DFT) to describe the electronic structure of the leads and the device. We first calculated the self-consistent potential in the leads and in the device and then set up the Hamiltonian and overlap matrices. The DFT calculation was implemented on the Lagrange function basis [70]. We have restricted the basis functions in such a way that only the nearest-neighbor blocks in the lead were connected in the Hamiltonian leading to block tridiagonal matrix representations. This restriction allows us to use the decimation technique to calculate the leads' self energies and compare the results to those obtained by the CAP approach.

4.2.2.1 Conductance of monoatomic aluminium wire

Our first example is a monoatomic Al wire (placing Al atoms 2.4 Å apart). Both the decimation and the CAP approaches use the same basis and therefore, apart from the complex potential in the CAP case, the Hamiltonian and overlap matrices are identical. The decimation provides well converged self-energies after about 25 iterations and we consider this the "exact" results and compare it to the CAP results. Fig. IV.4 shows the convergence of the CAP results as a function of the range of the complex potential (in units of number of lead blocks). As mentioned before, the increase of the CAP range leads to the decrease of reflections and the CAP results quickly converge to the exact values. In the CAP approach, the leads' Green's

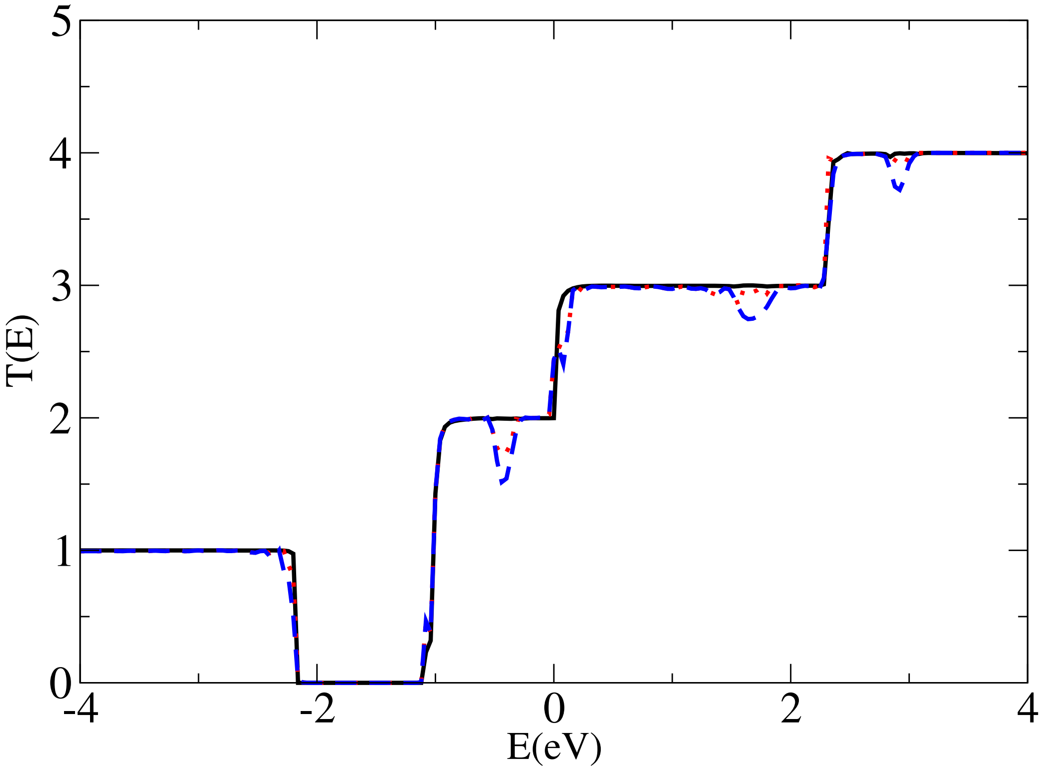

Figure IV.4: Transmission probability of a monoatomic Al wire. The result obtained by the decimation method (solid black line) is compared to the CAP of different ranges (blue dashed line two blocks, red dotted line four blocks). The CAP results using six blocks is indistinguishable from the decimation results within the line width on the figure.

functions were expressed by their spectral representation, so after the eigenvalue problem (Equation 4.31) was solved the self-energies were available for any energy at no extra cost.

We also tested the direct inversion which has to be repeated for all energies of interest. Both methods give identical results. We note that direct inversion is still about 10 times faster than decimation and in larger lead blocks the speed-up is expected to be even more significant.

4.2.2.2 Conductance of monoatomic C wire between Al leads

The calculation of the conductance of a monoatomic carbon wire is a popular test case of transport calculations [139, 140, 141]. In this test case a straight wire of seven carbon atoms is attached to Al(100) electrodes (lattice constant 4.05 Å). The C-C distance is fixed to 1.32 Å and the distance between the ends of the carbon chain and the first plane of Al atoms is 1 Å. The Al unit cell contains 18 atoms in four layers with identical unit cells in the left and right leads.

Fig. IV.5 shows the transmission probability as a function of the energy. The CAP and decimation results are in complete agreement.

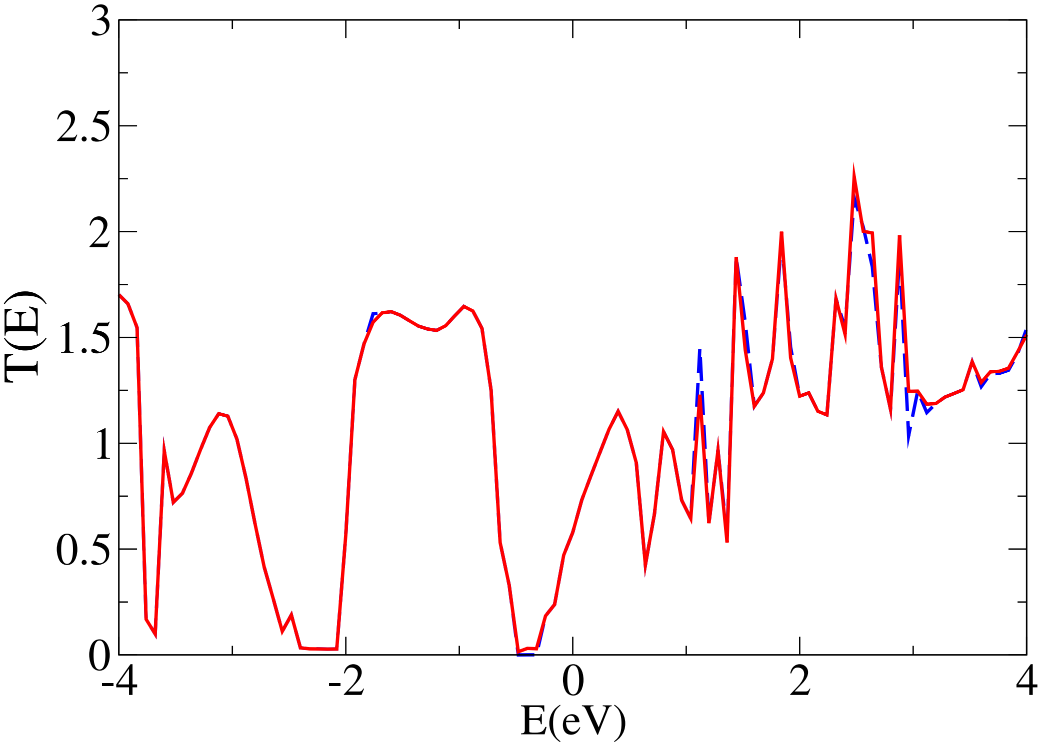

Figure IV.5: Transmission probability of a 7 atom monoatomic C wire sandwiched between Al(100) electrodes. The result obtained by the decimation method (solid red line) is compared to the CAP result (solid blue line) obtained by using 6 lead blocks.

4.2.2.3 Conductance of carbon nanotubes

In this example we calculated the conductance of carbon nanotubes and compared the transmission obtained from CAP and decimation. The agreement between the two approaches (Fig. IV.6) is again excellent. Next, we test the CAP method for

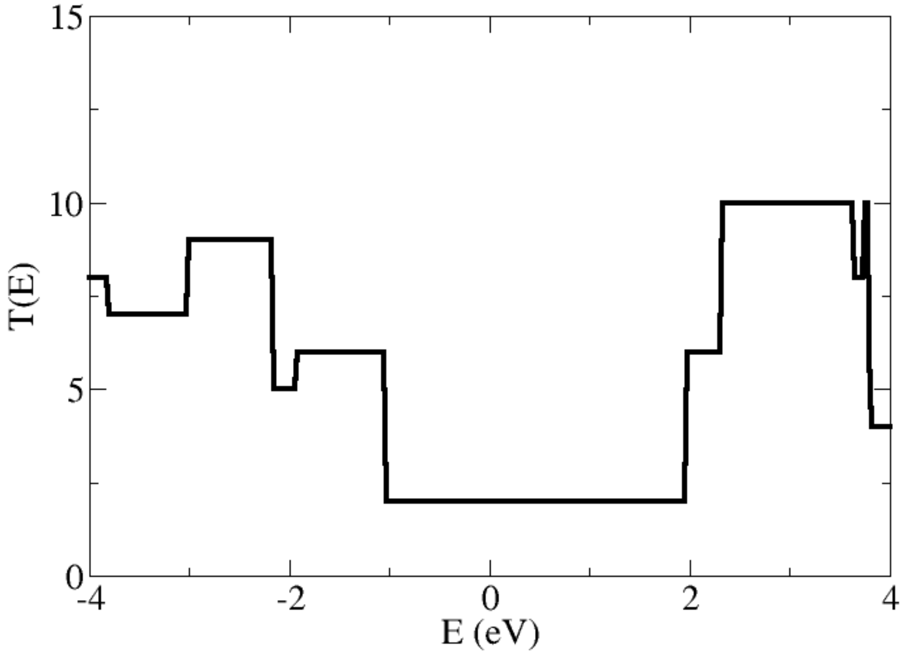

Figure IV.6: Transmission probability of a (10,10) carbon nanotube. The decimation and CAP results are in perfect agreement.

a carbon nanotube with a Hückel Hamiltonian. The tight-binding matrix elements are taken from [142] and the parametrization used is from [143]. In this case, we did not explicitly calculate the matrix elements of the complex potentials but in the spirit of the Hückel approach we simply added the $W(x)$ to the diagonal elements of the Hamiltonian. (The complex potential $W(x)$ was evaluated at the corresponding atomic positions.) The results are shown in Fig. IV.7. In this case, the agreement is

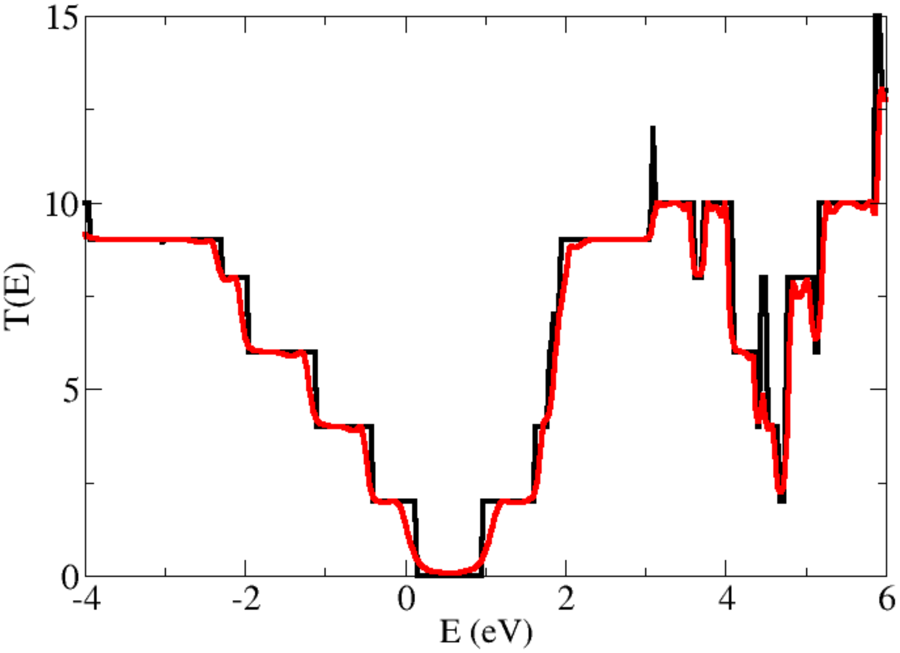

Figure IV.7: Transmission probability of a (5,5) carbon nanotube using the Hückel Hamiltonian.

not perfect, but considering the approximate nature of the construction of the matrix elements the closeness of the results is remarkable.

This section has presented an efficient and accurate way to calculate self-energy matrices for Green's function calculations. By adding a complex absorbing potential to the Hamiltonian of the semi-infinite lead, the lead can be terminated in a finite distance leading to finite dimensional matrices. In this way the leads' Green's functions can be calculated from their spectral representation for any energy at the same time. The examples presented in this section show the accuracy and effectiveness of the approach. For a given lead and basis set the lead's Green's functions can be precalculated and tabulated eliminating the computational bottleneck related to self-energy evaluations in transport calculations.

In typical transport calculations the dimension of the matrices used to describe a single block of the lead is on the order of a few hundreds. In our approach 4-6 of those blocks are used so the typical dimension of the matrices to be diagonalized is a few thousands. Complex symmetric matrices of that size can be easily diagonalized with standard direct diagonalization approaches. The Hamiltonian and overlap matrices in Equation 4.31 are block tridiagonal, and by using this special sparse structure the diagonalization can be made much faster. Iterative diagonalization can also be useful but so far we have used the whole eigenspectrum to construct the Green's functions, and so the advantage of iterative approaches when more than a few eigensolutions is needed is not tested. In the future we will investigate the possibility of using only a few dominant eigensolutions in the spectral representation of the leads' Green's function. If a few dominant eigensolutions provide satisfactory accuracy, an iterative solution for those target eigensolutions will make the approach even more powerful.

4.3 Summary

This chapter has given an introduction to the theory, implementation, and applications of complex absorbing potentials (CAPs). The various examples presented provide rigorous tests that allow us to rely on the CAPs' use in field emission calculations, where no such rigorous tests exist.

CHAPTER V

NANOSTRUCTURES AND FIELD EMISSION

The term "nanostructure" is typically used to describe an object that has at least one dimension that is most conveniently measured in nanometers (nm). Nanostructures can be classified based on how many of their dimensions are at the nanometer scale. For example, a nanotube is usually nanoscale in all dimensions except for the axial dimension. We can then say that this is a "one dimensional" structure, since only one dimension is not confined to nanoscale size.

The calculations performed for this dissertation involve nanowires, graphene nanoribbons, and nanotubes. Most of these structures are made from carbon, but some of the nanotubes are composed of other materials such as BN or SiC. This chapter presents the results of calculations of field emission from various nanostructures. These results go beyond existing work to give first-principles insight into the physics of field emission from these devices. First, an overview of field emission theory is presented. This is followed by several sections discussing the structure and field emission behavior of several nanostructures.

5.1 Field emission

5.1.1 Types of electron emission

Electrons are confined to a structure by a potential, which is itself due to the attraction of the positively charged atomic nuclei. In order to escape this potential and be emitted, an electron must somehow get beyond this potential. If an electron absorbs energy from a photon, for example, its energy may increase enough to break free of the potential. We can define the work function as the minimum energy that, when absorbed by an electron, will allow the electron to escape the potential. Here "escape" means just barely outside; excess energy will be used as kinetic energy, moving the electron away. In the case of photon absorption, this is called the photoelectric effect, and was first explained by Einstein in 1905 [144]. If the added energy instead comes from heating the material, we then say that the electrons have been emitted via thermionic emission [145]. In both of these cases, the electron escapes by gaining an energy that exceeds the confining potential.

Another way to get out of the potential is to modify it by applying an external electric field. This reshapes the potential into a barrier that can be overcome via quantum tunneling. Electrons that escape in this way are said to be field emitted [30]. In Figure V.1 a 1D confining potential is shown for different applied electric field strengths. Notice that with no field applied, tunnelling is not possible.

5.1.2 Theoretical models

5.1.2.1 Fowler-Nordheim theory

The earliest theory for field electron emission was developed in the late 1920s by Fowler and Nordheim (FN) [30]. This theory describes the emission of electrons from a flat metal surface in the presence of an electric field. The FN equation gives the current density J of field emitted electrons, and its derivation can be found in Ref.

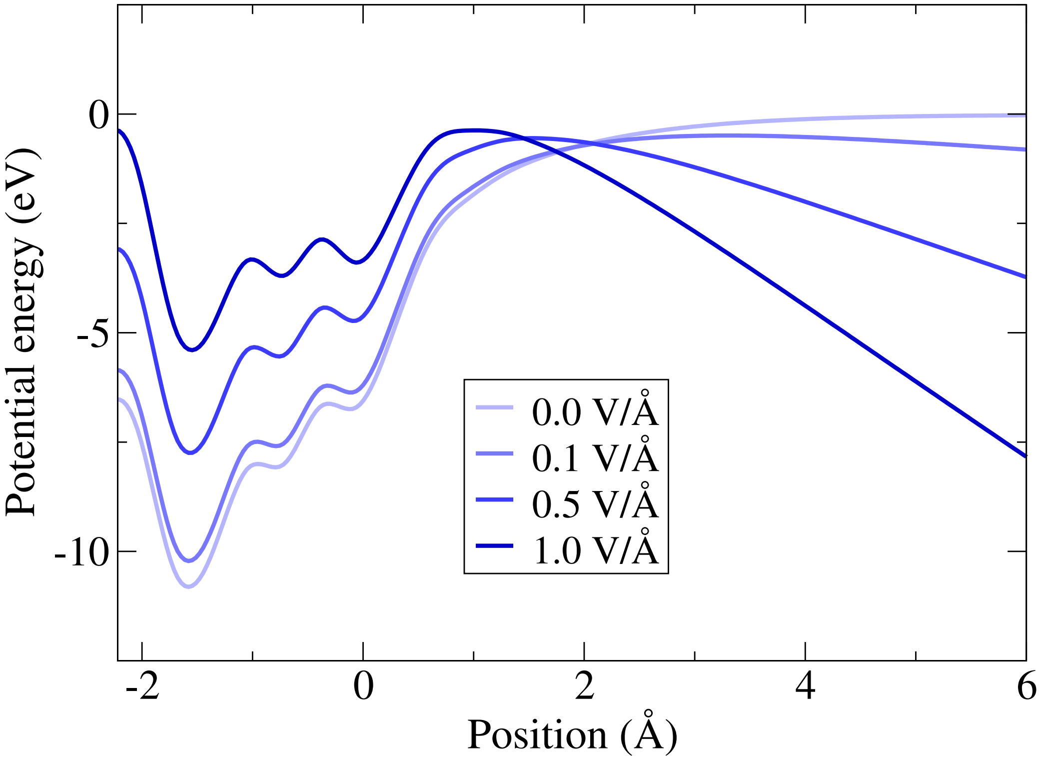

Figure V.1: One-dimensional confining potential under different electric field strengths.

[146]. That derivation is briefly summarized below.

In order to contribute to the emitted current density, electrons must tunnel from the metallic bulk into vacuum. By summing the contributions from all such electrons, we get [146]

$$J = 2e \int_{\mathbf{k}} f_{FD}(E, E_F, T) D(E) v_x \frac{d^3\mathbf{k}}{(2\pi)^3} \tag{5.1}$$

where J is the emitted current density, e is the electron charge, $D(E)$ is the tunnelling probability for an electron with energy E, and the integration is over all wave vectors $\mathbf{k}$. $v_x = \hbar k_x/m$ is the electron velocity perpendicular to the surface. The factor of 2 accounts for spin. f_{FD} is the Fermi-Dirac distribution for the occupation of energy level E at temperature T with Fermi energy E_F:

$$f_{FD}(E, E_F, T) = \left[exp\left(\frac{E - E_F}{k_B T}\right) + 1 \right]^{-1} \tag{5.2}$$

Now we need to find an expression for $D(E)$. The original FN approach used a simple 1D barrier tunneling formalism in which wavefunctions are matched on each side of the barrier.

The original FN equation was later refined to include the Schottky effect [147], which was described in Section 1.1. This change means that the simple wavefunction matching approach to solving the tunneling problem no longer is applicable, but one can instead use the WKB approximation [146]. The modern form of the FN equation, from Bonard et al [148] is

$$J = \frac{1.5 \times 10^{-6}}{\phi} E^2 exp\left(\frac{10.4}{\sqrt{\phi}} - \frac{6.44 \times 10^9 \phi^{\frac{3}{2}}}{E}\right) \tag{5.3}$$

where ϕ is the work function of the metal and E is the local electric field at the metal's surface. The units of J in the above equation are A/m^2, ϕ is given in eV, and E is given in V/m.

Applied to nanotubes, some aspects of the experimental data can be modeled by FN theory [31]. In the case of high current densities, the theory fails to describe the phenomena [32]. Also, the experimental energy spectra in the low energy region differs from the predictions of FN theory. The physical reasons for these deviations are still debated, and several possible explanations have been suggested. These include non-metallic density of states near the emission site of the nanotube [149], space charge effects [150], and interactions between nanotubes [151], in those cases using clusters of tubes. Our calculations only use single, isolated nanotubes. In addition, we make no assumptions about densities of states. This means that our calculations can incorporate these effects. Our method also handles space charge effects, as we now discuss.

With the space charge [152, 151] effect, a high current density results in a significant amount of charge being present near the end of the nanotube. This charge produces its own electric field, which can partially screen the externally applied electric field. This results in a lower effective field at the field emission site, and so the current reaches a saturation level. Adsorbates can further complicate the space charge effect, as charge can accumulate in the region between the nanotube and adsorbate [153], as well as in the region beyond the adsorbate.

It is important to note that the calculations presented in this dissertation incorportate the effects of space charge. This is because for each time step we calculate the electron density, and solve the Poisson equation to get the resulting potential. As a result, any space charge effects will be included, and no *ad hoc* modeling is required.

5.1.2.2 Beyond Fowler-Nordheim

Since FN theory was developed, several more advanced approaches have emerged. Field emission is fundamentally a problem in scattering theory, which includes tunneling as a special case. So, various theoretical frameworks in scattering theory have been applied. Examples include static calculations such as the transfer matrix method

[154] and the scattering state approach [155], as well as some time-dependent calculations [156]. These approaches still make assumptions about the physical system, though fewer assumptions than in FN theory. The method used here, time-dependent density functional theory [7], is a first-principles approach as was discussed in Chapter II.

5.1.3 Geometric field enhancement

Electron field emission requires the application of an external electric field E_{app}. A common experimental approach to generating this field is via a parallel plate capacitor configuration. In this case the capacitor plates are held at a voltage difference V. The plates are parallel and separated by a distance d. From V and d simple electrostatics [157] gives

$$E_{app} = V/d. \tag{5.4}$$

A crucial point is that the externally applied field E_{app} may in fact differ from the local field present at the surface of the nanostructure. We will call this local field E, and it is related to E_{app} by

$$E = \beta E_{app} \tag{5.5}$$

where β is called the field enhancement factor. β is determined mainly by the geometry of the nanostructure [158]. Several simple, analytically-solvable models that explain this geometric effect are reviewed by Forbes [159]. Here we give a simple qualitative explanation of how this effect works.

Consider an uncharged solid conducting medium. If there is no applied external electric field, the valence electrons are distributed throughout the medium relative to the nuclei so that there is no net electric field. If we apply an electric field, the valence electrons are free to move (but not the nuclei, which are held relatively fixed in the solid's lattice). This induced separation of charge creates an electric field inside the medium that opposes the applied field. The charge separation continues until the fields cancel, leaving no more field to move the electrons. In this equilibrium state, there is no electric field inside the medium. Since the electric field is the negative gradient of the electric potential, this also means that (in equilibrium) the electric potential inside the medium is constant.

The redistribution of the electrons also causes an induced surface charge density on the surface of the medium. The electrons along the surface repel each other due to the Coulomb force. For electrons along a flat part of the surface, this repulsive force is directed parallel to the surface. For electrons along a curved part of the surface, however, some part of the vector repulsive force is directed perpendicular to the surface and so does not contribute to the electron separation. As a result, the electrons along the curved surface can move closer together, since they feel this effectively reduced repulsive force. The extra charge in the curved surface produces a stronger electric field near it.

By combining Equations 5.3, 5.4, and 5.5, the FN equation is modified to contain β:

$$J = \frac{1.5 \times 10^{-6}}{\phi} \left(\frac{\beta V}{d}\right)^2 exp\left(\frac{10.4}{\sqrt{\phi}} - \frac{6.44 \times 10^9 \phi^{\frac{3}{2}} d}{\beta V}\right) \tag{5.6}$$

β can then be experimentally determined by fitting the FN equation to the current-voltage data via a Fowler-Nordheim plot, which was introduced in 1929 by Stern et al [160]. As can be see from Equation 5.6, if one plots $ln(J/V^2)$ versus V^{-1}, the slope should be a straight line, with

$$slope = \frac{6.44 \times 10^9 \phi^{\frac{3}{2}} d}{\beta} \tag{5.7}$$

From this slope, and knowledge of the work function ϕ (via experiment), one can determine the field enhancement factor β.

These β values can then be used as constants in theoretical models. Note that this assumes that β is spatially and temporally invariant, which is not the case. In addition to geometry, the field enhancement factor can also be affected by the presence of nearby structures [161, 162], variations in the internal structure of substrates [158], and variations in the cathode-anode distance [163]. Because of this, there has been effort [164, 165] to develop more complex field enhancement factors. For example, Bonard et al [148] considers the case of a cylinder capped by a hemisphere, which is a model for a capped nanotube. Their expression for β is

$$\beta = 1.2 \times \left(2.5 + \frac{L}{r}\right)^{0.9} \left[1 + 0.013 \times \left(\frac{d}{d-L}\right) - 0.033 \times \left(\frac{d-L}{d}\right)\right] \tag{5.8}$$

where d is the distance between the nanotube and the anode, r is the cylinder radius, and L is the length of the nanotube, including the cap.

One major advantage of our first-principles approach is that we do not have to use the field enhancement concept at all; any rearragement of electronic charge due to geometry is automatically included, since we are time-propagating the electron density itself. It is only when models such as FN are used, which do not work with the electronic density directly, that one needs to include a model parameter such as the field enhancement factor.

5.1.4 Resonant tunneling and adsorbates

Although many field emission experiments are conducted in very high vacuum conditions, some residual gas remains [166]. It has been observed experimentally [4, 22, 23, 24, 20, 26, 27] that these atoms can bond to the cap of a carbon nanotube, and can in fact dramatically alter the field emission current, as shown in Ref. [167] and Figure V.2. A more detailed image (from a different experiment) is shown in Figure V.3. The adsorbates usually do not stay bound for long, since the current heats the system and gives the adsorbate energy. Once the adsorbate is gone, the current returns to normal levels. This discovery prompted the search [168, 36] for adsorbates that can stay bound for reasonably long times and still increase the current significantly.

Resonant tunneling provides a potential physical explanation for how adsorbates can increase current [4]. Here the presence of an adsorbate adds localized electronic states to the end of the nanotube, which alters the potential barrier from its typical triangular shape by adding a well. The result is a double-barrier tunneling configuration. There are then two tunneling problems: (1) from the nanotube to the adsorbate, and (2) from the adsorbate to the vacuum. The overall transmission probability from nanotube to vacuum is therefore a function the transmission probabilities for each

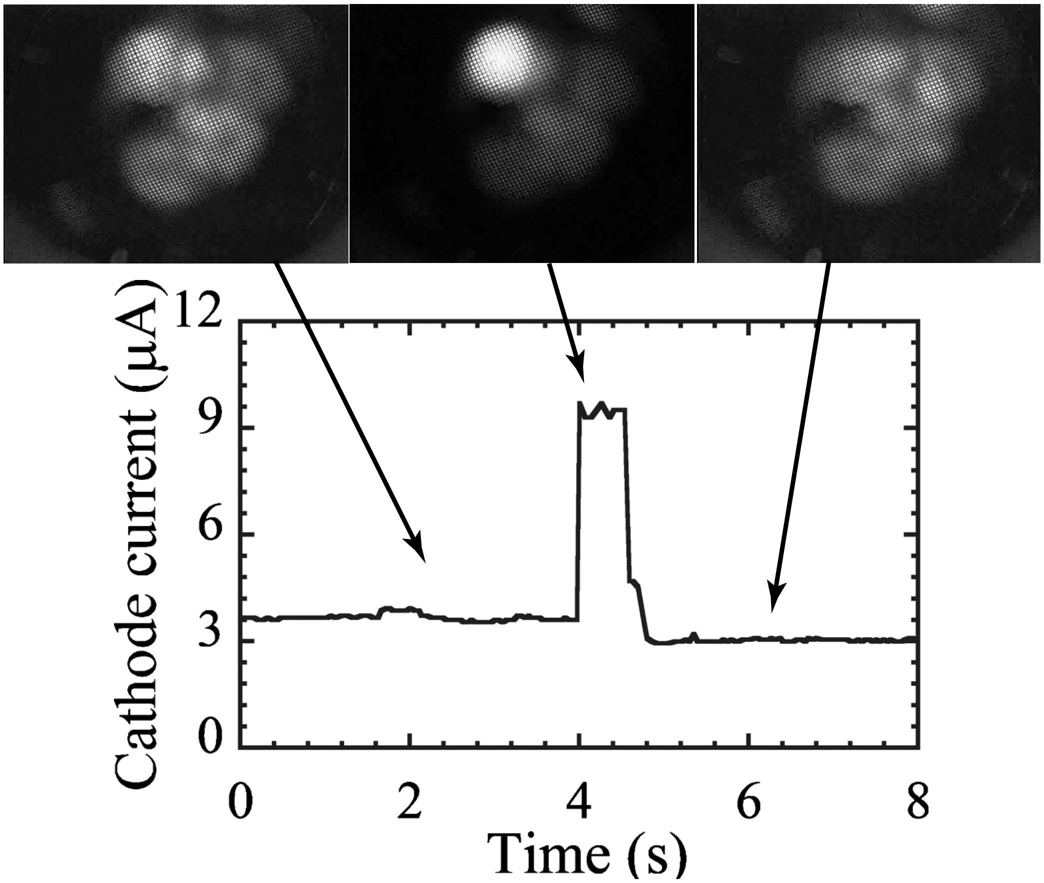

Figure V.2: Field emission current vs. time for a multiwall nanotube, with and without adsorbates. The presence of adsorbates causes the current to increase, and a corresponding bright spot on a phosphor screen is visible. From [4].

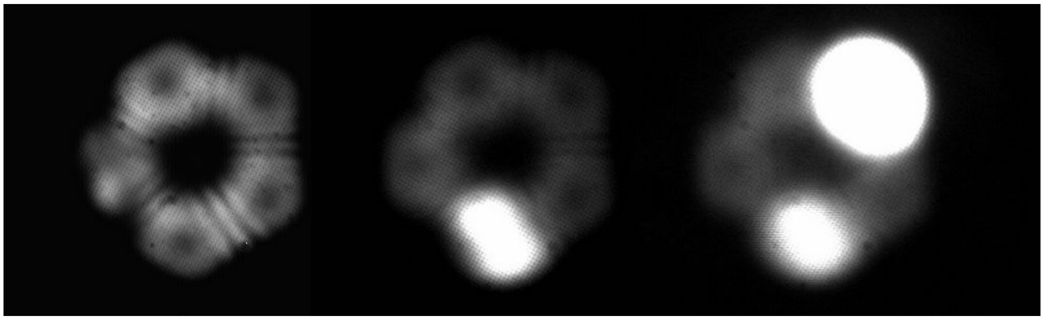

Figure V.3: A multiwall nanotube with and without adsorbates. The presence of adsorbates causes the current to increase, and a corresponding bright spot on a phosphor screen is visible. From [5].

barrier alone [153]. Without resonant tunneling, the electrons with highest energies (i.e., at the Fermi level E_F) are the most likely to tunnel out into vacuum. The idea behind resonant tunneling is that for certain electron energies, the overall tunneling probability will be increased dramatically. In fact, for certain (resonant) energies, the transmission probability can be much higher than what is possible with a single barrier. This means that more electrons can now get out, thus increasing the total current. A signature of this phenomenon can be found by analyzing the energy spectrum of the emitted electrons [4]. Without resonant tunneling, most of the current will be peaked around E_F. In a resonant tunneling situation, there will be peaks at other (resonant) energies.

5.2 Nanotubes

Graphene is a two-dimensional sheet of carbon atoms arranged in a hexagonal lattice whose real space lattice vectors can be given as (see Figure V.4)

$$\mathbf{a}_1 = \left(\frac{\sqrt{3}}{2}a, \frac{a}{2}\right), \qquad \mathbf{a}_2 = \left(\frac{\sqrt{3}}{2}a, -\frac{a}{2}\right), \tag{5.9}$$

where $a = \sqrt{3}a_{C-C}$ is the lattice constant of the graphene and $a_{C-C} = 1.41$ Å is the carbon-carbon bond length. Graphene will be described in more detail below. For now, we turn to carbon nanotubes. In a single-walled carbon nanotube, graphene is rolled into a tube [169]. The sheet can be connected to itself in several ways by shifting one side before the connection is made. This determines the chirality of the nanotube, which specifies the spatial arrangement of carbon atoms in the tube (see Figure V.5).

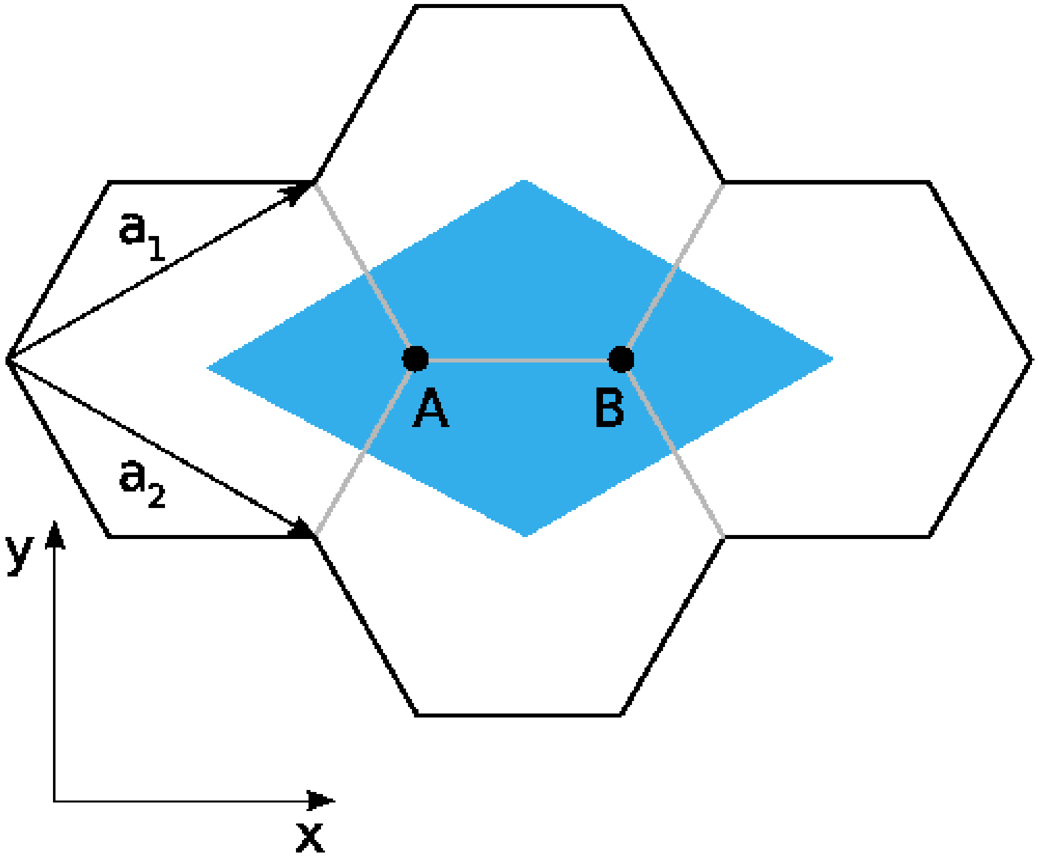

Figure V.4: Real space lattice vectors of graphene. The shaded area marks the unit cell.

Unlike graphite, which consists of many graphene sheets that can conduct in many directions, the nanotube's longitudinal axis defines a preferred direction for transport, and the nanotube's chirality determines whether the tube, in this direction, behaves as a semiconductor or a conductor [170].

The chirality of a nanotube is specified by (n, m), where n and m are integers called chiral indices. When $m = n$, the nanotube is said to have an armchair structure. Another class is the zigzag nanotube, in which $m = 0$. All other cases are called chiral

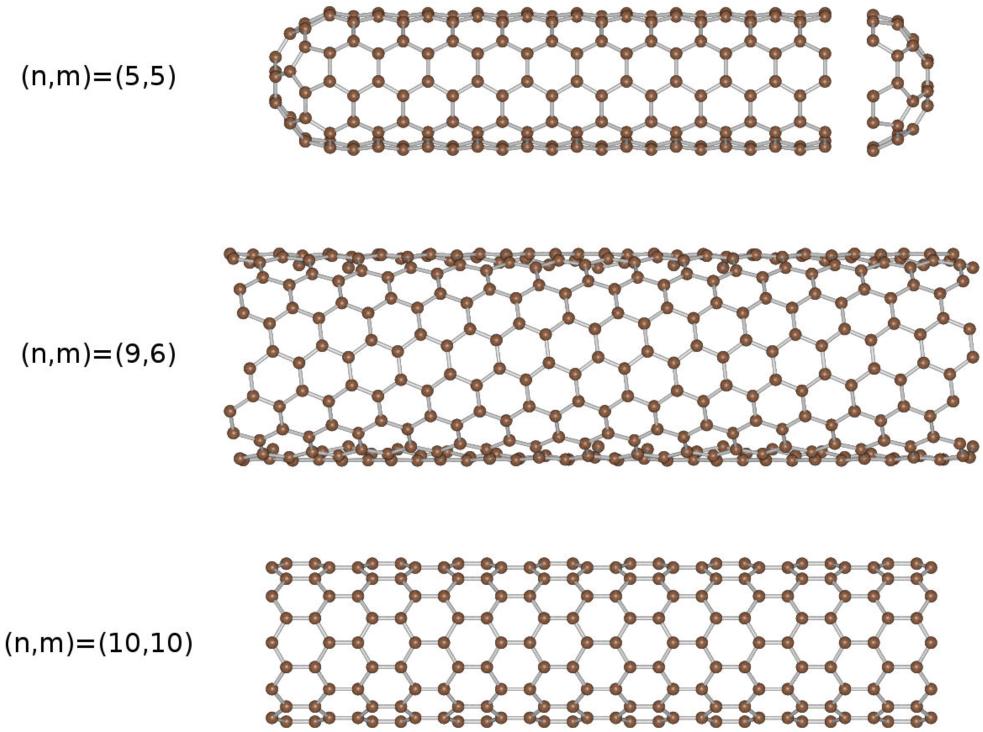

Figure V.5: Examples of nanotubes with varying chirality.

nanotubes.

Figure V.6 allows us to make rigorous the analogy of a nanotube as a rolled-up sheet of graphene. In the figure, $\mathbf{T}$ is the long axis of the nanotube. The sheet will be rolled up such that points B and B' meet, and the same for points O and A. The region enclosed by the points O, A, B, and B' define the nanotube's unit cell. The vector $\mathbf{C}_h$ is the chiral vector, defined to be

$$\mathbf{C}_h = n\mathbf{a}_1 + m\mathbf{a}_2 \tag{5.10}$$

where n and m are the usual chiral indices, and $\mathbf{a_1}$ and $\mathbf{a_2}$ are the same graphene unit vectors as in Equation 5.9. The chiral angle Θ is a useful quantity for characterizing

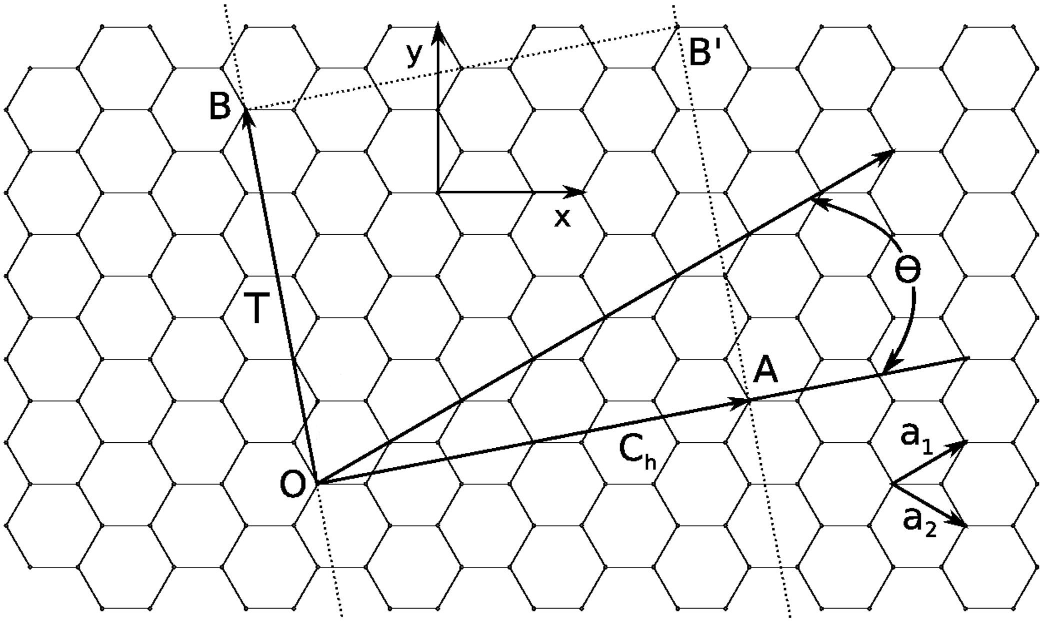

Figure V.6: Hexagonal structure of graphene before being rolled up into a nanotube.

nanotubes. It is defined as the angle between $\mathbf{C_h}$ and $\mathbf{a_1}$, and can be expressed as

$$\Theta = \frac{2n+m}{2\sqrt{n^2+m^2+nm}} \tag{5.11}$$

This angle expresses how the hexagons in the graphene sheet are oriented relative to the nanotube axis **T**. For example, armchair nanotubes have $\Theta = 30°$ while zigzag nanotubes have $\Theta = 0°$. Finally, the diameter d of a single-walled nanotube is completely determined by its chiral indices:

$$d = a\sqrt{n^2+m^2+nm} \tag{5.12}$$

Experimentally, one usually works with multiwalled nanotubes (MWNTs), because they are easier to fabricate than single-wall nanotubes [171]. MWNTs can be thought of as a collection of single-walled nanotubes that have a coaxial, nested structure. In addition to variations in the number of walls, the end of a nanotube can be open or closed. In calculations, the closed ends are usually modeled by half fullerenes (e.g., half of a C60 molecule in the case of a (5,5) nanotube, as shown in the top of Figure V.5). The nanotubes are usually closed after creation but can become open via processes such as mechanical breakage or laser vaporization of the tip [172].

The high aspect ratio and atomically sharp apex make nanotubes (NTs) attractive for applications as field emitters. In addition to these geometrical features, carbon nanotubes (CNTs) have high mechanical strength [173, 174], electrical [175] and thermal [176, 177] conductivity, and high thermal [178] stability which allows the fabrication of novel CNT-based devices such as next-generation displays [17, 19, 179, 180, 181, 182], electron sources [8, 16, 18], and high-resolution electron beam instruments [20, 15, 21]. In addition to carbon, nanotubes of other types have also been synthesized which share some of the same desirable properties of CNTs. Examples include BN [183], SiC [184], Si [185], and GaN [186] nanotubes.

5.2.1 Adsorbate effects in nanotube field emission

The influence of adsorbed atoms on field emission is investigated in this section. It is found that adsorbate atoms significantly increase the field emission current and cause strong differences and nonlinearity in the Fowler-Nordheim plot. The adsorbates introduce additional electron orbitals which are localized around the tip of the nanotube and electrons are easily emitted from these states.

5.2.1.1 Positions of the adsorbates

The calculations use a 20 Å long capped $(5, 5)$ carbon nanotube as a model system. To determine the position of the adsorbate, the adsorbate atom was positioned in front of the nanotube (see Figure V.7) and the system was relaxed by first-principles geometry optimization using the code VASP [187]. In these calculations the atomic positions of the adsorbate atom and the carbon atoms forming the cap of the CN were allowed to relax while the rest of the system was kept fixed. Convergence was achieved when the forces on atoms were less than 0.05 eV/Å . The obtained bond distances (see Table V.1) are in good agreement with previous calculations [188]. This static geometry optimization approach is a compromise dictated by computational limitations. In a more elaborate calculation one would do a first-principles molecular dynamics simulation in the presence of the electric field. But then, for a consistent description, one should account for the field emission of electrons during the molecular dynamics (picosecond time range) which is computationally unfeasible. One expects

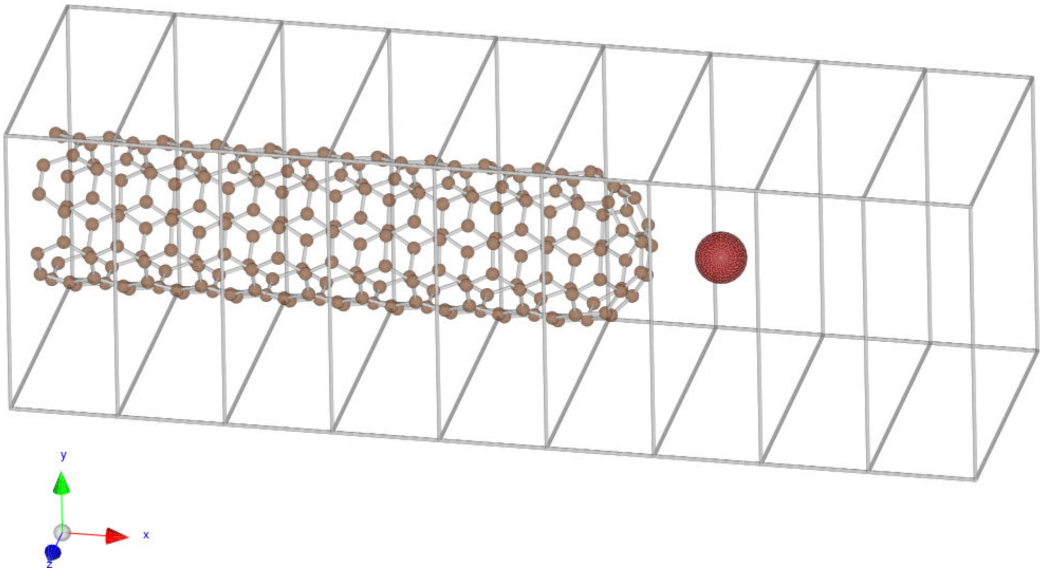

Figure V.7: A capped (5,5) carbon nanotube with an adsorbate atom.

that in the presence of an electric field, the equilibrium position would be slightly different. We have shifted the adsorbates ±0.1 Å from the equilibrium position to test the effect of the position change on the current. The current has changed by less then 10 % due to the shift in position. While this shows the expected sensitivity of the field emission current on the position of the adsorbate, the calculations show that the relative currents of various adsorbates remain similar. In addition, the short time scales of these calculations means that the atoms do not have time to move significantly due to the applied electric field, which further justifies our methods. Figure V.8 shows an enlargement of the nanotube cap region with a tungsten adsorbate.

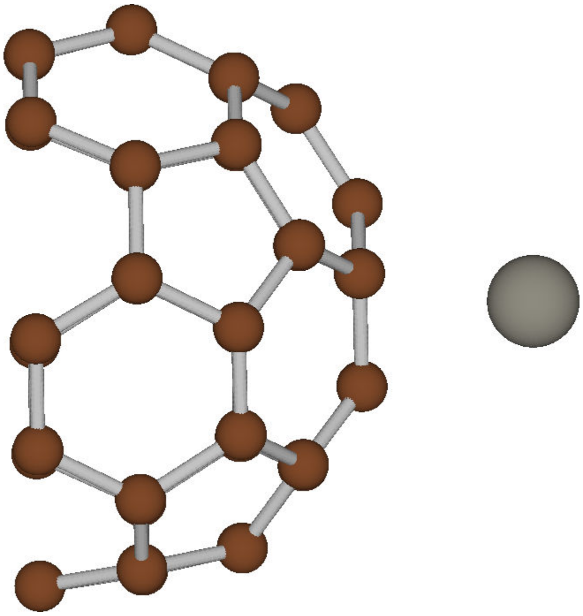

Figure V.8: Enlargement of the cap region of a carbon nanotube with a tungsten adsorbate.

5.2.1.2 Methods

Once the ground state of the system is calculated, the electric field is added and time development for 2 fs begins. The electric field is directed along the axis of the

Table V.1: Field emission current for (5,5) capped nanotubes with various adsorbate atoms in a 1 V/Å electric field.

Adsorbate	Current (μA)	Bond distance (Å)
None	28.4	-
F	75.5	1.38
Cs	117.4	2.28
S	176.0	1.83
Al	189.3	2.21
Au	190.9	2.28
Ag	200.3	2.43
Si	216.6	2.02
W	276.4	2.12

nanotube. The electric field's magnitude is increased slowly with a linear ramp over 0.2 fs. The ramping is used to slowly turn on the field, so that an abrupt jump is not introduced. Such jumps lead to transient effects in the results which take time to dissipate, and are unphysical since an instantaneous jump is not possible. At time t, the scaled field strength E_s is

$$E_s = E \times min\left(1, \frac{t}{t_{ramp}}\right) \tag{5.13}$$

where E is the full electric field magnitude, t_{ramp} is the duration of the ramping (here 0.2 fs), and the "min" operator selects the minimum of its arguments. This operator is used so that for $t \geq t_{ramp}$, $E_s = E$. The ramping duration of 0.2 fs was determined empirically to be sufficient to avoid transient effects. Once a steady state has been reached, the FE current was measured.

5.2.1.3 Results

The calculated currents for several adsorbates are given in Table V.1. The results show that compared to the untipped case, almost an order of magnitude increase can be achieved by a tungsten adsorbate atom at 1 V/Å, which is a typical electric field used in experiments. Calculations using different electric fields show a similar tendency (see Figure V.9). The calculated current enhancement factor for Cs is about 4 which is smaller than the experimentally observed order of magnitude increase [28], but it is in good agreement with the theoretical prediction of 3.4 in Ref. [189]. The direct comparison to the experiment is difficult, because in the experiments (1) longer, thicker and most probably multiwall CNs are used and (2) several adsorbate atoms can be present in different cap positions. Here, the addition of adsorbate atoms always increased the field emission current. Some experiments show that other types of adsorbates, such as CO, CO_2 and CH_4 molecules, can decrease the field emission current [26, 27]. The role of the adsorbate atom in the enhancement of the field emission current is twofold. The calculations show that (1) the adsorbate atom lowers the potential energy barrier for the emitted electrons and (2) the adsorbate atom introduces extra electronic states at and above the HOMO in the CN spectrum. The energy spread of the emitted current is illustrated in Figure V.10. This spectrum plot was created using Gaussian broadening. For each Kohn-Sham orbital, a Gaussian was added to the plot, where the Gaussian's height was set to be the current from that orbital. The full-width at half-maximum (FWHM) of the Gaussian was set to be 0.2 eV. Once the Gaussians are added, they are summed and the result is the spectrum plot of Figure V.10.

Larger values of the FWHM tend to smooth out the spectrum, hiding small details. Smaller values reduce the overlap of the Gaussians, making the plot more sensitive

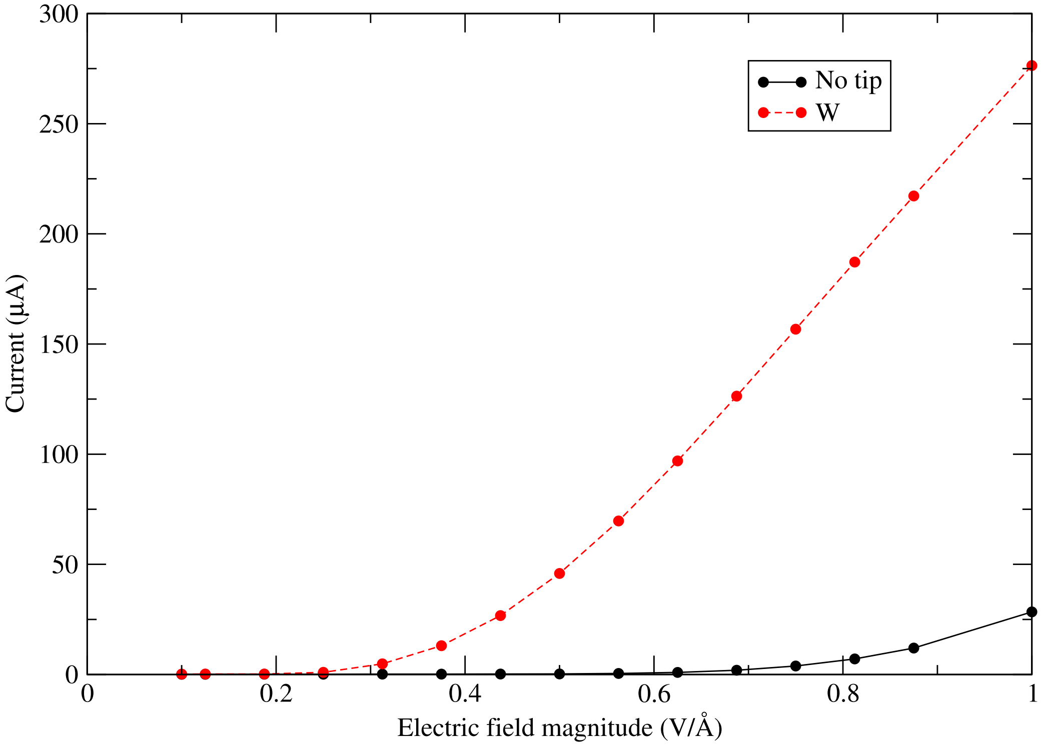

Figure V.9: Current vs. electric field magnitude for no tip and a W tip.

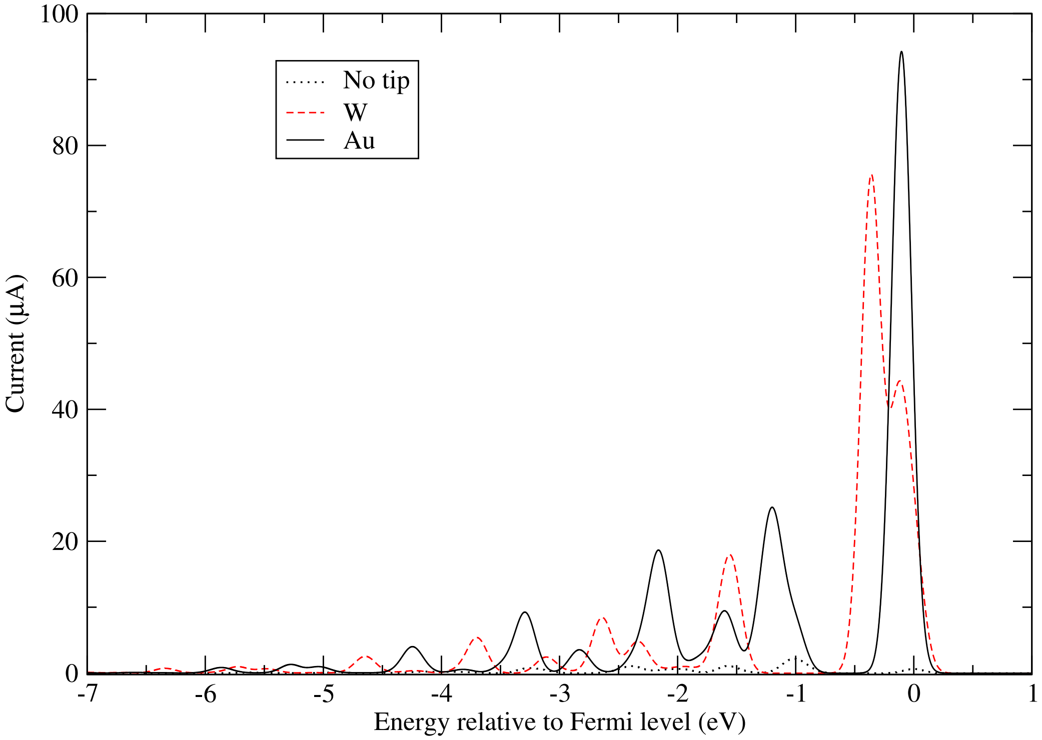

Figure V.10: Current vs. energy, relative to Fermi energy

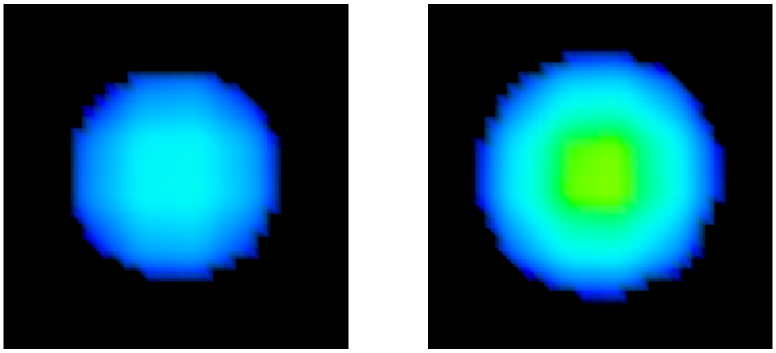
(a) Al (b) Ag

Figure V.11: Two-dimensional spatial pattern of field emission intensity at an electric field magnitude of 1.0 V/Å, for various tips.

to lower current-producing orbitals. We determined the value of 0.2 eV empirically as a good compromise. It allows us to see major peaks, while avoiding the noise of low-current orbitals. Such a value has been used in other calculations (e.g., [190, 191]) and is consistent with experimental resolution [192].

This energy spectrum shows that the majority of the field emission current comes from states located near the Fermi energy. These states are introduced by the adsorbate atom and localized at the tip of the capped CN. When the electric field is turned on these are the states that are propagated into the vacuum carrying the emitted current. These adsorbate-induced states, which do not exist in the case of the untipped CN, are the major contributors to the enhanced current. Spatial snapshots of the emitted current are shown in Figure V.11.

In Figure V.10 it is difficult to see the curve for the no-tip case, so this curve alone is shown in Figure V.12. Note that the spectrum has multiple peaks, which differs from the single peak predicted for Fowler-Nordheim theory and seen experimentally for some nanotube samples (cf. Section 1.1). This multiple-peak structure has been

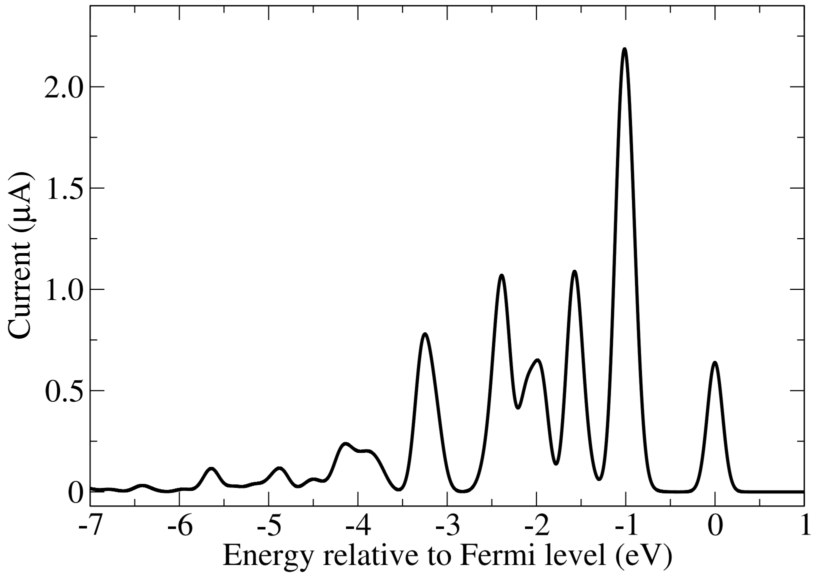

Figure V.12: Current vs. energy, relative to Fermi energy, for the no-tip case.

found in other studies [193, 194] and is likely due to the fact that we use a relatively small, single-walled (5,5) nanotube. In experiments that show single peaks, either multi-wall tubes or bundles of single-wall tubes were used. It is suspected that when using a small-diameter tube (such as the one considered here), the local variation in the surface structure at the emitting end of the tube can cause significant peaks in the local density of states at the tube end, leading to the peaked energy spectra [193, 194]. In larger tubes, the end structure is more averaged out.

Some experiments on CN field emitters show linear [195, 196] Fowler-Nordheim plots (at least in certain field regions) while others are nonlinear [197, 198]. Figure V.13 shows the calculated Fowler-Nordheim plot for the untipped and W adsorbed CN. Both the untipped and the W absorbed CN Fowler-Nordheim plot are nonlinear and the there is a large difference between the behavior of the two systems. The difference in behavior of W tipped and untipped CN clearly indicates the role of local fields and atomistic details in determining the field emission properties of CNs.

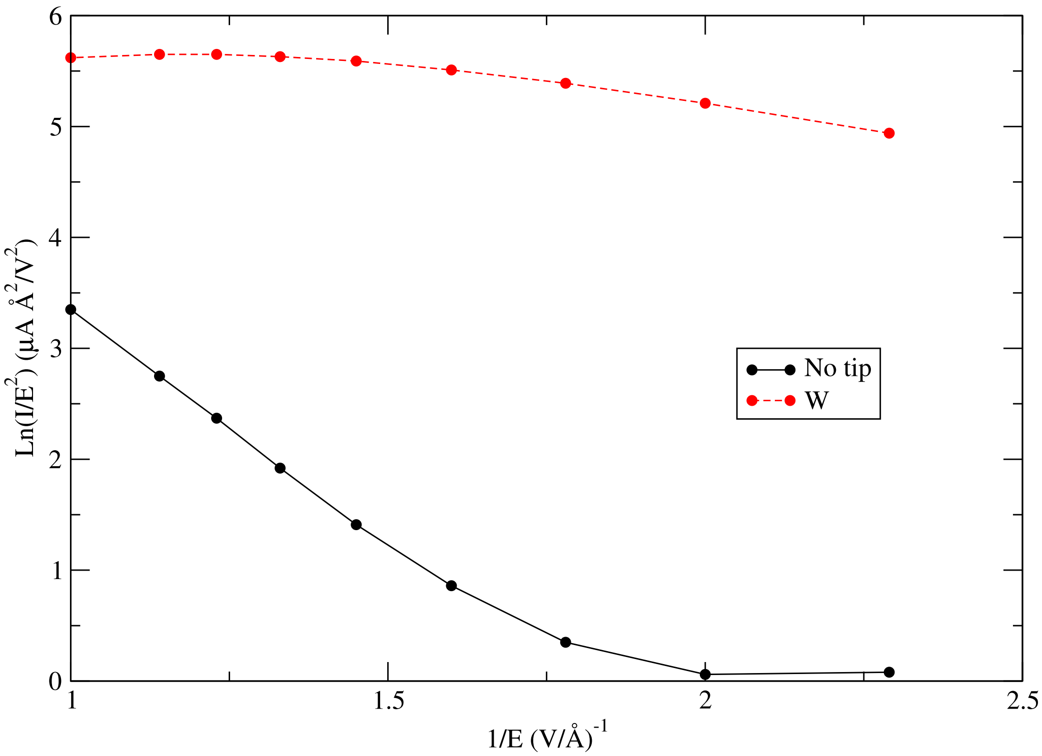

Figure V.13: Fowler-Nordheim plot for no tip and a W tip.

Direct qualitative comparison to experiment is difficult, because of the short length of the CN used in the calculation and the missing information on the chirality of the nanotubes used in the experiments.

5.2.1.4 Summary

In summary, the effect of adsorbates on the field emission properties of carbon nanotubes are investigated. Microscopic description of electron field emission from nanotubes is presented. These studies are important for both understanding the fundamental physics of field emission from CNs and future field emission device applications. It is found that adsorbate atoms significantly increase the field emission current. Adsorbate atoms also cause strong differences and nonlinearity in the Fowler-

Nordheim plot. The source of the enhanced current is electronic states introduced by the adsorbate atom.

In the future, we would like to consider adsorbates at sites other than the end pentagon, in order to compare with the present results. Further, only single-atom adsorbates were considered here; many other possibilities exist. Future work may include the study of adsorbed molecules, and in these cases the molecular orientation will become another variable to be studied.

5.2.2 Laser-enhanced field emission

The rapid development of experimental techniques, especially the advances of high-power femtosecond lasers, allows the investigation of dynamical processes in nanostructures on the subfemtosecond time scale [199, 200, 201, 202]. To gain physical insight into the interaction between lasers and nanostructures, the understanding of nanoscale electron dynamics in time varying fields is indispensable. One of the most intriguing effects of strong electric fields is the induced field emission due to electrons tunneling into the vacuum. Laser-induced field emission in metallic needle cathodes with nanometer-scale sharpness has been realized in experiments and is used to generate bright, low-emittance, and short electron bunches with durations down to the femtosecond range, ideal for applications such as time-resolved electron microscopy, compact free-electron lasers [203], or scanning probe microscopy [204].

The physical mechanism of laser-induced field emission is not clearly understood. In a simple model the electrons are confined by a potential and the field emission is described by tunneling of the electrons through the potential barrier. The laser field can excite electrons by single or multiphoton absorption leading to enhanced tunneling through the potential barrier (photo-field emission). At the same time, the laser field also modifies the potential barrier prompting direct field emission (optical field emission). Simple one dimensional potential model calculations [199] nicely illustrate the effect of laser pulses on the potential barrier, but to test the relative importance of the various field emission mechanisms and to understand the highly nonlinear and nonequilibrium laser-induced electron pulses first-principles calculations are necessary.

The TDDFT framework is known [205] to be able to calculate ionization properties for a wide range of laser intensities, from the multiphoton [206] and tunneling [207] regimes to above-threshold ionization [208]. This versatility comes from the fact that the Kohn-Sham framework provides the exact electron density, from which all properties of the system can be found (cf. Chapter II).

In this section we study laser induced field emission using time-dependent density functional calculations. We will show that the field emission current increases considerably when a laser field is applied. We will also demonstrate that short laser pulses can be used to create spatially and temporally localized electron sources.

5.2.2.1 Adding a laser to TDDFT

The TDDFT simulations are carried out in real space and real time. The system, originally in its ground state, is placed in a static electric field along with a time-dependent laser field and the electron dynamics is simulated by time propagating the Kohn-Sham orbitals. The field emission is calculated as a function of time from the time evolved orbitals in the region far from the emitter.

For a static electric field applied along the positive x-axis, the potential is [157]

$$V_{\text{stat}}(x) = -E_{\text{stat}}x. \tag{5.14}$$

We can include a laser pulse field by adding the following time-dependent potential to the system's Hamiltonian:

$$V_{\text{laser}}(\mathbf{r}, t) = V_{\text{laser}}(\mathbf{r}) \exp\left[-\frac{(t - t_{\text{peak}})^2}{a^2}\right] \cos(\omega t)$$

Here ω is the laser frequency and $V_{\text{laser}}(\mathbf{r})$ is the amplitude of the oscillating potential. Parameter a controls the width of the Gaussian envelope. In this work we use short laser pulses consisting of just a few intense oscillations of the electric field. Accordingly, the value of parameter a was 1.7 fs, while the peak of the pulse occurred at $t_{\text{peak}} = 5$ fs.

Since the wavelength of the laser we used (266 nm) exceeds the size of the system by 1-2 orders of magnitude, the electric field may be considered uniform within the simulation box at any given instant. Assuming that the laser is linearly polarized along the x axis, $V_{\text{laser}}(x) = -E_{\text{laser}}x$ (cf. Equation 5.14). Our calculations used $E_{\text{laser}} = 1$ V/Å for all simulations in which the laser was active. The magnitude of the static field was ten times smaller, 0.1 V/Å.

5.2.2.2 Results

As test systems we have used carbon nanotubes and a chain-like molecule, $C_{12}H_{14}$, which is a particular case of an oligomer of the form C_NH_{N+1}–C_4H_4–C_NH_{N+1} (see Figure V.14). Figure V.15 shows the setup of the calculations. The system under study, in this case a $C_{12}H_{14}$ molecule, is placed in a large simulation box. Both electric fields (i.e., static and laser) are applied along the x axis. Due to the chosen direction of the static electric field, the net flow of electrons will be in the $+x$ direction. We calculate the current through a plane located 10 Å to the right of the molecule.

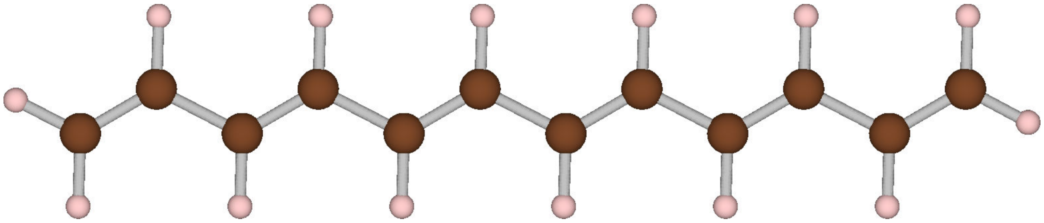

Figure V.14: The $C_{12}H_{14}$ molecule used in the calculations.

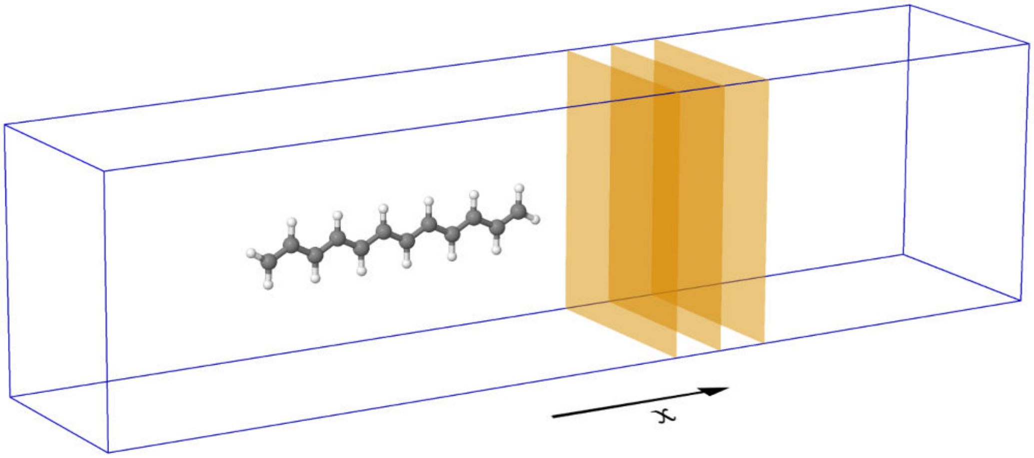

Figure V.15: Simulation box containing a $C_{12}H_{14}$ molecule. The emission current is measured through planes some distance away from the molecule. The space on the right of the measurement planes is the region where the complex absorbing potential acts.

The total simulation times in our calculations were in the range of 20-25 femtoseconds. As mentioned above, the peak of the electric field oscillations was set to occur at the time $t = 5$ fs. After that the laser field oscillations gradually vanished and we observed the response of the system to the strong perturbation they had caused. Since the total simulation time of 20-25 fs is comparable to the vibrational period of a typical C-C or C-H bond [209], it is not immediately clear how significantly the motion of ions during that time could affect the field emission current and whether that could qualitatively change the results. To check the effect of the nuclear motion, test calculations were performed by allowing the ions to move classically under the influence of quantum forces (i.e., Ehrenfest molecular dynamics [210]). The ions were allowed to move only for the smallest system in our simulations, the $C_{12}H_{14}$ molecule. The motion of ions is described by the following system of equations:

$$\begin{aligned} M_i \frac{d^2\mathbf{R}_i}{dt^2} &= -\boldsymbol{\nabla}_{\mathbf{R}_i}\Big[V_{\text{ext}}(\mathbf{R}_i,t) + \sum_{j\neq i}^{N_{\text{ion}}} \frac{Z_i Z_j}{|\mathbf{R}_i - \mathbf{R}_j|} \\ &\quad - \int \frac{Z_i \rho(\mathbf{r},t)}{|\mathbf{R}_i - \mathbf{r}|} d\mathbf{r}\Big], \end{aligned} \tag{5.15}$$

which are coupled with the Kohn-Sham equations through the density. In Equation 5.15 M_i, Z_i, and $\mathbf{R}_i$ are the mass, charge, and the position (respectively) of the i^{th} ion. To compute the positions and velocities of the ions at each time step the Verlet algorithm [211] has been used.

We first present our results for the linear $C_{12}H_{14}$ molecule, which serves as a simple model for a nanowire-like field emitter. At the beginning we optimized the geometry of the system in its ground state in order to avoid an artificial rearrangement of the ionic positions and jump in the ionic temperature during the time evolution.

The calculated field emission currents are shown in Figure V.16. The plot has three curves, corresponding to the simulation with fixed ions, moving ions with zero initial temperature, and moving ions with the initial temperature of 300 K. The calculated maximum currents due to the combined effect of laser pulse and static field, and due to static field only, are compared in Table V.2. The static and laser fields had magnitudes of 0.1 V/Å and 1.0 V/Å, respectively. The temperatures rose by no more

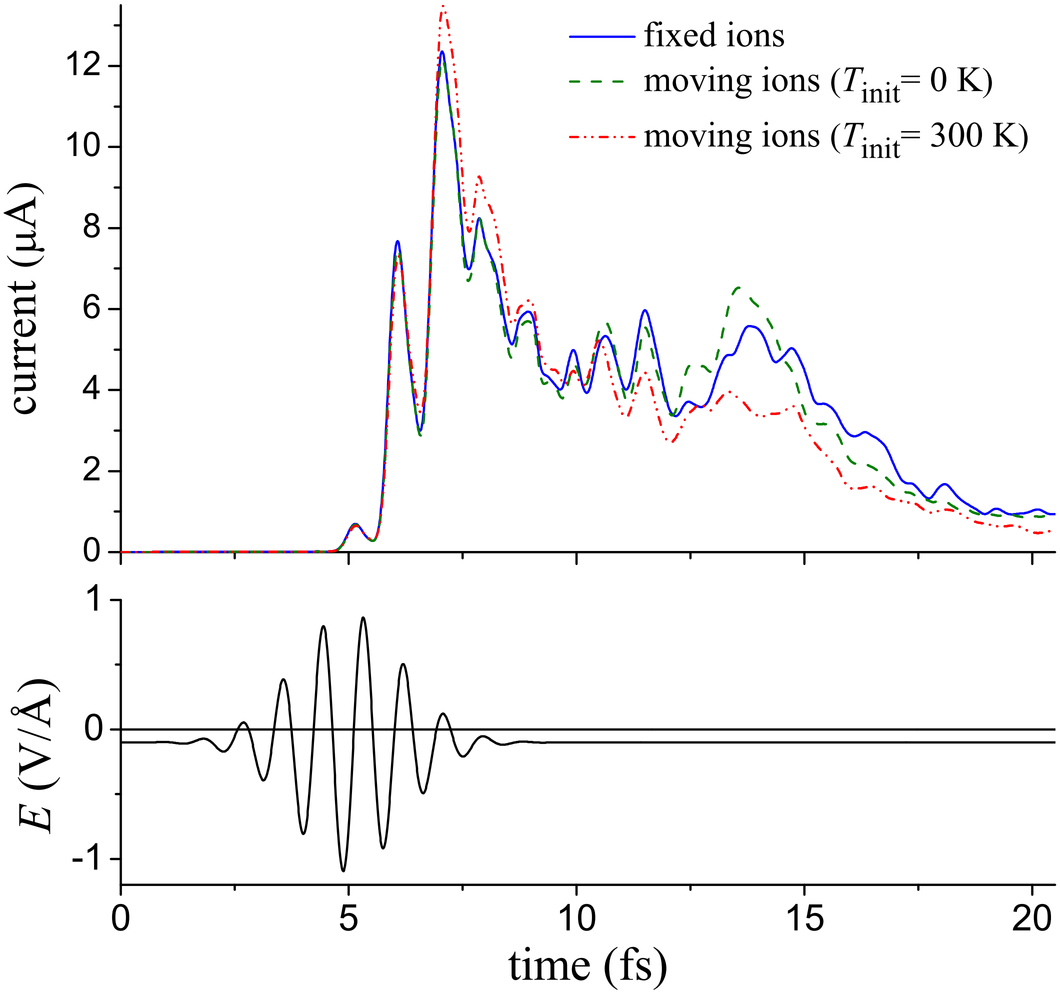

Figure V.16: Field emission from a $C_{12}H_{14}$ molecule due to static electric and laser fields acting together (top) and the laser pulse as a function of time (bottom). The currents shown are computed 10 Å from the right end of the molecule.

than 8 K, and the maximum atomic displacements were under 0.02 Å. From this we conclude that the static and laser fields are not causing significant motions in the atoms.

Table V.2 shows that the addition of a laser pulse to a static (and weak) electric field leads to a significant enhancement of the field emission current. While the laser pulse field has an approximately zero time average, the addition of the static field gives a small net field in the $+x$ direction. The static field alone only produces a tiny fraction of the observed current. The effect of the laser field is therefore to allow field emission to occur at a lower applied static field.

Figure V.16 also demonstrates that the laser pulse induces a field emission current with a pulse-like pattern. As seen in the bottom plot in Figure V.16, the current magnitude starts to increase significantly at around 5 fs, which corresponds to the arrival of the Gaussian envelope peak, and then gradually decays. Notice the relatively long decay tail (significantly longer than the pulse duration). A possible explanation for this behavior is that when the pulse arrives, electrons are excited to higher energies. These higher energies allow the electrons to tunnel out of the nanostructure at a higher rate, leading to a larger observed current. The current only returns to its pre-pulse levels once the excited electrons have tunneled out completely. Since the tunneling out can take longer than the initial transfer of energy from the pulse, a tail is observed on the emitted pulse.

The calculations have been repeated for segments of single walled (3,3) and (5,5) carbon nanotubes. In the case of the (3,3) nanotube (see Figure V.17) we passivated the dangling bonds with hydrogens. For the (5,5) nanotube (see Figure V.18) we placed carbon caps at the ends. The total number of atoms in these two sys-

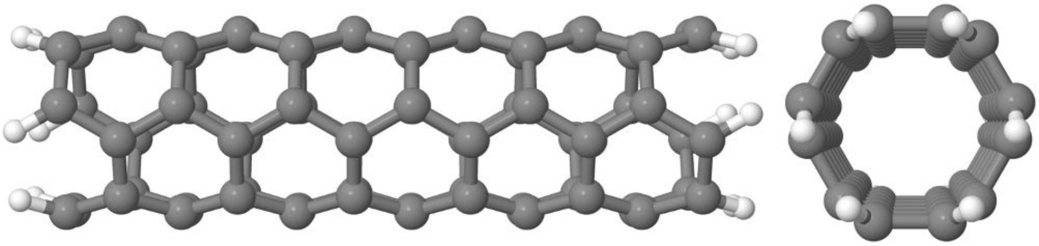

Figure V.17: The (3,3) nanotube used in the calculations.

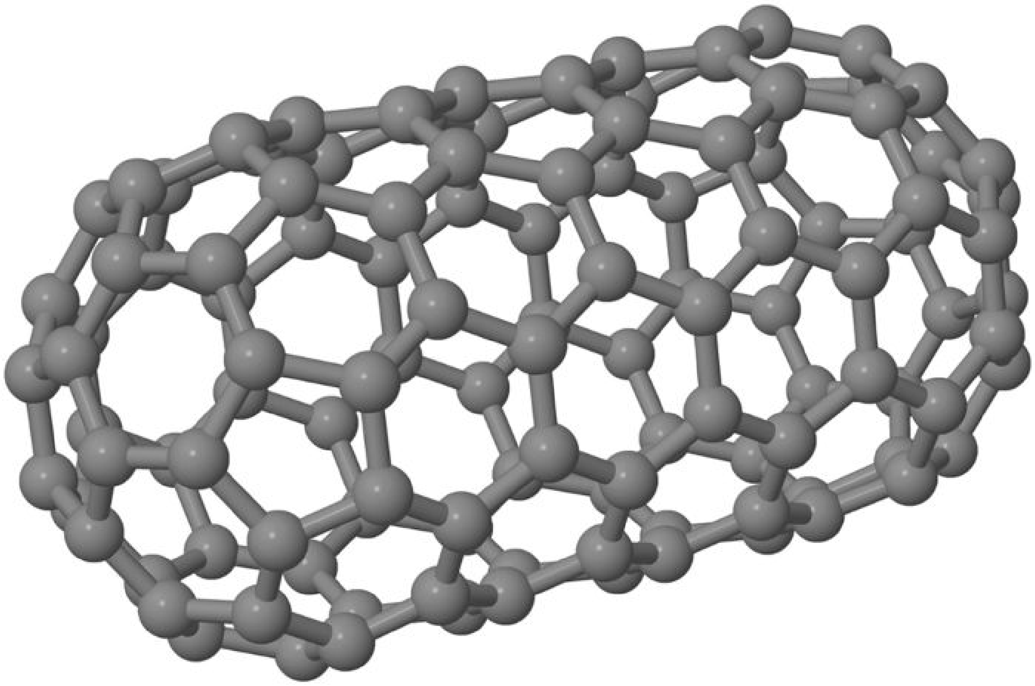

Figure V.18: The (5,5) nanotube used in the calculations.

tems was 84 and 120, respectively. As the difference in field emission current due to ionic motion was not expected to be very significant (as our simulations with $C_{12}H_{14}$ demonstrated), here we only performed the calculations with fixed ions. The field emission currents (see Table V.2) for both nanotubes look very similar qualitatively (apart from an obvious change in the magnitude). In Figure V.21 we show results for the (5,5) nanotube. Similar to the case of $C_{12}H_{14}$, the current is several orders of magnitude higher when the laser is applied.

A time series of plots in Figure V.19 for the (5,5) nanotube shows changes in

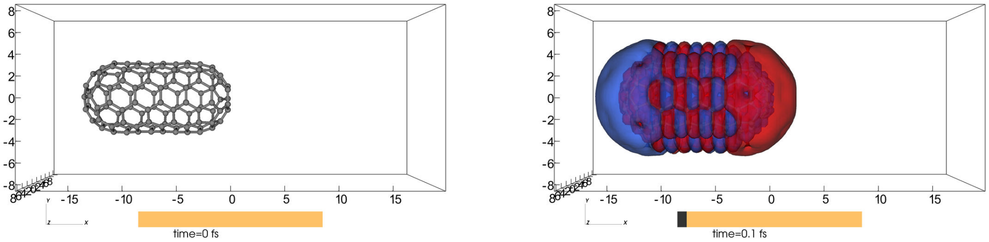

(a) t=0.0 fs

(b) t=0.1 fs

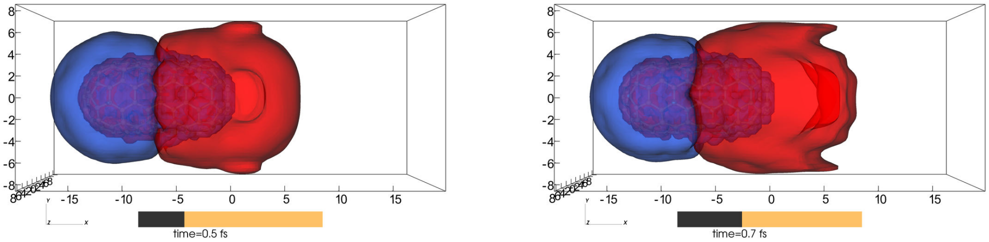

(c) t=0.5 fs

(d) t=0.7 fs

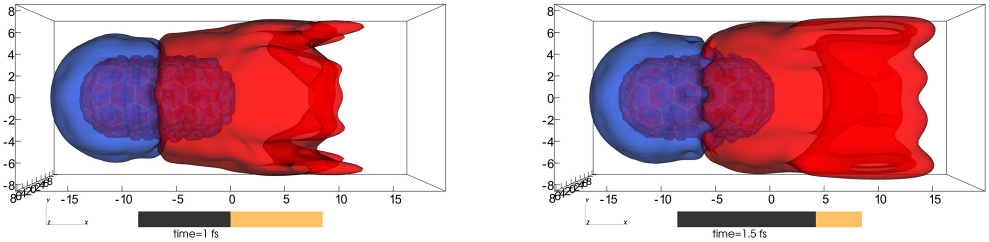

(e) t=1.0 fs

(f) t=1.5 fs

Figure V.19: Change in density vs. time around the (5,5) nanotube, at a field strength of 1.00 V/Å.

density around the structure.

These plots were created by subtracting the $t = 0$ density from the density at each time step. Red indicates regions where the density increased, while blue represents decreased density. This series of plots gives a sense of the time scale for the electron density dynamics. In the final plot of Figure V.19, the density is interacting with the sides of the calculation volume. Since these do not cause reflections along the nanotube axis, the current measurements are not affected. To confirm this, we repeated the calcuation using a larger simulation volume, and obtained the same current. See Figure V.20.

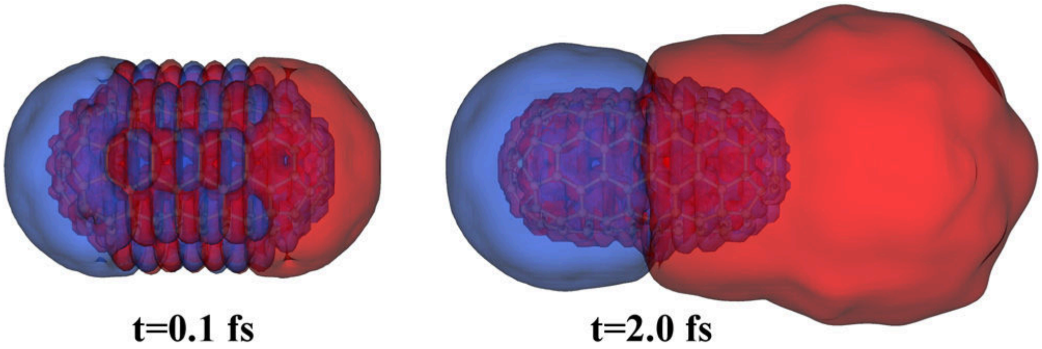

Figure V.20: Change in density around the (5,5) nanotube vs. time, using a larger box. Red indicates increases in density while blue shows decreases.

The time-dependent change of the potential and the electron orbitals show that the field emission is the due to the combined effect of electron excitation and a change in the potential barrier. The laser pulse excites the electrons that are close to the Fermi level and changes the shape of the potential that the electrons feel. The electron excitation changes the Hartree potential, further changing the potential barrier. Figure V.21 shows energy of the highest occupied orbital as a function of time. The energy strongly oscillates due to the laser field in the duration of the pulse. After the laser pulse, the energy decreases due to the change in the electrostatic potential caused by the excitation of electrons. The excited electrons tunnel through the time-varying potential barrier, producing pulse-like electron current.

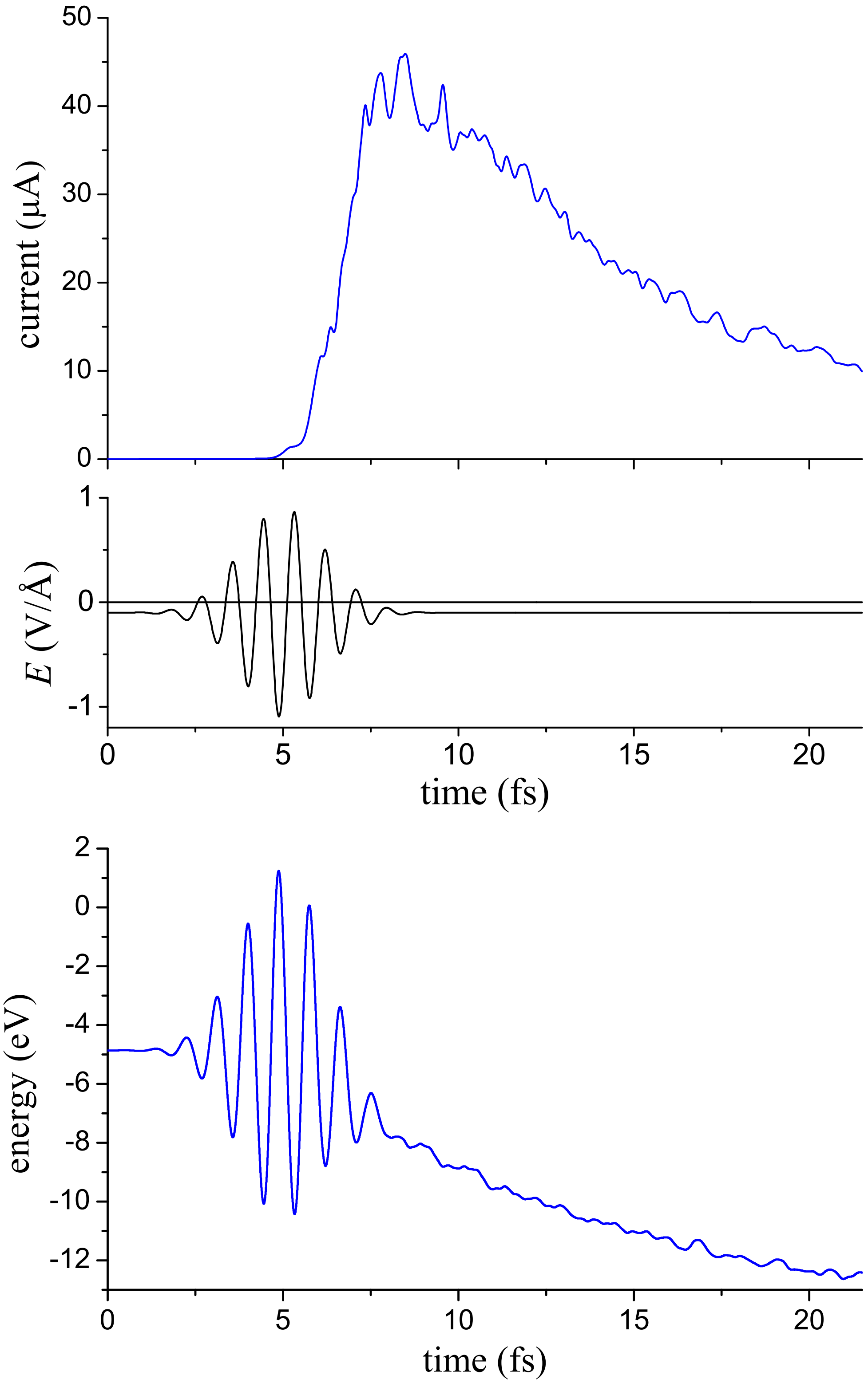

Figure V.21: Field emission from a (5,5) carbon nanotube due to static electric and laser fields acting together (top) and the laser pulse as a function time (middle). The bottom figure shows the energy of the highest occupied orbital as a function of time.

Table V.2: Maximum current values obtained with a static field of 0.1 V/Å only and with the static field and a laser pulse of 1.0 V/Å amplitude. All values are in μA.

	$C_{12}H_{14}$	(3,3) NT	(5,5) NT
static field	0.01	0.04	0.03
static field + laser pulse	12.4	20.3	45.9

5.2.2.3 Summary

We have investigated the emission of electrons from nanostructures induced by short intense laser pulses in the presence of a weaker uniform static field. Based on the results of our simulations, two important qualitative features of this process have been determined: (1) a significant enhancement of the emission when a laser pulse is applied, and (2) the field emission current has a peak of some duration and the position of this peak correlates with the time of the pulse arrival. These two features suggest the possibility of using short laser pulses for making few-electron emitters of nanoscale size [212]. Such emitters could have many desirable properties, especially very high spatial and time resolutions.

With the first-principles framework in place for these calculations, future work could include variations in laser frequency and intensity, the effects of adsorbates, or other effects. Interaction with experimentalists will be especially useful here, giving us guidance as to what configurations should be studied.

5.2.3 Nanotubes of varying composition

In addition to carbon, nanotubes of other types have also been synthesized which share some of the same desirable properties of CNTs. Examples include BN [183], SiC [184], Si [185], and GaN [186] nanotubes. In this section, field emission from various types of nanotubes is studied by propagating the electronic density in real space and time using time-dependent density functional theory. Capped (5,5) C, BN, SiC, Si, and GaN nanotubes are considered. The GaN, SiC, and Si nanotubes were found to be significantly better field emitters than C and BN nanotubes, both in terms of current magnitude and sharpness of peaks in the energy spectra. By analyzing the electronic structure of the various systems it is seen that the nanotubes with the highest currents have electron densities that extend significantly from the nanotube in the emission direction.

It is known [213, 214, 215, 216] that nanotubes can assume different geometries depending on parameters such as the number of atoms and the chirality. In order to see the differences in field emission properties caused by changes in composition, we kept other aspects of the nanotubes the same. They all had (5,5) chirality, end caps made from half-C60 molecules, and a total of 120 atoms per nanotube.

5.2.3.1 Generation of coordinates

To generate realistic coordinates for the various nanotubes, we needed to relax the coordinates of all atoms, rather than just a subset as in the previous sections. This made the task computationally unfeasible for ab initio relaxation. Instead, we performed classical molecular dynamics (MD) simulations using the Tersoff potential [217]. Parameters were taken from Refs. [218, 219] for C, Ref. [220] for Si and SiC, and Refs. [221, 222] for BN. Ref. [223] was used for the GaN structure. The Tersoff potential is an empirical interatomic potential that has been widely used to study the properties of semiconducting materials [217, 218, 220]. Through the incorporation of information about bond order in an atom's local environment, the Tersoff potential describes electronic structure effects (e.g., sp^3 bonding) more explicitly than conventional pairwise potentials. Its accuracy has been demonstrated through numerous forms of property prediction, ranging from lattice and elastic constants for crystalline structures [218, 220] to cohesive energies [224] and mechanical behavior [225, 226, 227] for nanotubes.

In carrying out the MD simulations, we utilized the LAMMPS [228] open source package with a time step of 2.0 fs and the equations of motion were integrated via the standard velocity Verlet algorithm. The simulations were performed in the canonical (constant NVT) ensemble with the Nosé-Hoover thermostat applied. To produce the final relaxed coordinates, the following annealing procedure was used: (i) run MD for 100 ps at 298K, (ii) run MD for 100 ps while ramping the temperature down from 298K to 0K, (iii) run MD for 50 ps at 0K. Figures V.22, V.23, and V.24 show the final structures.

5.2.3.2 Results

After the geometry of the nanotubes was optimized the ground state orbitals $\Psi_k(\mathbf{r}, t = 0)$ were calculated by solving the self-consistent Kohn-Sham equations. Once the ground state of the system is obtained, the electric field is turned on and time development for a few femtoseconds begins. The electric field is directed along the axis of the nanotube. The electric field's magnitude is increased slowly with a linear ramp over 0.2 fs (cf. Section 5.2.1.2). Once a steady state has been reached, the FE current is calculated using the method of Section 2.5 (see Table V.3).

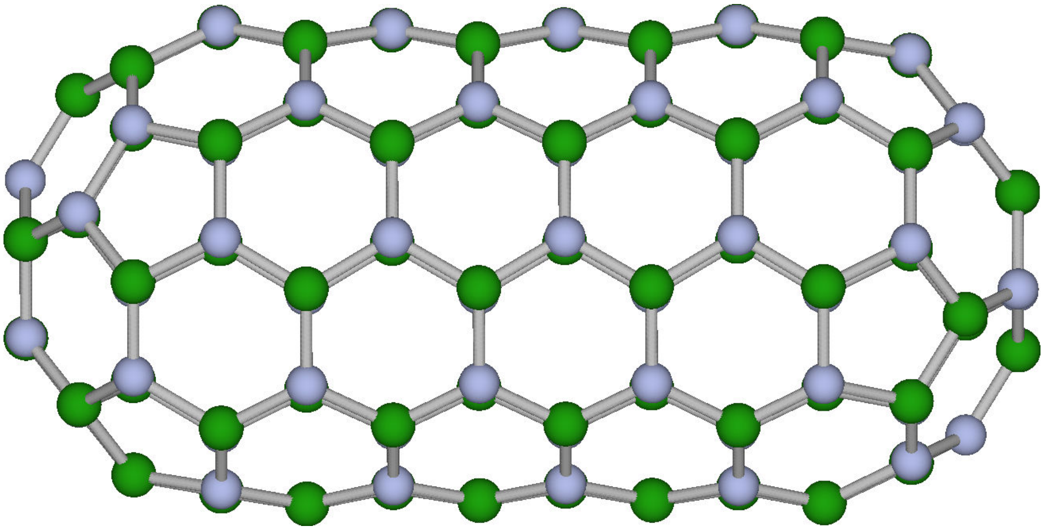

(a) BN

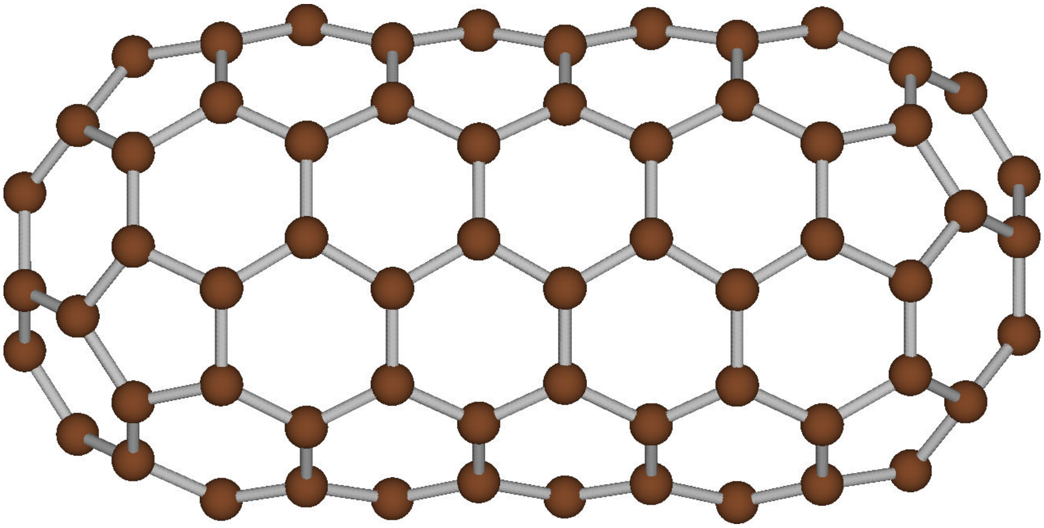

(b) C

Figure V.22: Relaxed structures for the (a) BN and (b) C nanotube used in the calculations.

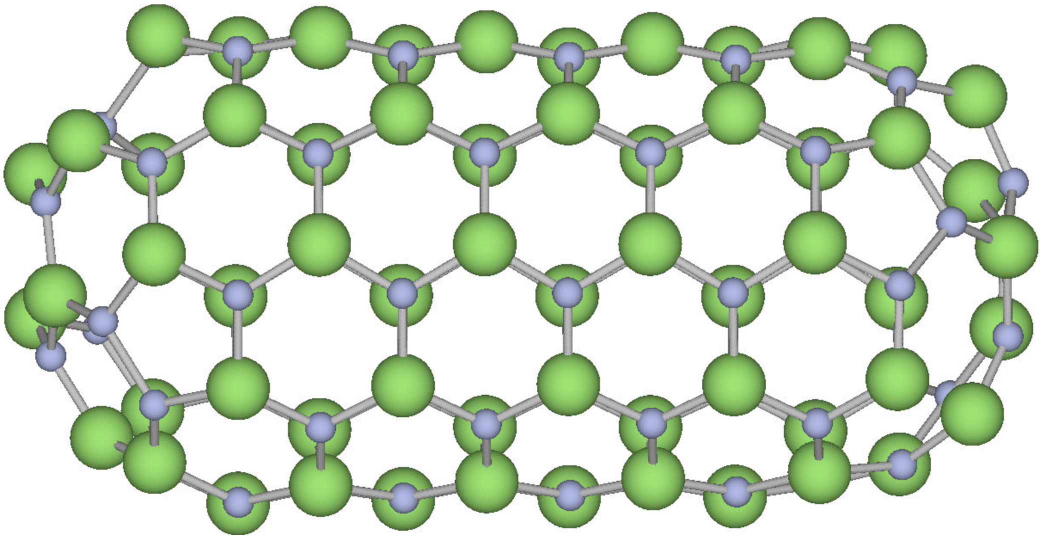

(a) GaN

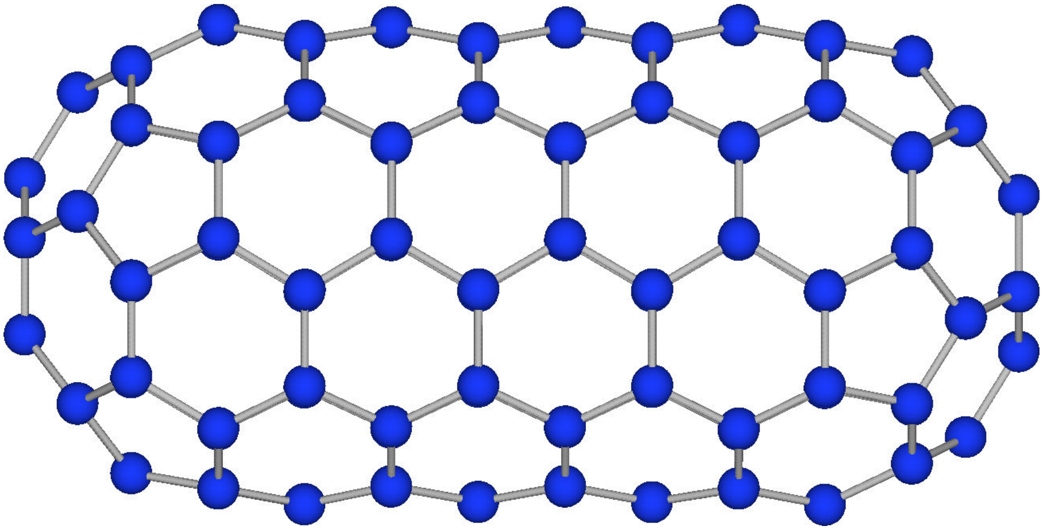

(b) Si

Figure V.23: Relaxed structures for the (a) GaN and (b) Si nanotube used in the calculations.

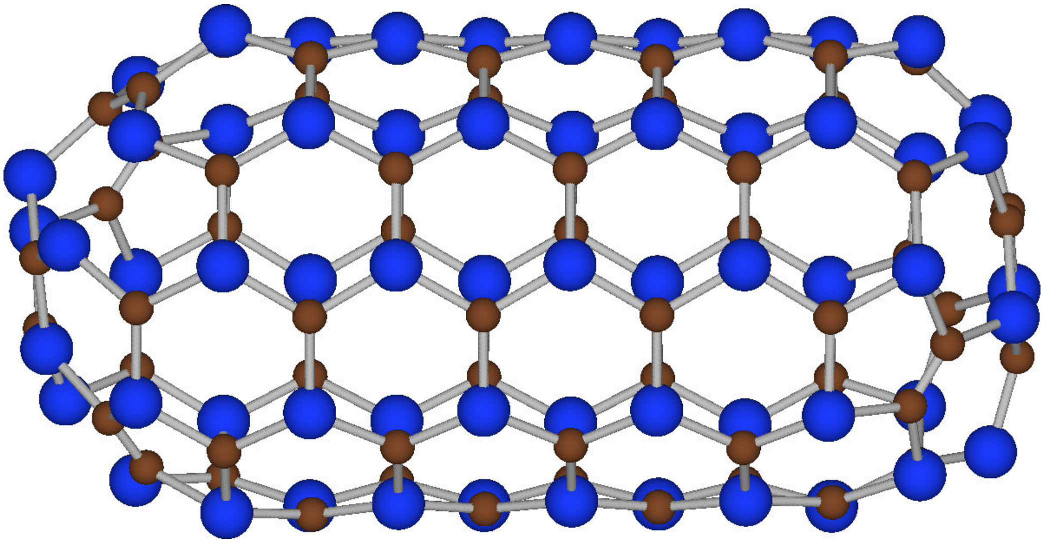

Figure V.24: Relaxed structure for the SiC nanotube used in the calculations.

	0.10 V/Å	0.50 V/Å	1.00 V/Å
C	0.024	1.297	29.384
BN	0.029	2.561	32.916
GaN	0.076	7.844	132.279
SiC	0.085	9.259	167.105
Si	0.162	28.292	347.537

Table V.3: Peak field emission currents (in μA) for (5,5) capped nanotubes with differing composition in varying electric fields.

Due to the high computational cost of the calculations, the size of the nanotubes is limited to 120 atoms. Once the electric field is turned on and the field emission starts, the nanotubes become charged due to the loss of electrons. This limits the length of the simulation time; once the electron deficiency of the nanotube becomes too large the field emission decreases (see Figure V.25). It should also be noted that increasing the number of atoms in a nanotube results in a somewhat increased current. Apparently, very long nanotubes are necessary in order to obtain completely converged values for the current magnitude, but this is computationally impractical.

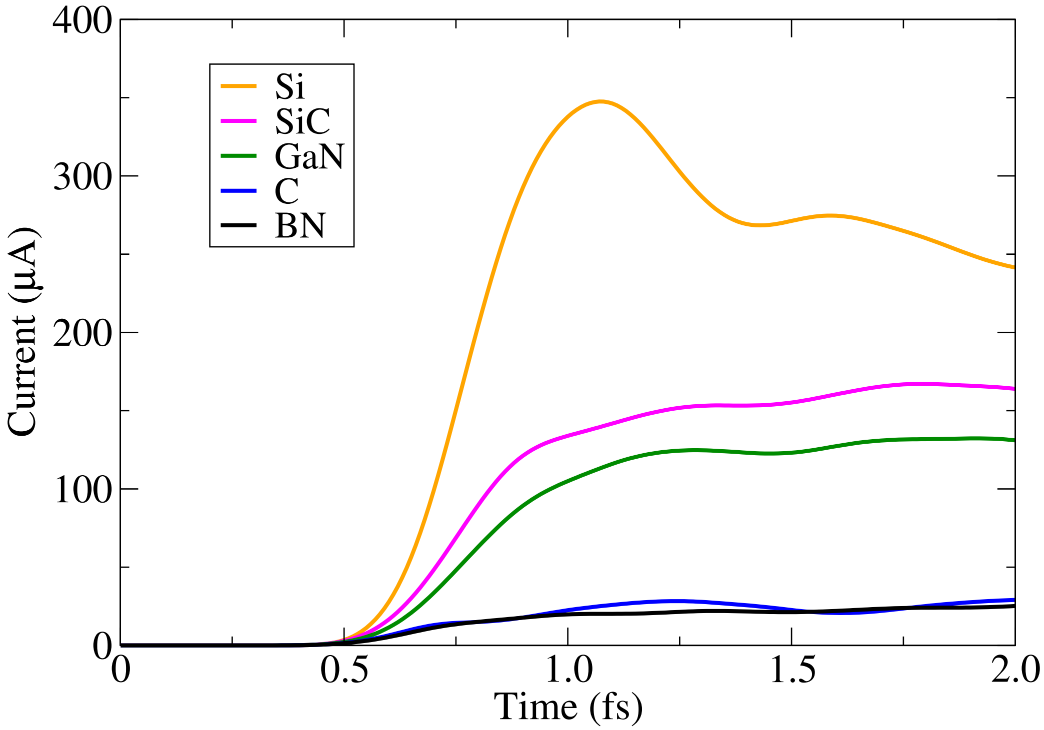

Figure V.25: Current vs. time for nanotubes of varying composition at the field strength of 1.00 V/Å.

The aim of the present simulations, however, is to study how the composition of the nanotubes affect their field emission properties. Since we keep the same number of atoms (and electrons) in all of our structures, it allows us to make a meaningful comparison.

The calculated currents for different electric fields are shown in Table V.3. The electric fields used in these calculations span the typical range of fields used in field emission experiments. The GaN, SiC, and Si nanotubes have much larger currents than the other nanotubes. BN and C nanotubes have similar current values, with BN being slightly higher.

Figure V.26 shows the profile of the local part of the potential in direction of the electric field (x-axis) for different electric field magnitudes (by profile we mean

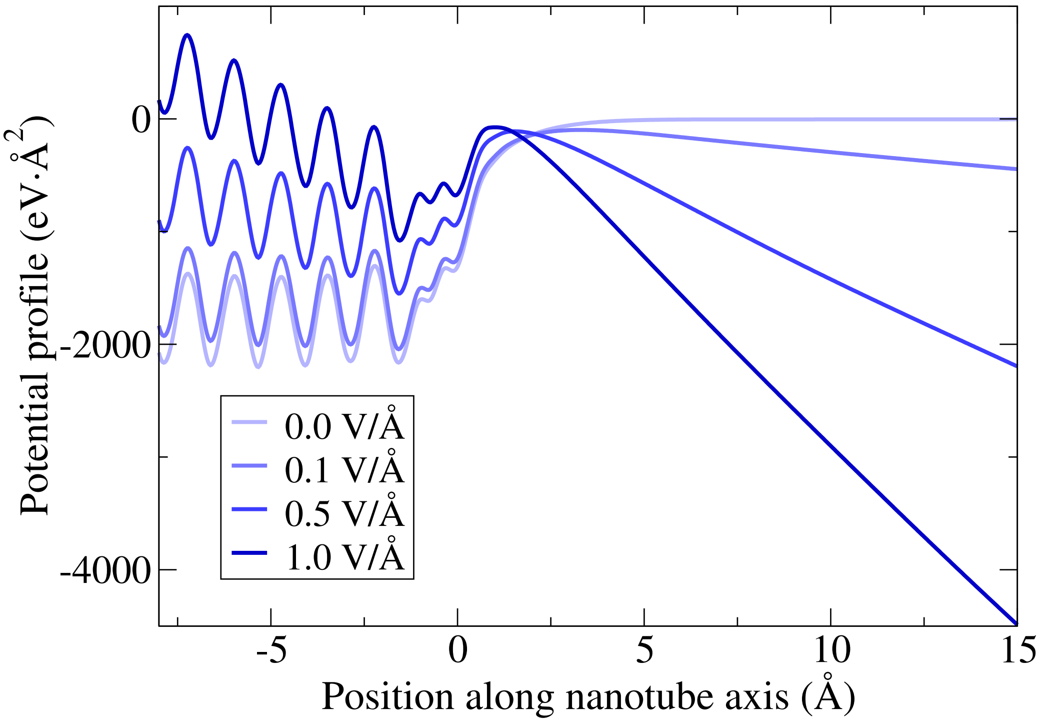

Figure V.26: Potential profile for 120 atom C nanotube at different electric field strengths.

the local potential integrated in the yz plane; i.e. it is a projection onto the x-axis). For higher electric fields the potential barrier lowers and gets narrower allowing higher electron currents. In the present calculations the core electrons are replaced by pseudopotentials which consist of both local and nonlocal parts. The use of nonlocal pseudopotentials makes the qualitative analysis of the potential profiles difficult. We cannot directly compare the potential distribution of nanotubes to study the reasons behind the differences in field emission currents because for different elements the contribution from the local and nonlocal parts differ.

In Figure V.27 the potential profile is plotted for the various nanotubes in the case of 1.00 V/Å field strength. It should be emphasized once again that this is an approximate picture, which lacks the contibution from the nonlocal part of the

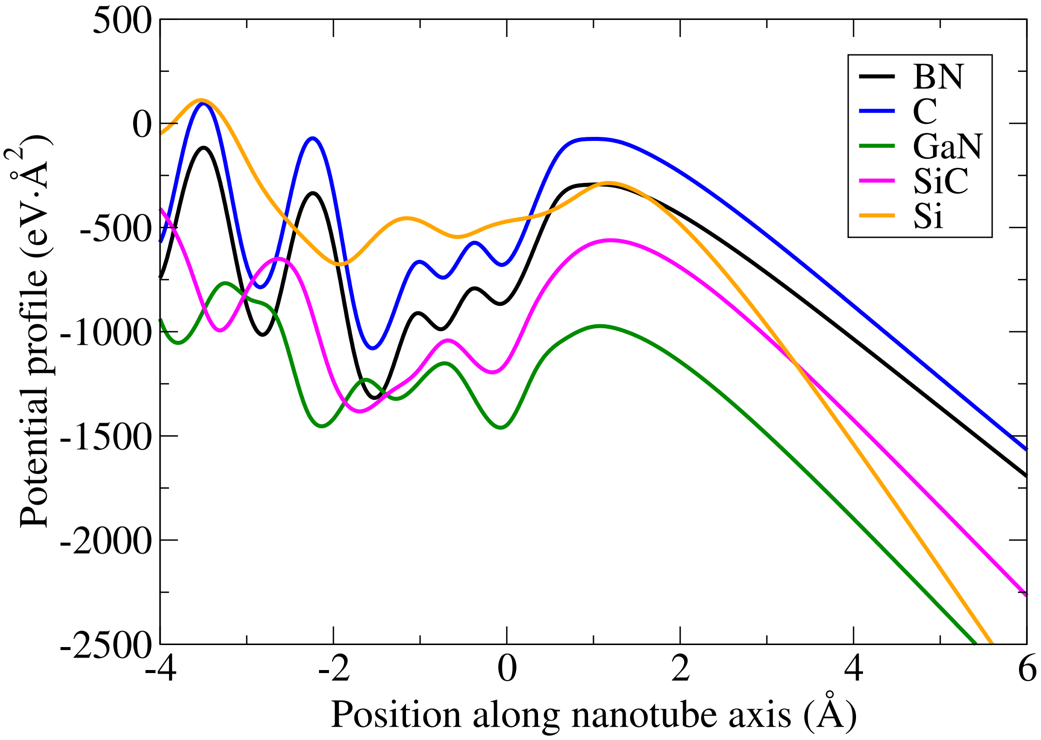

Figure V.27: Potential profile for various nanotubes at the field strength of 1.00 V/Å.

potential and does not show the full 3D structure of the total potential. Nonetheless, it serves as a good illustration of the basic mechanism that controls the field emission properties of various structures. As can be seen in Figure V.27 the potential barrier height and width for a given nanotube correlates quite well with the actual current intensity.

The density profile for the various nanotubes is shown in Figure V.28. This shows that for some of the nanotubes, the electron density extends further from the tube. From Table I we see that this correlates with higher currents.

Figures V.29, V.30, and V.31 show the current vs. energy distribution for the different nanotubes. The most intriguing feature of this figure is that the current is not emitted from one high lying orbital but instead originates from several states

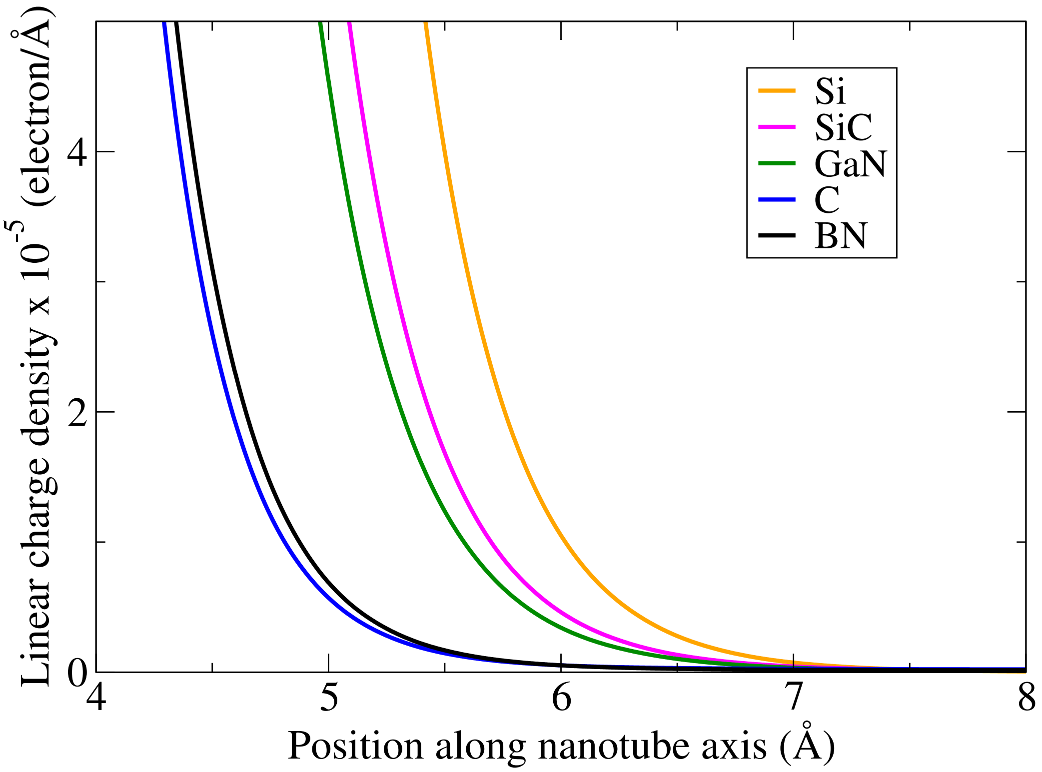

Figure V.28: Density profile for the different nanotubes at the field strength of 1.00 V/Å.

below the Fermi energy.

While Figures V.29, V.30, and V.31 show us which orbitals produced the most current, Figures V.32, V.33, and V.34 show which orbitals had significant density in the field emission region at the end of the nanotube. That is, it shows a local density of states for a volume starting 2 Å before the end of the nanotube and extending 10 Å beyond the end of the nanotube.

5.2.3.3 Summary

The field emission from nanotubes of various composition have been studied using time-dependent density functional theory. The calculations predict that the GaN, SiC, and Si nanotubes are particularly good field emitters. The highest-current nan-

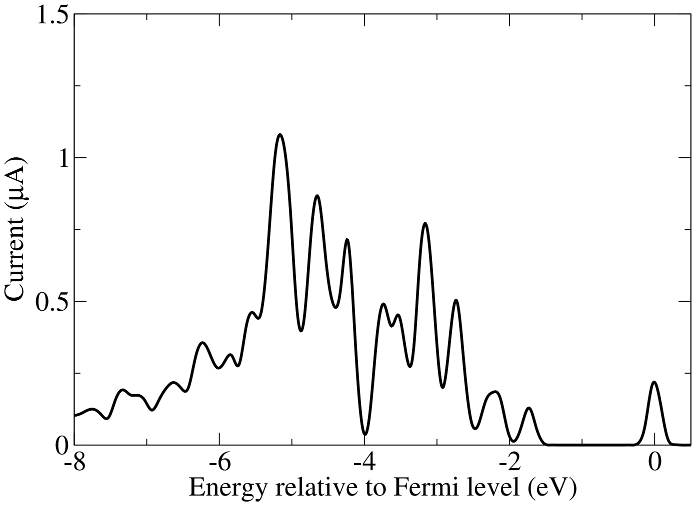

(a) BN

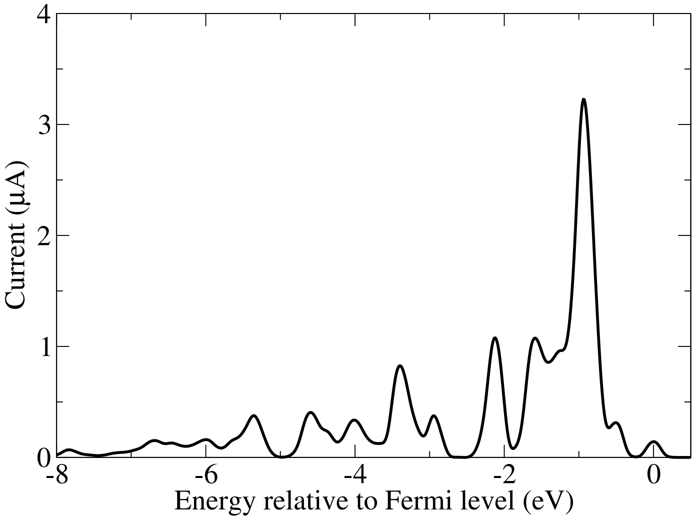

(b) C

Figure V.29: Current vs. energy, relative to Fermi energy, for the (a) BN and (b) C nanotubes at the field strength of 1.00 V/Å. The spectral peaks were broadened with Gaussians, using a full width at half-maximum of 0.2 eV.

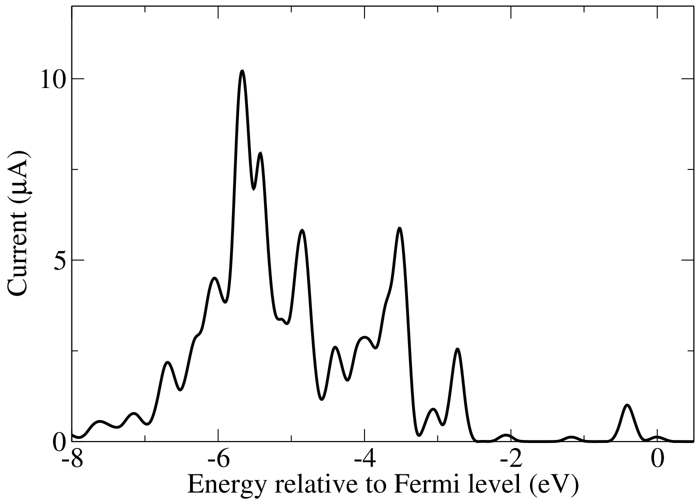

(a) GaN

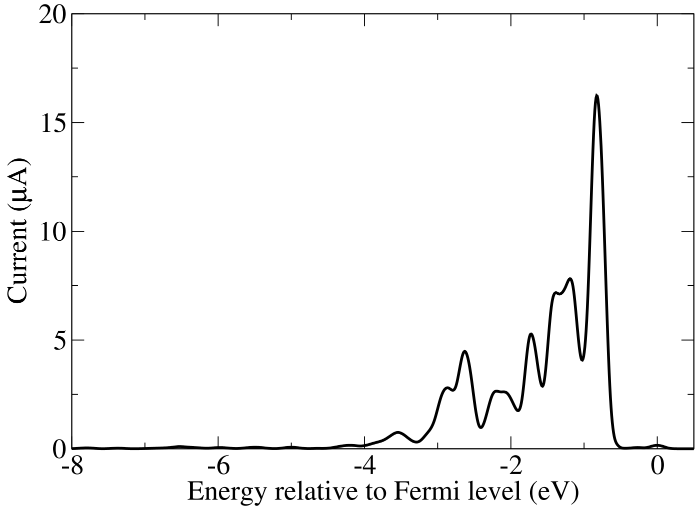

(b) Si

Figure V.30: Current vs. energy, relative to Fermi energy, for the (a) GaN and (b) Si nanotubes at the field strength of 1.00 V/Å. The spectral peaks were broadened with Gaussians, using a full width at half-maximum of 0.2 eV.

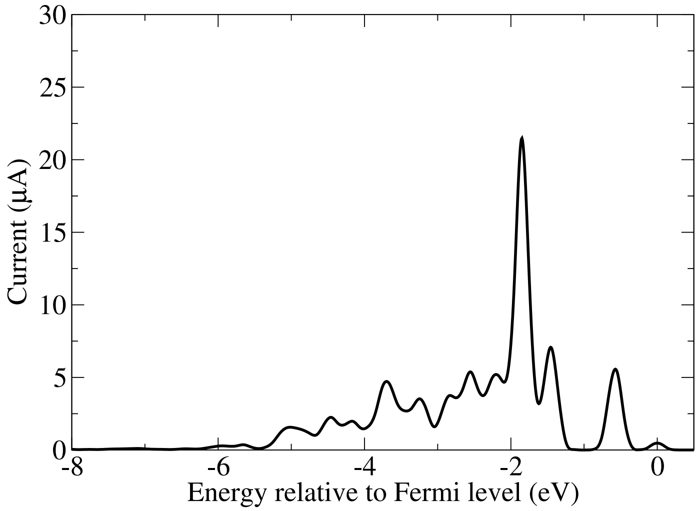

Figure V.31: Current vs. energy, relative to Fermi energy, for the SiC nanotube at the field strength of 1.00 V/Å. The spectral peaks were broadened with Gaussians, using a full width at half-maximum of 0.2 eV.

otube, Si, is predicted to produce a current an order of magnitude higher than BN or C nanotubes.

Future studies of these systems may explore the effects of adsorbates or defects in the atomic structures. In addition, encapsulation of atoms or molecules could be studied. Experiments are needed in order to determine the most interesting systems to consider.

5.2.4 Spin-polarized field emission from nanotubes

In addition to charge, the spin of an electron has the potential to become a fundamental carrier type in future technology [229, 230]. This will require the ability to control collections of spins, much like we now control collections of charges. This new area is called spintronics [231]. One type of this control is the ability to separate electron density into regions that are primarily one type of spin. These spin-polarized

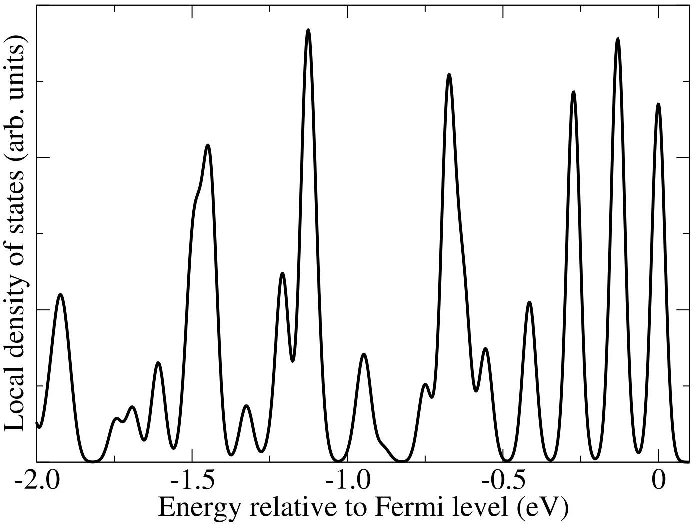

(a) BN

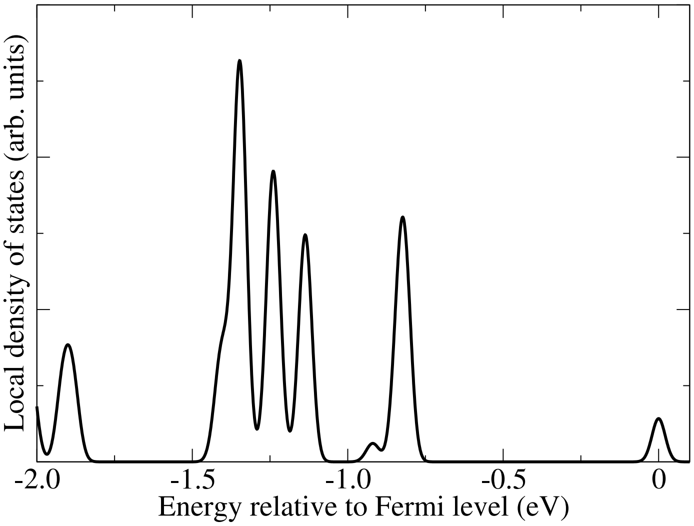

(b) C

Figure V.32: Orbital localization vs. energy, relative to Fermi energy, for the (a) BN and (b) C nanotubes at a field strength of 1.00 V/Å.

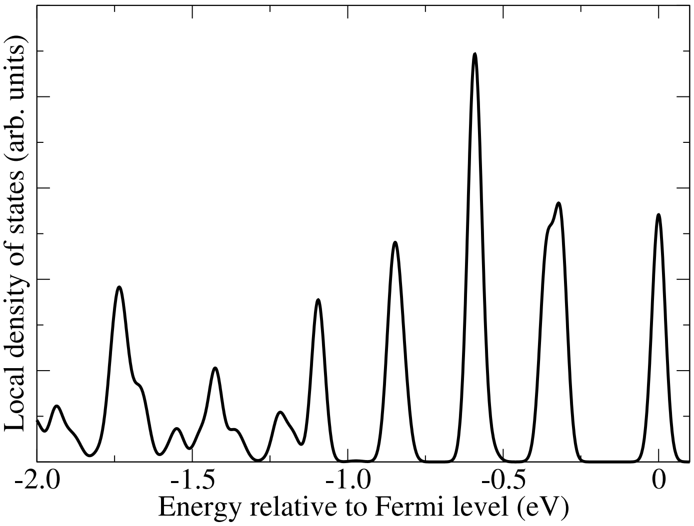

(a) GaN

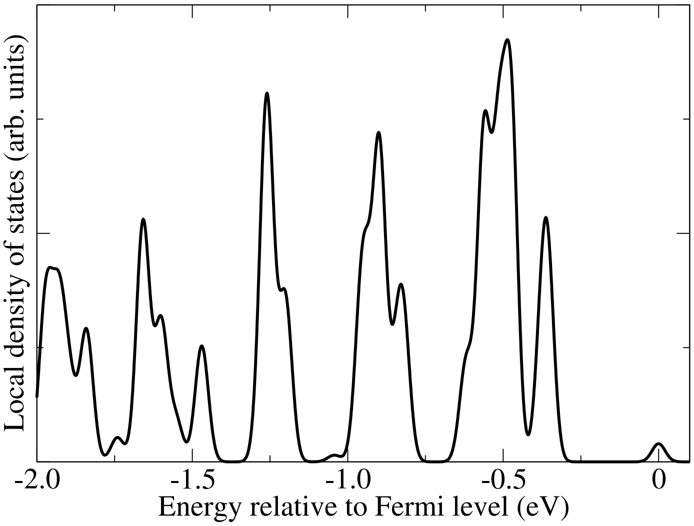

(b) Si

Figure V.33: Orbital localization vs. energy, relative to Fermi energy, for the (a) GaN and (b) Si nanotubes at a field strength of 1.00 V/Å.

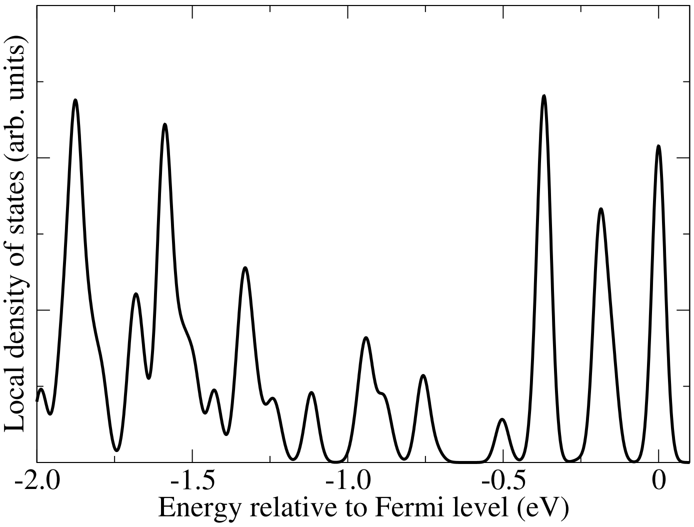

Figure V.34: Orbital localization vs. energy, relative to Fermi energy, for the SiC nanotube at a field strength of 1.00 V/Å.

density regions are then similar to collections of charge of a particular type.

This chapter presents results of spin-dependent field emission calculations for carbon nanotubes. This will allow us to see, for example, how various adsorbates (such as Fe atoms or clusters) affect the separation of density into spin-polarized regions. Experiments demonstrating spin-polarized field emission include a EuS-coated tungsten tip [232, 233] and bulk GaAs [234]. However, spin-polarized field emission from nanotubes has not yet been experimentally demonstrated.

The work of Hao et al. [235, 236] uses first-principles methods to calculate the electronic structure of Mn-doped GaN nanotubes, and the authors predict that spin-polarized field emission would result. In contrast, here we study carbon nanotubes, as they are likely to be more relevant due to their greater industrial availablity and other favorable properties relative to GaN nanotubes. As no theoretical studies yet exist that directly calculate the spin-polarized field emission current from carbon nanotubes, the present work fills this gap. By predicting which adsorbates generate spin-polarized current from nanotubes, we hope to generate experimental interest to check our results.

5.2.4.1 Extension of the code for spin-polarization

The TDDFT methods described in Chapter II were extended to include the physics of spin polarization. This required the use of a spin-polarized density functional for the exchange and correlation. The particular functional used is called the local spin density approximation (LSDA) [237]. In addition, the code was extended to keep track of up and down spin densities separately, which is needed when using LSDA. As a result of these modifications, we were able to calculate the current for up and down spins separately, in addition to the combined-spin results. This allows us to detect when there are signifcant differences between up and down spin currents, which indicates spin-polarization. The total electron density $n(\mathbf{r})$ is still used, and can be obtained from the separate densities for up and down spin ($n_\uparrow(\mathbf{r})$ and $n_\downarrow(\mathbf{r})$, respectively) as

$$n(\mathbf{r}) = n_\uparrow(\mathbf{r}) + n_\downarrow(\mathbf{r}). \tag{5.16}$$

The local spin density approximation (LSDA) to the exchange and correlation energy is given by [237]

$$E_{xc}^{LSDA}[n_\uparrow, n_\downarrow] = \int d\mathbf{r}\; n(\mathbf{r})\epsilon_{xc}(n_\uparrow, n_\downarrow) \tag{5.17}$$

where $\epsilon_{xc}(n_\uparrow, n_\downarrow)$ is the spin-dependent exchange-correlation energy density. Expressions for this have been determined via Monte Carlo calculations for the spin-polarized electron gas; a common choice is the expression from Perdew and Zunger [63].

5.2.4.2 Structural coordinates

Figure V.35 shows the Fe_4 cluster that was used. The coordinates for the cluster were taken from Ref. [6]. The (3,3) nanotube (without adsorbates) is shown in Figure V.36. Notice that the nanotube has been passivated with hydrogen atoms at each end, in order to satisfy dangling bonds. Figures V.37 and V.38 show this nanotube with an adsorbed Fe atom and Fe_4 cluster, respectively. Once these structures were created, they were allowed to relax via a spin-polarized VASP [238] calculation, in order to provide realistic geometries.

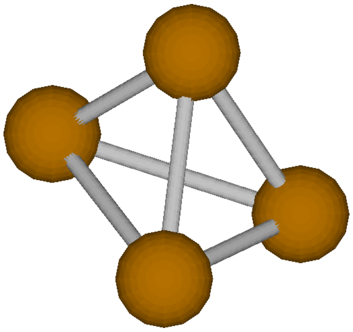

Figure V.35: Structure of the Fe_4 cluster used in the calculations. The coordinates used were obtained from Ref. [6].

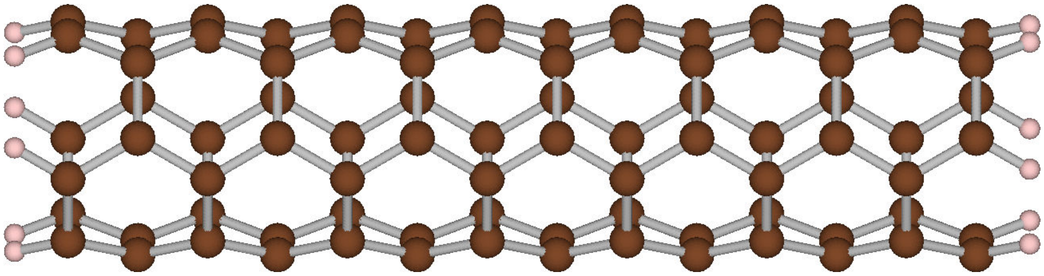

Figure V.36: Structure of a (3,3) carbon nanotube without iron adsorbates.

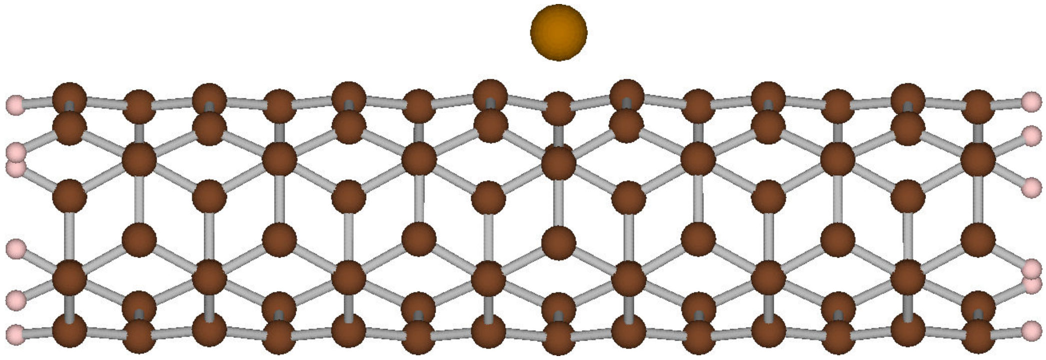

Figure V.37: Structure of a (3,3) carbon nanotube with an Fe atom adsorbed on the side.

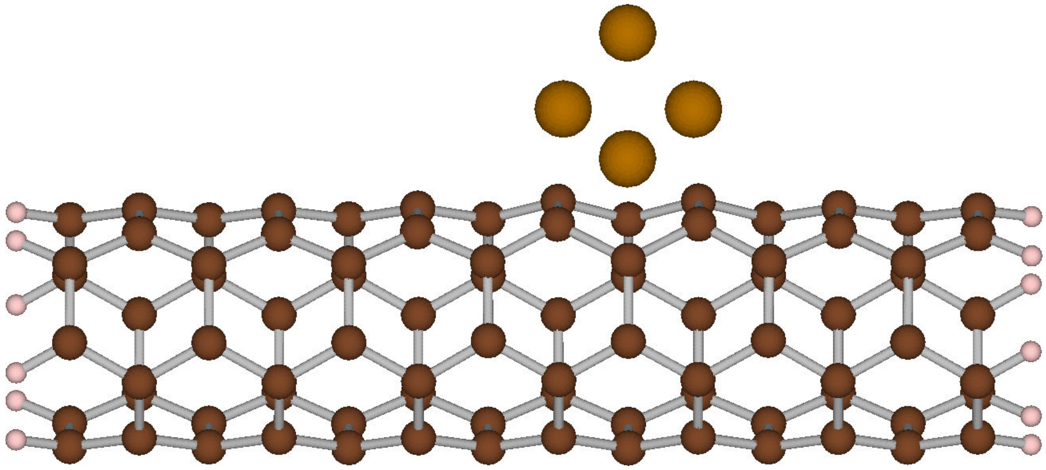

Figure V.38: Structure of a (3,3) carbon nanotube with an Fe_4 cluster adsorbed on the side.

5.2.4.3 Results

To provide a reference for evaluating the spin-polarized currents, we first consider spin-resolved field emission from the nanotube without iron adsorbates. Figure V.39 shows the field emission currents for the spin up, spin down, and total densities. These are indicated in the figure by I_{up}, I_{down}, and I_{total}, respectively. The electric field is directed along the axis of the nanotube. The applied field had a magnitude of 1.0 V/Å. For this structure, spin polarization was not present; the numbers of spin up and spin down electrons were the same. So, as expected, the plots for the spin up and spin down currents were identical and equal to one-half of the total current.

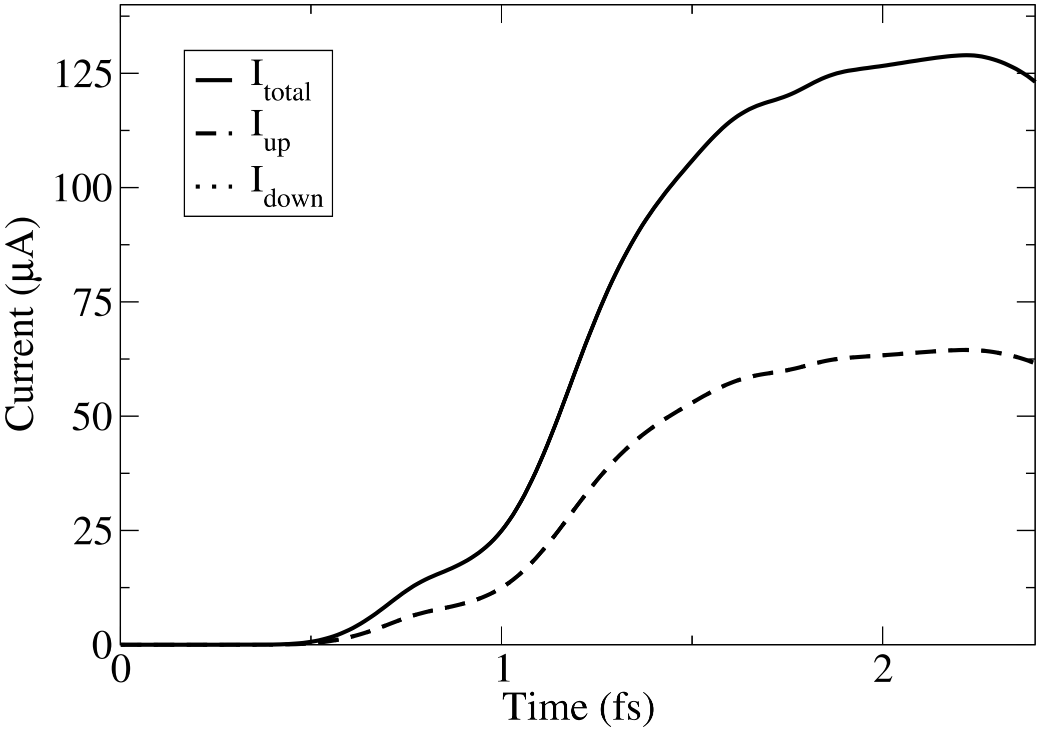

Figure V.39: Spin-polarized field emission current vs. time for a (3,3) carbon nanotube with no adsorbates. The applied electric field magnitude was 1.0 V/Å. The up and down currents are indistinguishable for this non spin-polarized structure.

We next consider the currents for nanotubes that have iron adsorbates. Figures V.40 and V.41 show the currents for an adsorbed Fe atom and Fe_4 cluster, respectively. These figures clearly show that the spin-up and spin-down currents are significantly different, with the spin down current exceeding the spin up current in both cases. This demonstrates spin polarized field emission in these systems. Figure V.42 plots the difference between spin up and spin down currents for the nanotubes with adsorbates. The separation between up and down spin currents is nearly the same, being slightly larger in the case of the Fe_4 cluster.

Figure V.43 compares the total (both spins) current for the three structures. Notice that the addition of either of the iron adsorbates reduces the total current

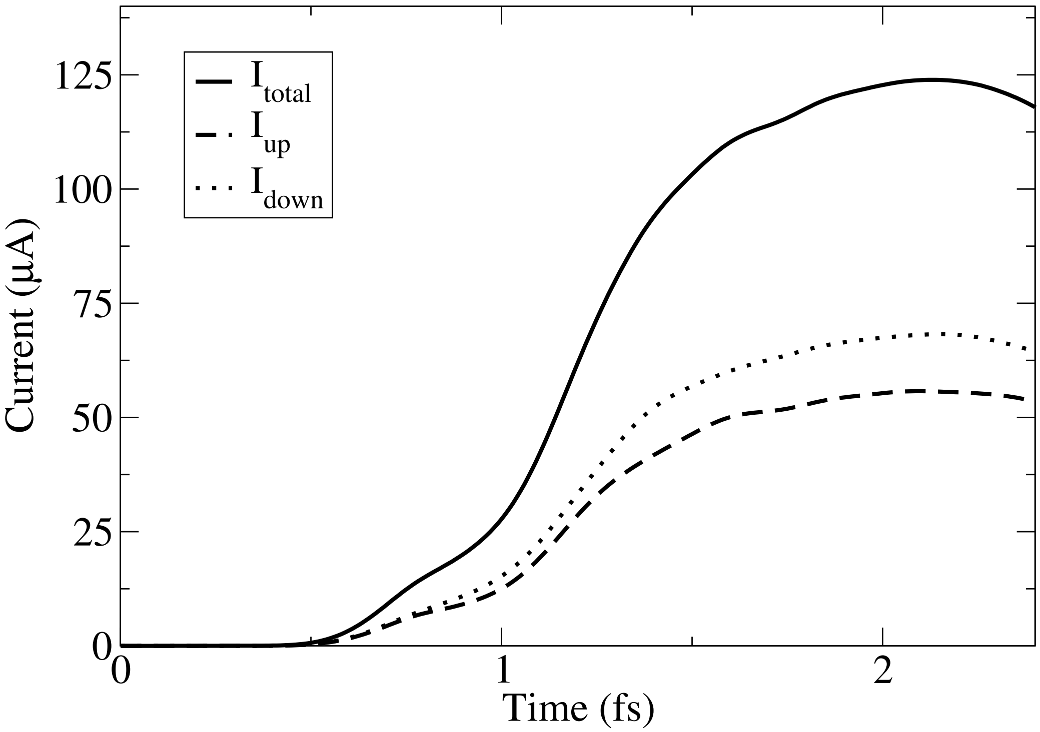

Figure V.40: Spin-polarized field emission current vs. time for a (3,3) carbon nanotube with an adsorbed Fe atom. The applied electric field magnitude was 1.0 V/Å.

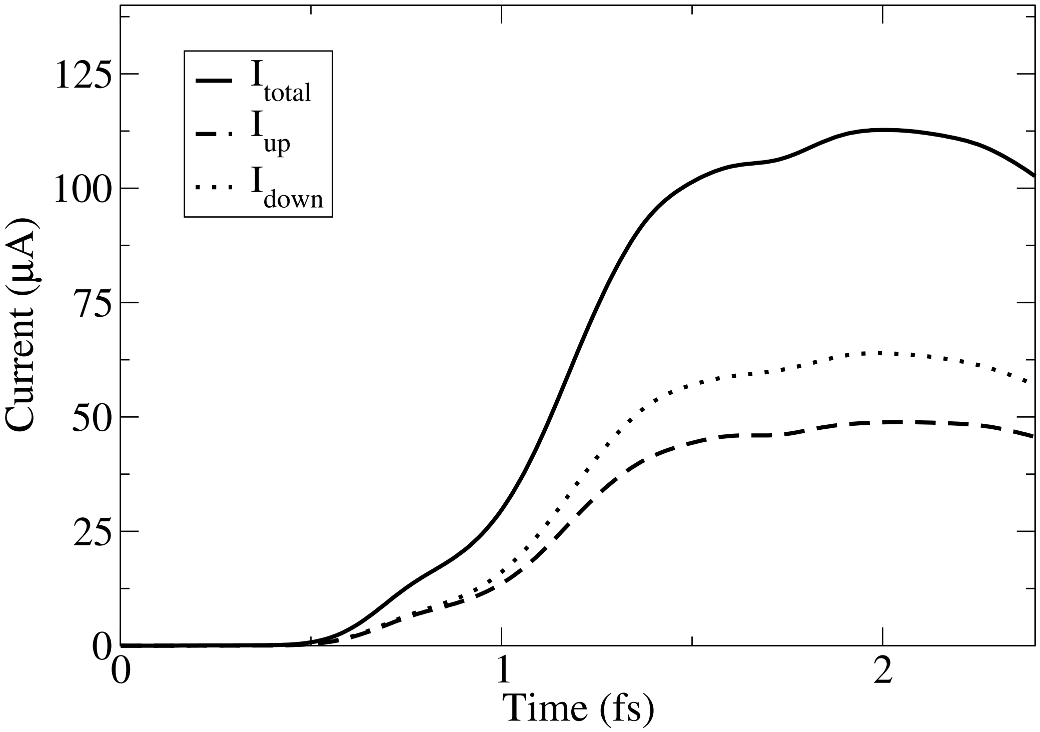

Figure V.41: Spin-polarized field emission current vs. time for a (3,3) carbon nanotube with an Fe_4 cluster adsorbate. The applied electric field magnitude was 1.0 V/Å.

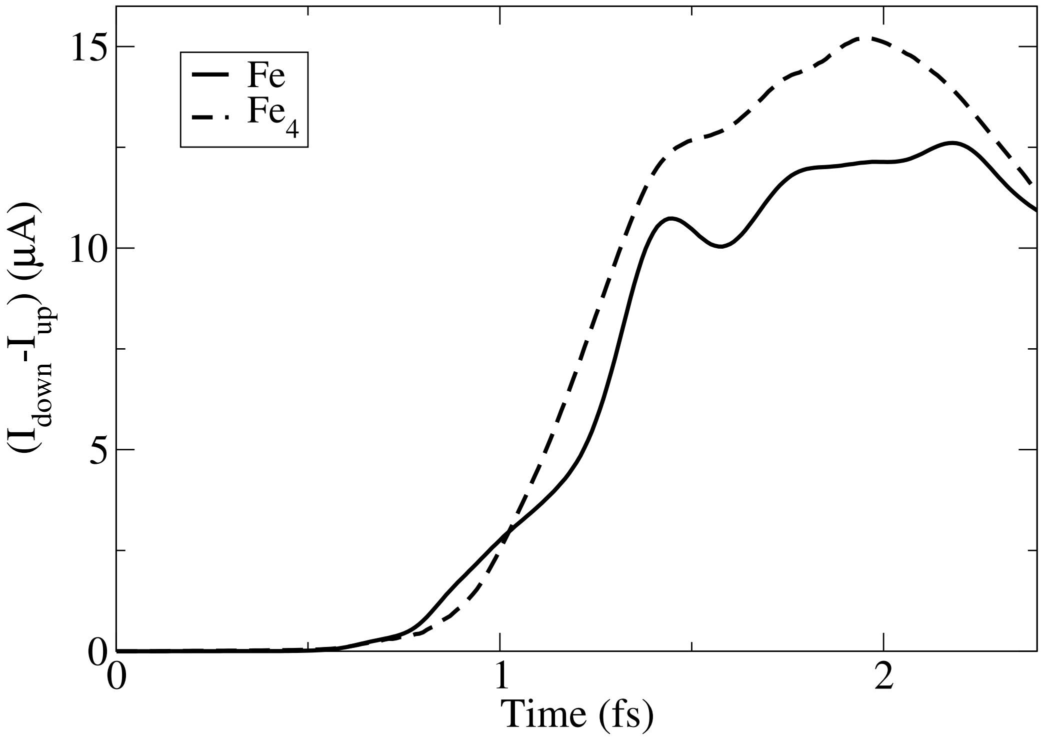

Figure V.42: Difference between spin-up and spin-down field emission current vs. time for a (3,3) carbon nanotube with an Fe atom and an Fe$_4$ cluster adsorbed on the side. The applied electric field magnitude was 1.0 V/Å.

of the nanotube, as compared to the no-adsorbate case. This reduction is more pronounced for the case of the Fe$_4$ cluster. Figures V.44 and V.45 compare the spin up and spin down currents, respectively, for the two types of iron adsorbate. For both up and down spin currents, the Fe atom adsorbate produces a higher current than the Fe$_4$ cluster, which explains the higher total current of the Fe atom case shown in Figure V.43.

5.2.4.4 Summary

These calculations predict that carbon nanotubes with iron adsorbates can be used as spin-polarized current sources. Both a single Fe atom and an Fe$_4$ cluster

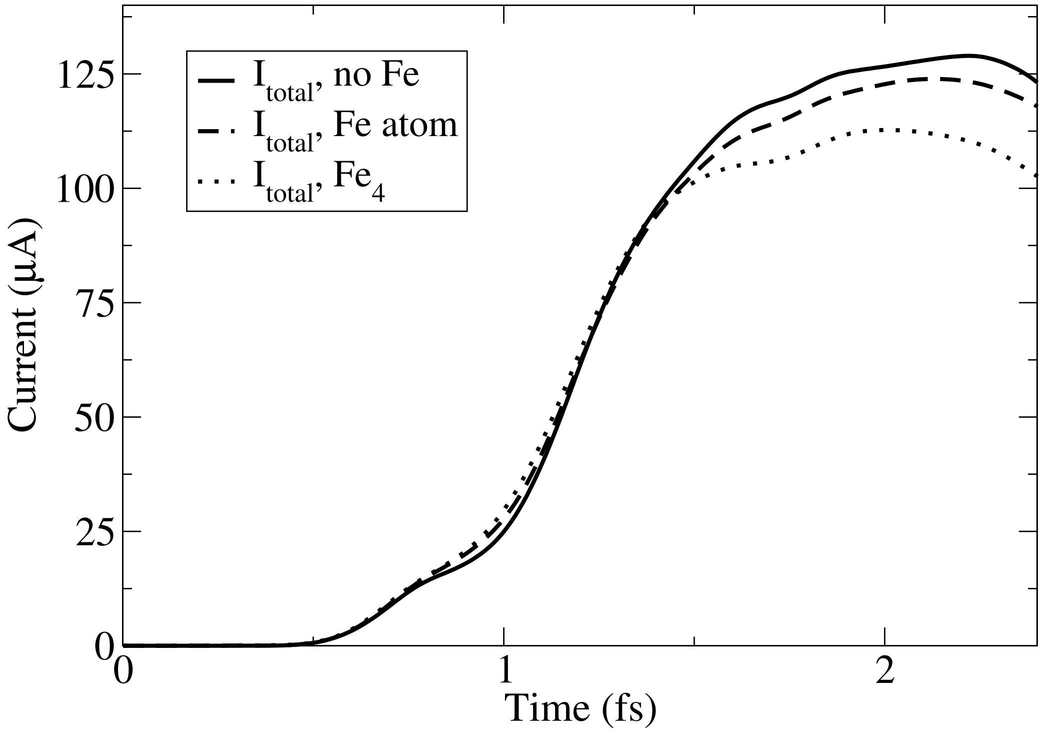

Figure V.43: Total field emission current vs. time for a (3,3) carbon nanotube with and without iron adsorbates. The applied electric field magnitude was 1.0 V/Å.

are shown to exhibit separations in their spin up and spin down currents. These are the first first-principles calculations to show spin-polarized field emission for carbon nanotubes with iron adsorbates. There is currently no experimental data with which to compare these results. However, the predicted strong spin-polarized field emission from these structures will hopefully spur experimental tests, potentially leading to applications within spintronics.

5.3 Field emission from nanowires

The aspect ratio (length to width) of a nanostructure such as a nanowire or nanotube is very high, leading to a strong enhancement of an externally applied electric field at the end of the chain. (This field enhancement due to structural

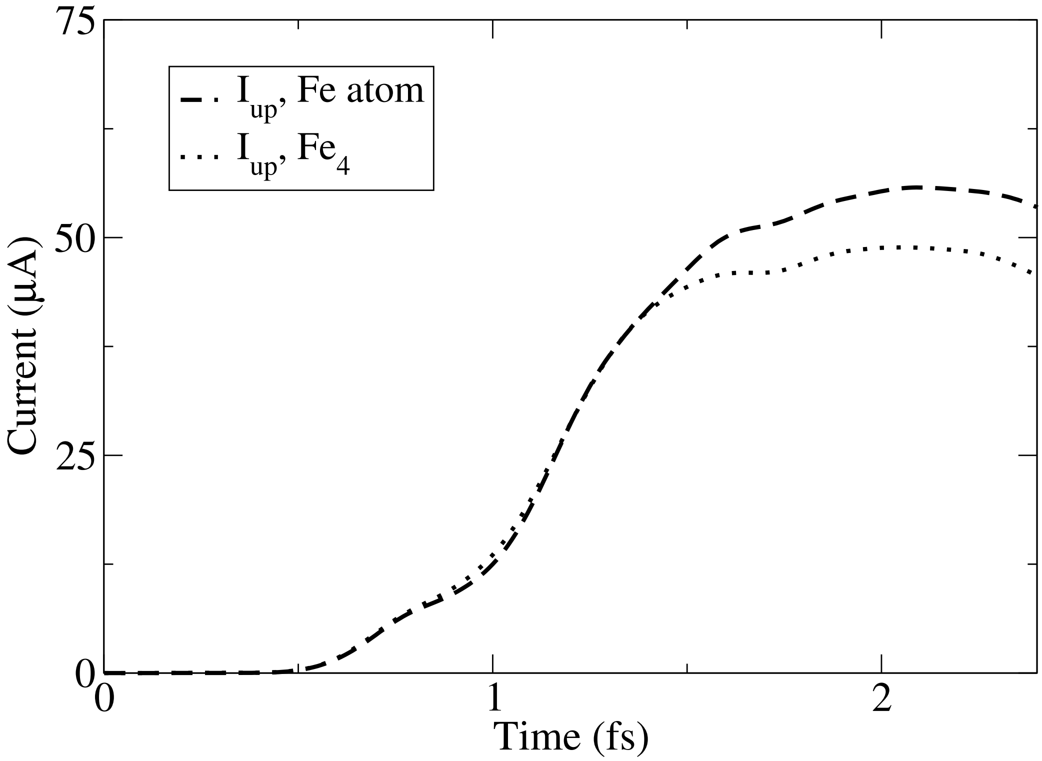

Figure V.44: Spin-up field emission current vs. time for a (3,3) carbon nanotube with an Fe atom and an Fe_4 cluster adsorbed on the side. The applied electric field magnitude was 1.0 V/Å.

geometry was discussed in Section 5.1.3.) For this reason, an obvious idea is to use a single atom chain as a field emission source.

There are some obstacles to using atomic chains as field emitters, however. The Peierls distorion [239] prevents atoms in a 1D lattice from being equally spaced and introduces a band gap. However, calculations [240] show that these distortions in a carbon chain are small, and so the introduced band gap is small enough to not significantly inhibit electronic conduction. Another issue is that while the high aspect ratio is attractive for enhancing the electric field, a 1D nanowire lacks the structural strength of larger structures such as nanotubes.

A carbon nanowire (see Figure V.46) is a one-dimensional system of carbon atoms.

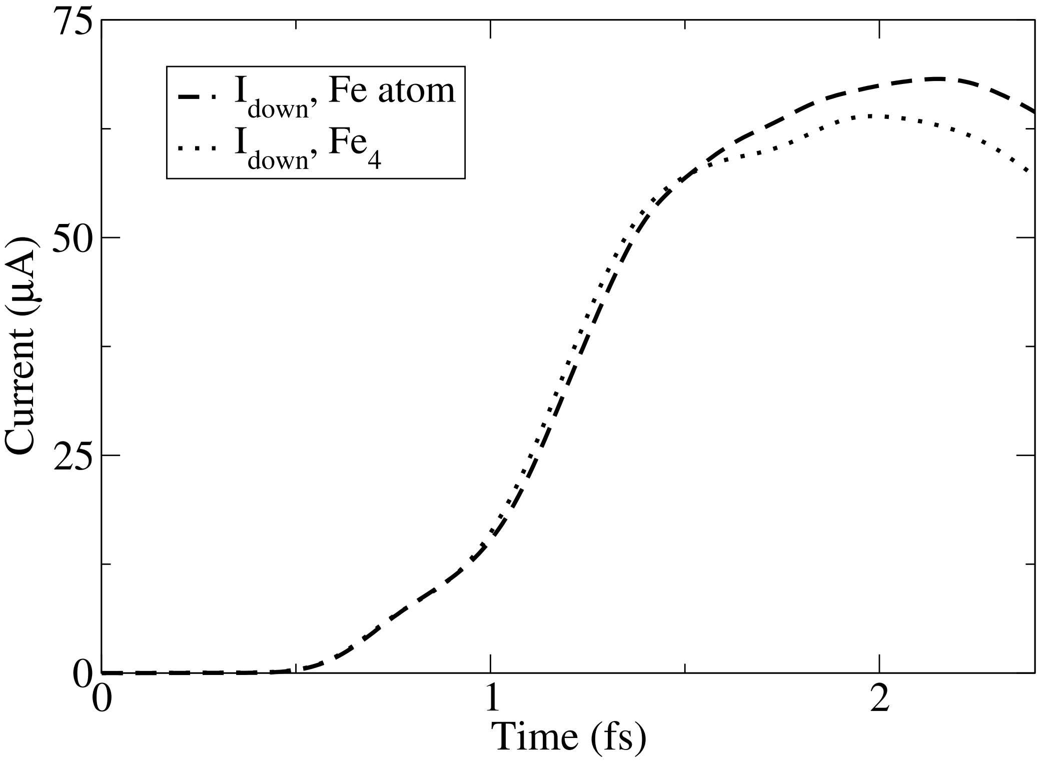

Figure V.45: Spin-down field emission current vs. time for a (3,3) carbon nanotube with an Fe atom and an Fe_4 cluster adsorbed on the side. The applied electric field magnitude was 1.0 V/Å.

Nanowires are relatively long (e.g., microns) in the axial direction, but nanoscale in

Figure V.46: A carbon nanowire passivated with hydrogen atoms.

the others. In Figure V.46, notice that there are also hydrogen atoms. These serve to passivate dangling bonds. A dangling bond exists on an atom if it has an unsatisfied valence shell. Without the addition of these hydrogen atoms, the lowest energy structure would be, due to the dangling bonds, something more complicated than a 1D wire. This is because the dangling bonds would cause the carbon atoms to become attracted to each other in order to form bonds and satisfy their valence requirements. Since we want a particular structure, i.e. a 1D wire, we can passivate the dangling bonds with hydrogens. This is a realistic situation for a structure prepared in a hydrogen atmosphere.

The experimental motivation for studying field emission from carbon chains started with the work of Rinzler et al [172]. They mounted a single multiwall carbon nanotube to a graphite fiber electrode and studied its field emission properties. First they applied a voltage that was not sufficient to achieve field emission unless the nanotube was heated by a laser (i.e., the Schottky mechanism [10]). The laser was applied in seconds-long pulses, and so the nanotube was alternately heated and allowed to cool. A plot of field emission current vs. time shows steady current when the laser was on, and no current when the laser was off.

They then opened the end of the nanotube by heating the end to a temperature twice that of the previous heating. They then repeated the process of shining the laser on the nanotube and recording the field emission current. When the laser was on, the current was more than two orders of magnitude greater than in the closed nanotube case. The speculation is that while the closed cap provides a geometric field enhancement effect, the ragged edges of a blown-open open end would provide an even greater enhancement.

When the laser was off, the emission current was not zero, as in the closed tube case. Instead, the current increased by another factor of 100. That is, the current in the open tube case was enormous when the laser was off. This is to be contrasted with the closed tube case, in which the current was practically zero when the laser was off.

The speculated reason for this unexpected result is that, with the laser off and the opened tube end allowed to cool, the atoms were pulled out by the external electric field and formed a monatomic chain of 10-100 carbon atoms. This chain provides a huge enhancement factor for the electric field, resulting in large field emission. Such a chain would be destroyed by the added energy of the laser [241], and so that is why laser heating reduced the current. During the no-laser emission, the authors did observe rapid fluctuations of the current that were likely due to reconfigurations of the chain(s) from Joule heating. Lim et al. [242] also report observing these effects.

Inspired by the work of Rinzler et al., Lorenzoni et al. [243] used the WKB approximation to calculate field emission from carbon chains. Current-voltage plots follow Fowler-Nordheim [30] theory, indicating metallic behavior. The chains are also found to be highly polarizable, and for the most part emit electrons monoenergetically. They also show that the photoabsorption cross section has one major peak, in agreement with experimental findings [244].

Fan et al. [245] use DFT to study carbon chains alone and inside carbon nanotubes. They focus on seeing how changing the parity (even or odd number of C atoms) and termination (hydrogen or no hydrogen at the ends) affects various properties. These properties include the HOMO-LUMO gap and optical spectra. For chains inside CNTs, they additionally discuss the potential energy inside the tube. They note that, at least for the (8,0) CNT, the potential energy is ~ 1 eV lower inside the tube, which may explain why carbon chains would form there. In addition, the walls of the CNT have alternating deep potential wells that stabilize the linear chain.

Rusznyák et al. [246] use DFT to show that the chain and CNT engage in charge transfer and reach a common Fermi level. Lucotti et al. [247] combine experiment and

DFT to discuss the Raman and surface-enhanced Raman spectroscopic properties of carbon chains. Bianchetti et al. [248] use DFT to calculate absorption spectra and polarizability of carbon chains.

We have calculated the field emission for a more realistic nanowire, $C_{12}H_{14}$, which is shown in Figure V.47. Figure V.48 shows the field emission current vs. time for three applied fields. For all three fields, the currents increase, peak, then decrease. In addition, the peak currents are much lower than the currents seen for the nanotubes of previous sections. Since the nanowire has only a few atoms, when it field emits a non-trivial amount of charge is lost from the device. This positive charging deepens the confining potential, effectively increasing the work function. Another part of this effect is that once charge is flowing into the vacuum region, it can repel the charge that is trying to follow it. These effects are common to all of the results in this dissertation. Despite these phenomena, the peak current is still an identifiable feature of the plots.

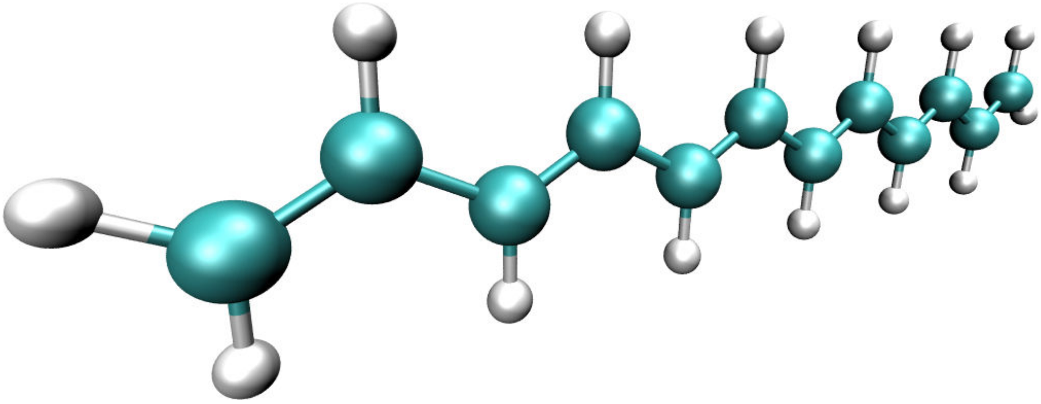

Figure V.47: The $C_{12}H_{14}$ molecule used in the calculations.

Since there is not yet any experimental work on field emission from isolated carbon nanowires, we cannot compare these results to experiment. This section is still useful

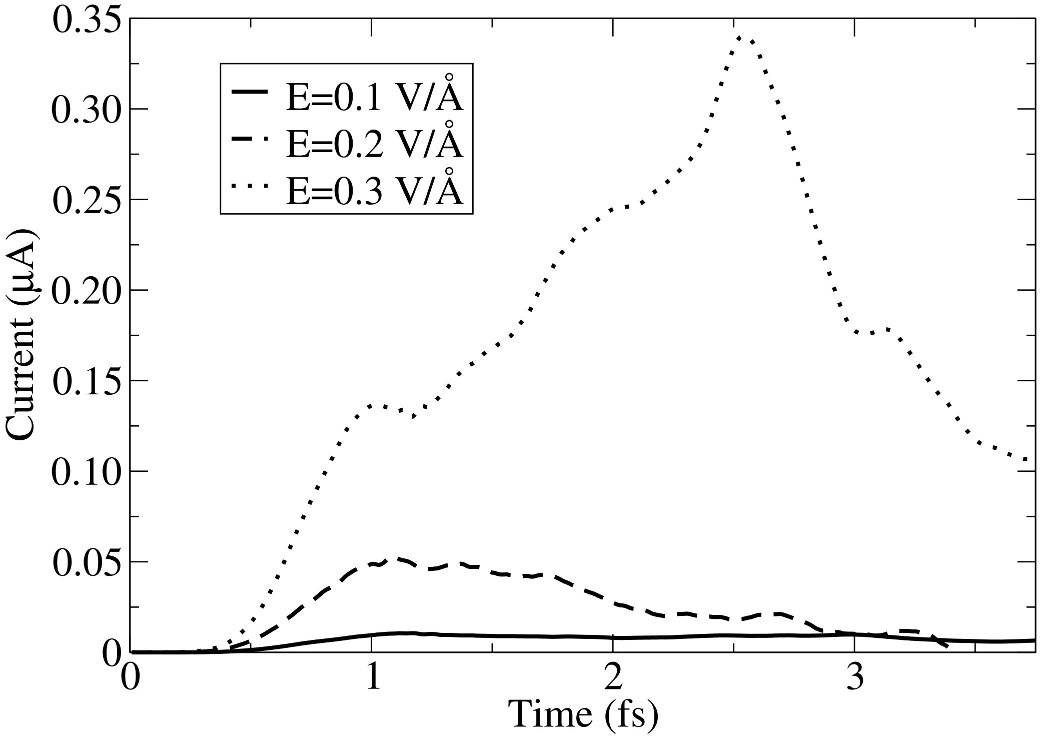

Figure V.48: Field emission current from a $C_{12}H_{14}$ molecule at varying electric fields.

in demonstrating the ability of our framework to study non-nanotube structures. The next section considers graphene nanoribbons.

5.4 Graphene

In the case of graphene, which has a two-dimensional sheet structure (see Figure V.49), the thickness of the material is only an atom thick, and so this dimension is at the nanoscale. Its other dimensions (i.e., directions parallel to the sheet) can be much larger.

It is only in the last few years that single sheets of graphene could be reliably fabricated [249]. Graphene can be produced by applying carbon atoms on a substrate to produce a thin coating; this process is called epitaxy [250, 251]. One disadvantage

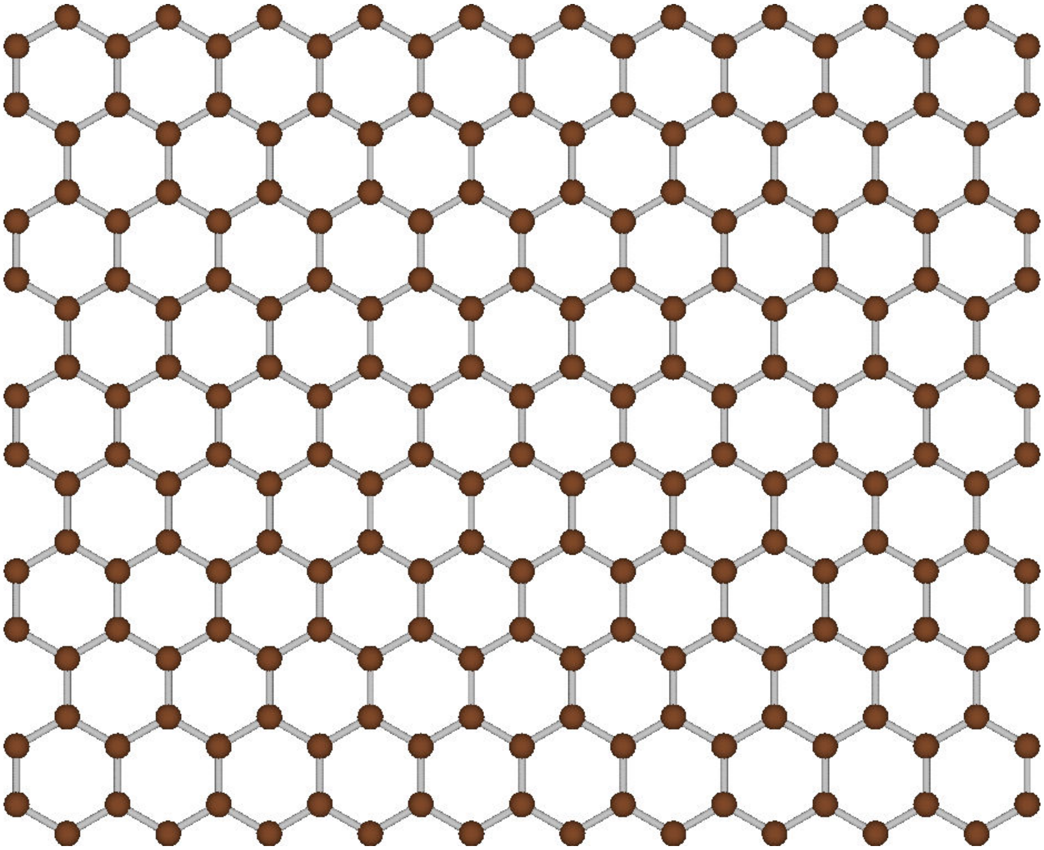

Figure V.49: A portion of a graphene sheet. The structure continues far away in the in-plane directions.

with this method is that the substrate can have significant influence on the grown graphene, resulting in altered electrical properties [252].

Another method of obtaining graphene is called mechanical exfoliation [253]. Many graphene sheets are bound together in graphite, a macroscopic material. The bonding between sheets is much weaker than within sheets, which means that pulling layers off one (or a few) at a time is practical. Until 2004, this usually produced samples having at least tens of graphene layers. In 2004 Geim and Novoselov refined the technique such that exfoliation of single graphene sheets were possible [249]. They were awarded the 2010 Nobel Prize in physics for their work in graphene.

5.4.1 Field emission from graphene nanoribbons

A sheet of graphene can be relatively large in the in-plane dimensions, and so in Figure V.49 only a small portion of a sheet is shown. Since this portion is assumed to not be near edges, no passivating hydrogens were added (in contrast to the nanowires discussed above). Now consider a graphene sheet that is cut such that only one of the in-plane dimensions is large. In this case a ribbon-like structure is obtained. Graphene nanoribbons can be conducting or semiconducting, depending on the details of their structure [254].

We now examine the field emission behavior of graphene nanoribbons (GNRs). Hydrogen passivation is used to satisfy the dangling bonds on the edges of the ribbons. As part of this study, we compare field emission behavior with and without hydrogens on the edge that emits. In all cases, the other three edges have hydrogens. One can imagine rolling these ribbons up (along the emission axis) into nanotubes. For comparison, we do create such nanotubes, and compare their field emission performance to that of the corresponding nanoribbons. Figures V.50-V.53 show the structures used in the calculations.

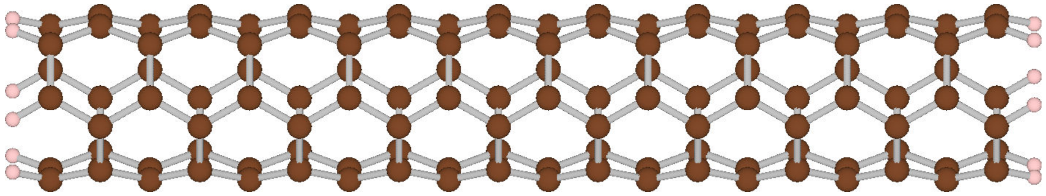

Figure V.50: Structure of a (3,3) carbon nanotube with passivating hydrogens.

Figures V.54-V.57 show the field emission currents of these structures as a function of time, for different electric fields.

As with the nanowire of Section 5.3, there is currently no experimental work with

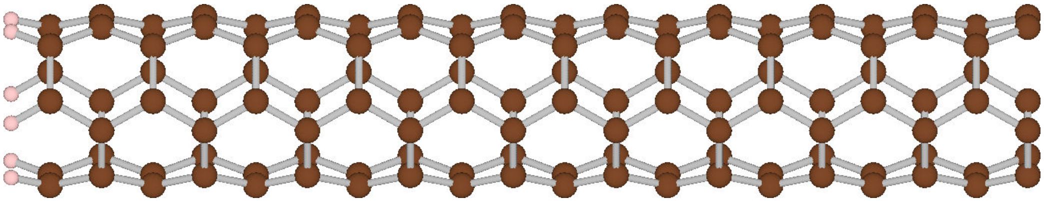

Figure V.51: Structure of a (3,3) carbon nanotube without passivating hydrogens.

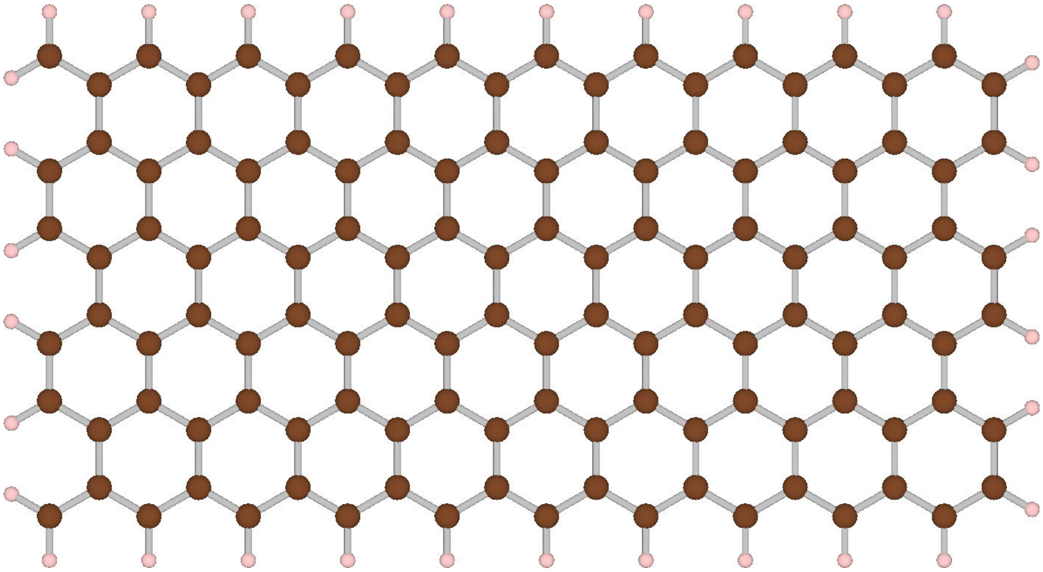

Figure V.52: Structure of a (3,3) graphene nanoribbon with passivating hydrogens.

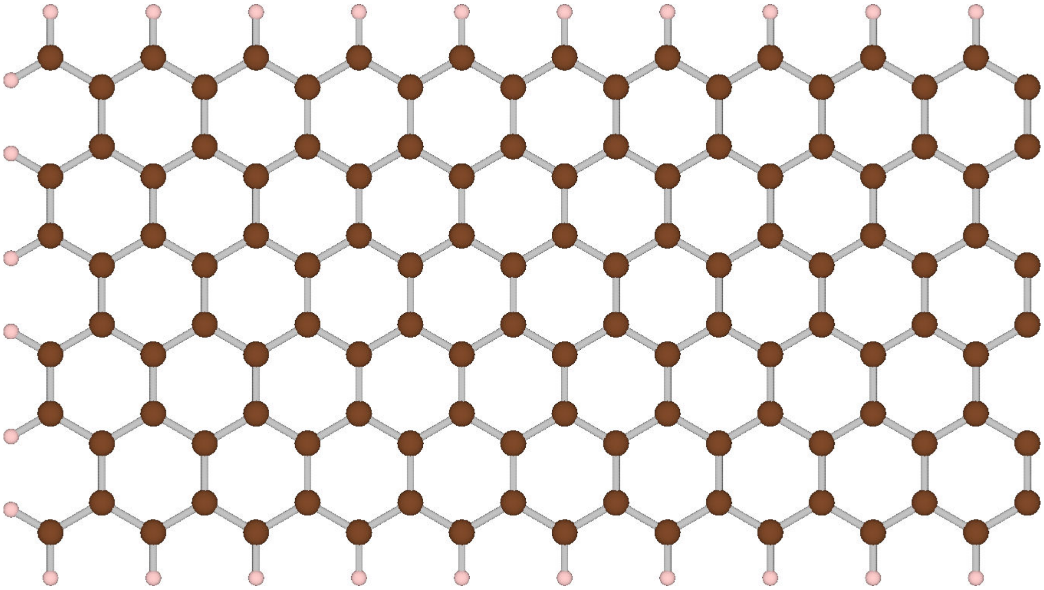

Figure V.53: Structure of a (3,3) graphene nanoribbon without passivating hydrogens.

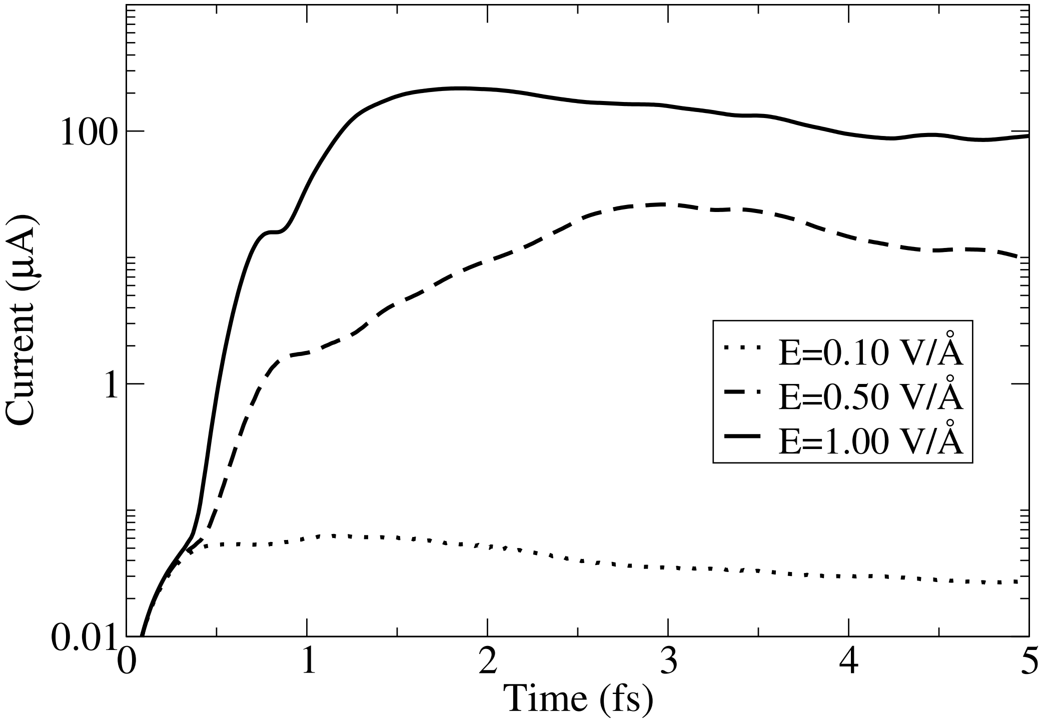

Figure V.54: Field emission current vs. time for a (3,3) hydrogen-terminated graphene nanoribbon. Curves for three different applied electric fields are shown.

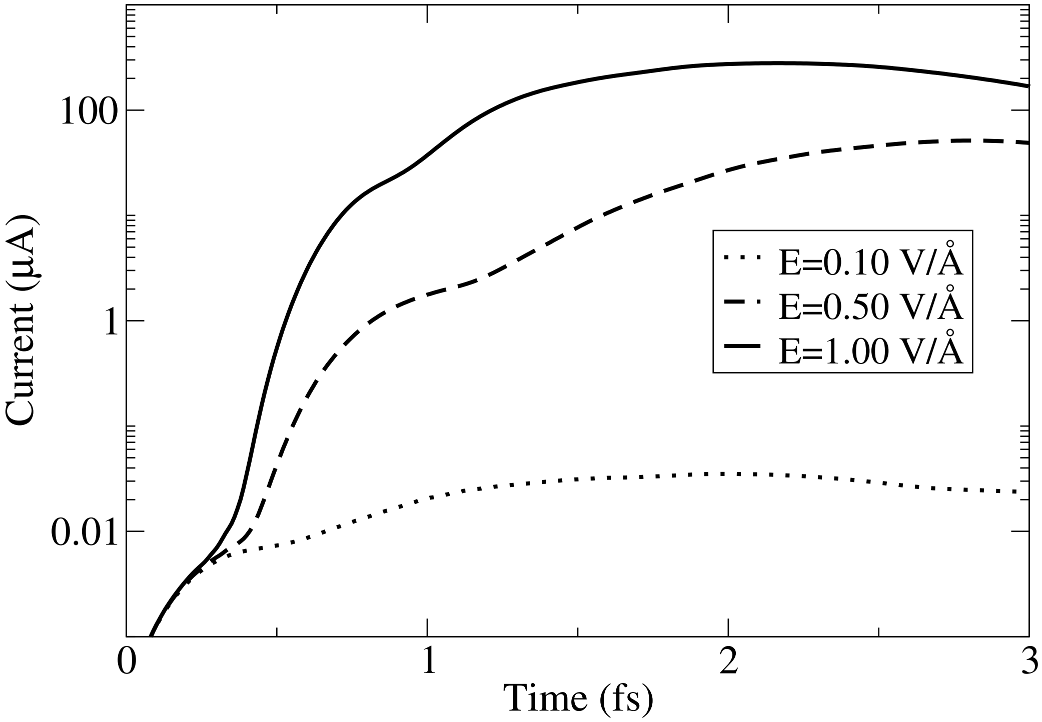

Figure V.55: Field emission current vs. time for a (3,3) hydrogen-terminated carbon nanotube. Curves for three different applied electric fields are shown.

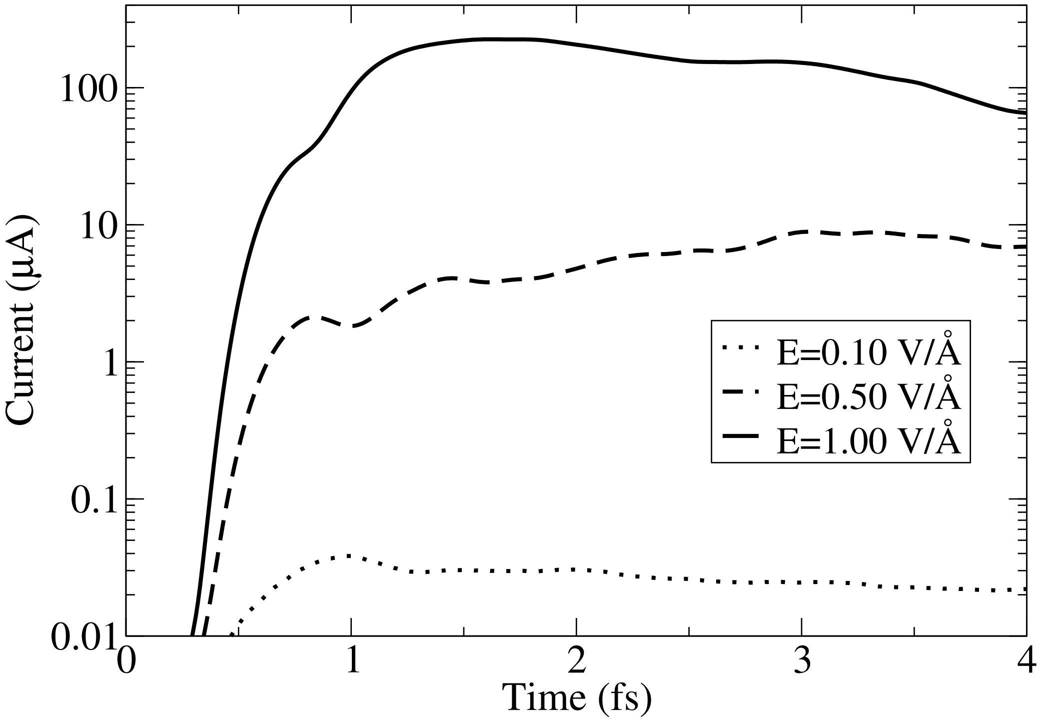

Figure V.56: Field emission current vs. time for a (3,3) graphene nanoribbon. Curves for three different applied electric fields are shown.

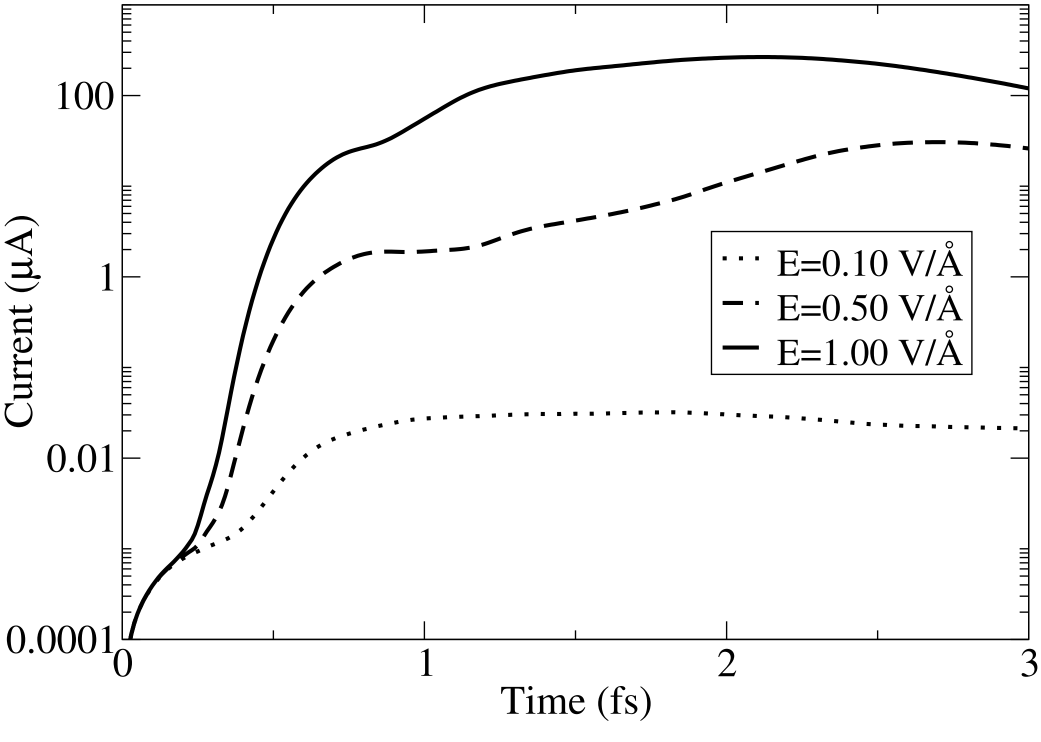

Figure V.57: Field emission current vs. time for a (3,3) carbon nanotube. Curves for three different applied electric fields are shown.

which to compare these results. Still, our results make interesting predictions of high currents (see below). In addition, this section serves as another example of the capabilities of our computational framework.

The currents increase by several orders of magnitude when increasing the applied electric field (notice that the plots use logarithmic scales for the vertical axes). This is a much greater response than with the nanotube results of previous sections. The time to reach a relatively stable current is also much shorter. These features suggest that these nanoribbons could be extremely good field emitters, and experiments are needed to further explore this.

CHAPTER VI

SUMMARY

The objective of this work was to study electron field emission from several nanostructures using a first-principles framework. The systems studied were carbon nanowires, graphene nanoribbons, and nanotubes of varying composition. These particular structures were chosen because they have recently been identified as showing novel physical phenomena, as well as having tremendous industrial applications. We examined the field emission under a variety of conditions, including laser illumination and the presence of adsorbates. The goal was to explore how these conditions affect the field emission performance.

In addition to the calculations, this dissertation has presented computational developments by the author that allowed these demanding calculations to be performed. There are many possible choices for basis when performing an electronic structure calculation. Examples are plane waves, atomic orbitals, and real-space grids. The best choice of basis depends on the structure of the system being analyzed and the physical processes involved (e.g., laser illumination). For this reason, it was important to conduct rigorous tests of basis set performance, in terms of accuracy and computational efficiency. There are no existing benchmark calculations for field emission, but transport calculations for nanostructures are similar, and so provide a useful reference for evaluating the performance of various basis sets. Based on the results, for the purposes of studying a non-periodic nanostructure under field emission conditions, we decided to use a real-space grid basis which incorporates the Lagrange function approach.

Once a basis was chosen, in this case a real-space grid, the issue of boundary conditions arose. The problem is that with a non-periodic system, field emitted electron density can experience non-physical reflections from the boundaries of the calculation volume, leading to inaccuracies. To prevent this issue, we used complex absorbing potentials (CAPs) to absorb electron density before it could reach the boundaries and reflect. The CAPs were zero in the region of the emitting structure and in regions were measurements were made. Still, we wanted to make sure that complex potentials were an accurate and efficient solution to the boundary problem. To evaluate this, we once again turned to benchmarks from transport calculations. The results showed CAPs to be an extremely accurate and efficient computational tool, and were incorporated into all of this dissertation's calculations.

Our calculations show that adsorbate atoms significantly increase the field emission current of carbon nanotubes. Adsorbate atoms also cause strong differences and nonlinearity in the Fowler-Nordheim plot. The source of the enhanced current is electronic states introduced by the adsorbate atom.

We have investigated the emission of electrons from nanostructures induced by short intense laser pulses in the presence of a weaker uniform static field. Based on the results of our simulations, two important qualitative features of this process have been determined: (1) a significant enhancement of the emission when a laser pulse is applied, and (2) the field emission current has a peak of some duration and the position of this peak correlates with the time of the pulse arrival. These two features suggest the possibility of using short laser pulses for making few-electron emitters of nanoscale size [212]. Such emitters could have many desirable properties, especially very high spatial and time resolutions.

The field emission from nanotubes of various composition has been studied. The calculations predict that the GaN, SiC, and Si nanotubes are particularly good field emitters. The highest-current nanotube, Si, is predicted to produce a current an order of magnitude higher than BN or C nanotubes.

The calculations predict that carbon nanotubes with various adsorbates can be used as spin-polarized current sources. These are the first first-principles calculations to show spin-polarized field emission for carbon nanotubes with iron adsorbates. Also, there is currently no experimental data with which to compare these results. However, the predicted strong spin-polarized field emission from these structures will hopefully spur experimental tests, potentially leading to applications within spintronics.

We also studied field emission from carbon nanowires and graphene nanoribbons. Since there is not yet any experimental work on field emission from isolated carbon nanowires or graphene nanoribbons, we cannot compare these results to experiment. These results are still useful in demonstrating the ability of our framework to study non-nanotube structures.

In addition, our nanoribbon results make interesting predictions of high currents. The currents increase by several orders of magnitude when increasing the applied electric field. This is a much greater response than with the nanotube results. The time to reach a relatively stable current is also much shorter. These features suggest that these nanoribbons could be extremely good field emitters, and experiments are needed to further explore this.

6.1 Comparison with experiment

There are experiments that have inspired our work, but for the most part the results presented in this dissertation represent predictions. In other words, there are few experiments with which the results can be directly compared. The problem is that the majority of experiments involve multiwall nanotubes. Due to the expense of our computations, we are restricted to single-wall tubes. There are experiments with single-wall nanotubes, but they usually involve collections of many tubes, and so again the experimental case differs from what we can presently compute. We hope that our results lead to experimental tests. This is already happening with nanotube field emission with adsorbates. Brau et al. [4] are experimenting with adding various adsorbates to nanotubes, and we are making predictions for which adsorbates to try.

As another example, there are experiments in which spin-polarized field emission is demonstrated for GaAs tips, Mn-doped BN nanotubes, etc. But not much for carbon. In fact, our calculations appear to be the first first-principles calculations of spin-polarized field emission from carbon nanotubes with adsorbed iron.

Cs atoms have been observed experimentally ([28, 29]) to increase field emission current magnitude, and our calculations also predict this. Kim et al. [28] used multiwall nanotubes and saw an order of magnitude increase. Wadhawan et al. [29] used bundles of many singlewall nanotubes and saw an increase of six orders of magnitude. Other experiments (such as Kim et al.) don't see six orders of magnitude, but it is important to note that the system under study differs. Regardless of the magnitude, both studies see enhancement, as do we in our calculations.

Another example of matching experimental results is Fowler-Nordheim plots. It is seen experimentally that field emission from carbon nanotubes is well-described by Fowler-Nordheim theory only for low fields. This deviation appears as nonlinear regions in a Fowler-Nordheim plot. Bonard et al. [2] show a sample experimental plot, and we see the same behavior in our calculations.

Some of our calculations compared the field emission performance of nanotubes made of different materials. We found that BN and C nanotubes are very similar in their current magnitudes, which was observed experimentally by Cumings et al. [255].

In the work of Hommelhoff et al. [199], laser pulses are applied to a field emitting tungsten tip to get short pulses of emitted electron density. We see the same effect in our calculations with nanotubes.

REFERENCES

[1] S. Waki, K. Hata, H. Sato, and Y. Saito. Behaviors of single nitrogen molecule on pentagon at carbon nanotube tip observed by field emission microscopy. *Journal of Vacuum Science & Technology B: Microelectronics and Nanometer Structures*, 25:517, 2007.

[2] J.M. Bonard, J.P. Salvetat, T. Stöckli, L. Forró, and A. Châtelain. Field emission from carbon nanotubes: perspectives for applications and clues to the emission mechanism. *Applied Physics A: Materials Science & Processing*, 69(3):245–254, 1999.

[3] M. Strange, I. S. Kristensen, K. S. Thygesen, and K. W. Jacobsen. Benchmark density functional theory calculations for nanoscale conductance. *J. Chem. Phys.*, 128(11):114714, 2008.

[4] J. D. Jarvis, H. L. Andrews, B. Ivanov, C. L. Stewart, N. de Jonge, E. C. Heeres, W.-P. Kang, Y.-M. Wong, J. L. Davidson, and C. A. Brau. Resonant tunneling and extreme brightness from diamond field emitters and carbon nanotubes. *Journal of Applied Physics*, 108(9):094322, 2010.

[5] J.D. Jarvis. Personal communication, 2011.

[6] Wulue Zhu and Guoliang Li. Structures and properties of small iron-doped carbon clusters. *International Journal of Mass Spectrometry*, 281(1-2):63 – 71, 2009.

[7] R.G. Parr and W. Yang. *Density-Functional Theory of Atoms and Molecules*. Oxford University Press, USA, 1989.

[8] W.A. de Heer, A. Châtelain, and D. Ugarte. A carbon nanotube field-emission electron source. *Science*, 270(5239):1179, 1995.

[9] OW Richardson. The Emission of Electrons from Tungsten at High Temperatures: An Experimental Proof That the Electric Current in Metals Is Carried by Electrons. *Science*, 38(967):57–61, 1913.

[10] HS Kim, ML Yu, MGR Thomson, E. Kratschmer, and THP Chang. Energy distributions of Zr/O/W Schottky electron emission. *Journal of Applied Physics*, 81:461, 1997.

[11] L. W. Swanson. Comparative study of the zirconiated and built-up w thermal-field cathode. *Journal of Vacuum Science and Technology*, 12(6):1228–1233, 1975.

[12] C. Hernandez Garcia and C. A. Brau. Pulsed photoelectric field emission from needle cathodes. *Nuclear Instruments and Methods in Physics Research Section A: Accelerators, Spectrometers, Detectors and Associated Equipment*, 483(1-2):273 – 276, 2002.

[13] WI Milne, KBK Teo, GAJ Amaratunga, P. Legagneux, L. Gangloff, J.P. Schnell, V. Semet, V.T. Binh, and O. Groening. Carbon nanotubes as field emission sources. *Journal of Materials Chemistry*, 14(6):933–943, 2004.

[14] K.B.K. Teo, E. Minoux, L. Hudanski, F. Peauger, J.P. Schnell, L. Gangloff, P. Legagneux, D. Dieumegard, G.A.J. Amaratunga, and W.I. Milne. Carbon nanotubes as cold cathodes. *Nature*, 437:968, 2005.

[15] N. de Jonge, Y. Lamy, K. Schoots, and T.H. Oosterkamp. High brightness electron beam from a multi-walled carbon nanotube. *Nature*, 420(6914):393–395, 2002.

[16] Y. Saito, K. Hamaguchi, K. Hata, K. Uchida, Y. Tasaka, F. Ikazaki, M. Yumura, A. Kasuya, and Y. Nishina. Conical beams from open nanotubes. *Nature*, 389(6651):554–554, 1997.

[17] WB Choi, DS Chung, JH Kang, HY Kim, YW Jin, IT Han, YH Lee, JE Jung, NS Lee, and GS Park. Fully sealed, high-brightness carbon-nanotube field-emission display. *Appl. Phys. Lett.*, 75:3129, 1999.

[18] AG Rinzler, JH Hafner, P. Nikolaev, P. Nordlander, DT Colbert, RE Smalley, L. Lou, SG Kim, and D. Tomanek. Unraveling nanotubes: field emission from an atomic wire. *Science*, 269(5230):1550–1553, 1995.

[19] Y. Saito and S. Uemura. Field emission from carbon nanotubes and its application to electron sources. *Carbon*, 38(2):169–182, 2000.

[20] Kenneth A. Dean and Babu R. Chalamala. Field emission microscopy of carbon nanotube caps. *J. Appl. Phys.*, 85(7):3832–3836, 1999.

[21] Heinz Schmid and Hans-Werner Fink. Carbon nanotubes are coherent electron sources. *Appl. Phys. Lett.*, 70(20):2679–2680, 1997.

[22] Y. Song, B. Usner, J. Choi, S.C. Lim, and Y.H. Lee. Field Emission Properties of Vertically Aligned Carbon Nanotubes Driven by Polar and Non-Polar Gas Adsorption. In *MATERIALS RESEARCH SOCIETY SYMPOSIUM PROCEEDINGS*, volume 706, pages 125–130. Warrendale, Pa.; Materials Research Society; 1999, 2001.

[23] Changkun Dong and Mool C. Gupta. Influences of the surface reactions on the field emission from multiwall carbon nanotubes. *Applied Physics Letters*, 83(1):159–161, 2003.

[24] Kenneth A. Dean, Paul von Allmen, and Babu R. Chalamala. Three behavioral states observed in field emission from single-walled carbon nanotubes. *Journal of Vacuum Science & Technology B: Microelectronics and Nanometer Structures*, 17(5):1959–1969, 1999.

[25] Kenneth A. Dean and Babu R. Chalamala. Current saturation mechanisms in carbon nanotube field emitters. *Applied Physics Letters*, 76(3):375–377, 2000.

[26] L. M. Sheng, P. Liu, Y. M. Liu, L. Qian, Y. S. Huang, L. Liu, and S. S. Fan. Effects of carbon-containing gases on the field-emission current of multiwalled carbon-nanotube arrays. volume 21, pages 1202–1204. AVS, 2003.

[27] Koichi Hata, Akihiro Takakura, and Yahachi Saito. Field emission from multiwall carbon nanotubes in controlled ambient gases, h2, co, n2 and o2. *Ultramicroscopy*, 95:107 – 112, 2003.

[28] Do-Hyung Kim, Hyeong-Rag Lee, Man-Woo Lee, Jin-Ho Lee, Yoon-Ho Song, Jong-Gi Jee, and Sang-Yun Lee. Effect of the in situ cs treatment on field emission of a multi-walled carbon nanotube. *Chemical Physics Letters*, 355(1-2):53 – 58, 2002.

[29] A. Wadhawan, R. E. Stallcup II, and J. M. Perez. Effects of cs deposition on the field-emission properties of single-walled carbon-nanotube bundles. *Applied Physics Letters*, 78(1):108–110, 2001.

[30] RH Fowler and L. Nordheim. Electron Emission in Intense Electric Fields. *Proceedings of the Royal Society of London. Series A*, 119(781):173–181, 1928.

[31] Xueping Xu and G. R. Brandes. A method for fabricating large-area, patterned, carbon nanotube field emitters. *Appl. Phys. Lett.*, 74(17):2549–2551, 1999.

[32] J.M. Bonard, J.P. Salvetat, T. Stöckli, W.A. de Heer, L. Forró, and A. Châtelain. Field emission from single-wall carbon nanotube films. *Appl. Phys. Lett.*, 73:918, 1998.

[33] K. L. Jensen. Exchange-correlation, dipole, and image charge potentials for electron sources: Temperature and field variation of the barrier height. *J. Appl. Phys.*, 85(5):2667–2680, 1999.

[34] N. D. Lang, A. Yacoby, and Y. Imry. Theory of a single-atom point source for electrons. *Phys. Rev. Lett.*, 63(14):1499–1502, 1989.

[35] Y. Gohda, Y. Nakamura, K. Watanabe, and S. Watanabe. Self-consistent density functional calculation of field emission currents from metals. *Phys. Rev. Lett.*, 85(8):1750–1753, 2000.

[36] Amitesh Maiti, Jan Andzelm, Noppawan Tanpipat, and Paul von Allmen. Effect of adsorbates on field emission from carbon nanotubes. *Phys. Rev. Lett.*, 87(15):155502, 2001.

[37] Seungwu Han, M. H. Lee, and Jisoon Ihm. Dynamical simulation of field emission in nanostructures. *Phys. Rev. B*, 65(8):085405, 2002.

[38] K. Tada and K. Watanabe. Ab initio study of field emission from graphitic ribbons. *Phys. Rev. Lett.*, 88(12):127601, 2002.

[39] A. Szabo and N.S. Ostlund. *Modern Quantum Chemistry: Introduction to Advanced Electronic Structure Theory.* Courier Dover Publications, 1996.

[40] J. C. Slater. The theory of complex spectra. *Phys. Rev.*, 34(10):1293–1322, Nov 1929.

[41] R.M. Martin. *Electronic structure: basic theory and practical methods.* Cambridge Univ Pr, 2004.

[42] C. David Sherrill and Henry F. Schaefer III. The configuration interaction method: Advances in highly correlated approaches. volume 34 of *Advances in Quantum Chemistry*, pages 143 – 269. Academic Press, 1999.

[43] Jiří Čížek. On the correlation problem in atomic and molecular systems. calculation of wavefunction components in ursell-type expansion using quantum-field theoretical methods. *The Journal of Chemical Physics*, 45(11):4256–4266, 1966.

[44] W. Koch, M.C. Holthausen, and M.C. Holthausen. *A chemist's guide to density functional theory*, volume 2. Wiley Online Library, 2001.

[45] P. Hohenberg and W. Kohn. Inhomogeneous electron gas. *Phys. Rev.*, 136(3B):B864–B871, Nov 1964.

[46] W. Kohn and L. J. Sham. Self-consistent equations including exchange and correlation effects. *Phys. Rev.*, 140(4A):A1133–A1138, Nov 1965.

[47] C. Fiolhais. A Primer in Density Functional Theory. *Materials Today*, 6(12):59–59, 2003.

[48] M. C. Payne, M. P. Teter, D. C. Allan, T. A. Arias, and J. D. Joannopoulos. Iterative minimization techniques for ab initio total-energy calculations: molecular dynamics and conjugate gradients. *Rev. Mod. Phys.*, 64(4):1045–1097, Oct 1992.

[49] Leonard Kleinman and D. M. Bylander. Efficacious form for model pseudopotentials. *Phys. Rev. Lett.*, 48(20):1425–1428, May 1982.

[50] P. H. Dederichs and R. Zeller. Self-consistency iterations in electronic-structure calculations. *Phys. Rev. B*, 28(10):5462–5472, Nov 1983.

[51] Erich Runge and E. K. U. Gross. Density-functional theory for time-dependent systems. *Phys. Rev. Lett.*, 52(12):997, Mar 1984.

[52] M. J. Stott and E. Zaremba. Linear-response theory within the density-functional formalism: Application to atomic polarizabilities. *Phys. Rev. A*, 21(1):12–23, Jan 1980.

[53] E. Runge and EKU Gross. Density-functional theory for time-dependent systems. *Phys. Rev. Lett.*, 52(12):997–1000, 1984.

[54] N. Troullier and José Luriaas Martins. Efficient pseudopotentials for plane-wave calculations. *Phys. Rev. B*, 43(3):1993–2006, 1991.

[55] E. K. U. Gross and Walter Kohn. Local density-functional theory of frequency-dependent linear response. *Phys. Rev. Lett.*, 55(26):2850–2852, 1985.

[56] A. Castro, M.A.L. Marques, and A. Rubio. Propagators for the time-dependent Kohn–Sham equations. *The Journal of chemical physics*, 121:3425, 2004.

[57] A. Askar and AS Cakmak. Explicit integration method for the time-dependent Schrödinger equation for collision problems. *The Journal of Chemical Physics*, 68:2794, 1978.

[58] Edward A. McCullough and Robert E. Wyatt. Quantum dynamics of the collinear (h, h_2) reaction. *The Journal of Chemical Physics*, 51(3):1253–1254, 1969.

[59] Klmn Varga and S. T. Pantelides. Lagrange-function approach to real-space order-n electronic-structure calculations. *physica status solidi (b)*, 243(5):1110–1120, 2006.

[60] R.G. Parr and W. Yang. *Density-Functional Theory of Atoms and Molecules.* Oxford University Press, USA, 1989.

[61] Aron J. Cohen, Paula Mori-Snchez, and Weitao Yang. Insights into current limitations of density functional theory. *Science*, 321(5890):792–794, 2008.

[62] W. Kohn, A. D. Becke, and R. G. Parr. Density functional theory of electronic structure. *The Journal of Physical Chemistry*, 100(31):12974–12980, 1996.

[63] J. P. Perdew and Alex Zunger. Self-interaction correction to density-functional approximations for many-electron systems. *Phys. Rev. B*, 23(10):5048–5079, May 1981.

[64] D. R. Hamann. h_2o hydrogen bonding in density-functional theory. *Phys. Rev. B*, 55(16):R10157–R10160, Apr 1997.

[65] Timothy J. Giese and Darrin M. York. Density-functional expansion methods: Evaluation of lda, gga, and meta-gga functionals and different integral approximations. *The Journal of Chemical Physics*, 133(24):244107, 2010.

[66] R. W. Godby and R. J. Needs. Metal-insulator transition in kohn-sham theory and quasiparticle theory. *Phys. Rev. Lett.*, 62(10):1169–1172, Mar 1989.

[67] Dirk Porezag and Mark R. Pederson. Infrared intensities and raman-scattering activities within density-functional theory. *Phys. Rev. B*, 54(11):7830–7836, Sep 1996.

[68] Mark R. Pederson, Koblar A. Jackson, and Warren E. Pickett. Local-density-approximation-based simulations of hydrocarbon interactions with applications to diamond chemical vapor deposition. *Phys. Rev. B*, 44(8):3891–3899, Aug 1991.

[69] Benny G. Johnson, Peter M. W. Gill, and John A. Pople. The performance of a family of density functional methods. *The Journal of Chemical Physics*, 98(7):5612–5626, 1993.

[70] K. Varga, Z. Zhang, and S.T. Pantelides. Lagrange functions: A family of powerful basis sets for real-space order-n electronic structure calculations. *Phys. Rev. Lett.*, 93(17):176403, 2004.

[71] Volker Blum, Ralf Gehrke, Felix Hanke, Paula Havu, Ville Havu, Xinguo Ren, Karsten Reuter, and Matthias Scheffler. Ab initio molecular simulations with numeric atom-centered orbitals. *Computer Physics Communications*, 180(11):2175 – 2196, 2009.

[72] B. Delley. From molecules to solids with the dmol^3 approach. *The Journal of Chemical Physics*, 113(18):7756–7764, 2000.

[73] Javier Junquera, Óscar Paz, Daniel Sánchez-Portal, and Emilio Artacho. Numerical atomic orbitals for linear-scaling calculations. *Phys. Rev. B*, 64(23):235111, Nov 2001.

[74] T. Ozaki and H. Kino. Numerical atomic basis orbitals from h to kr. *Phys. Rev. B*, 69(19):195113, May 2004.

[75] James R. Chelikowsky and Steven G. Louie. First-principles linear combination of atomic orbitals method for the cohesive and structural properties of solids: Application to diamond. *Phys. Rev. B*, 29(6):3470–3481, Mar 1984.

[76] David Vanderbilt and Steven G. Louie. Total energies of diamond (111) surface reconstructions by a linear combination of atomic orbitals method. *Phys. Rev. B*, 30(10):6118–6130, Nov 1984.

[77] Robert W. Jansen and Otto F. Sankey. Ab initio linear combination of pseudo-atomic-orbital scheme for the electronic properties of semiconductors: Results for ten materials. *Phys. Rev. B*, 36(12):6520–6531, Oct 1987.

[78] W. J. Hehre, R. F. Stewart, and J. A. Pople. Self-consistent molecular-orbital methods. i. use of gaussian expansions of slater-type atomic orbitals. *The Journal of Chemical Physics*, 51(6):2657–2664, 1969.

[79] John A. Pople, Martin Head-Gordon, Douglas J. Fox, Krishnan Raghavachari, and Larry A. Curtiss. Gaussian-1 theory: A general procedure for prediction of molecular energies. *The Journal of Chemical Physics*, 90(10):5622–5629, 1989.

[80] Jr. Thom H. Dunning. Gaussian basis sets for use in correlated molecular calculations. i. the atoms boron through neon and hydrogen. *The Journal of Chemical Physics*, 90(2):1007–1023, 1989.

[81] Pablo Ordejón, Emilio Artacho, and José M. Soler. Self-consistent order-n density-functional calculations for very large systems. *Phys. Rev. B*, 53(16):R10441–R10444, Apr 1996.

[82] Francesco Mauri and Giulia Galli. Electronic-structure calculations and molecular-dynamics simulations with linear system-size scaling. *Phys. Rev. B*, 50(7):4316–4326, Aug 1994.

[83] X.-P. Li, R. W. Nunes, and David Vanderbilt. Density-matrix electronic-structure method with linear system-size scaling. *Phys. Rev. B*, 47(16):10891–10894, Apr 1993.

[84] Stefan Goedecker. Linear scaling electronic structure methods. *Rev. Mod. Phys.*, 71(4):1085–1123, Jul 1999.

[85] Gabor Szego. *Orthogonal polynomials.* American Mathematical Society, 4th ed. edition, 1939.

[86] Gene H. Golub and John H. Welsch. Calculation of Gauss quadrature rules. *Math. Comp. 23 (1969), 221-230; addendum, ibid.*, 23(106, loose microfiche suppl):A1–A10, 1969.

[87] Viktor Szalay. The generalized discrete variable representation. an optimal design. *The Journal of Chemical Physics*, 105(16):6940–6956, 1996.

[88] D. Baye and P-H. Heenen. Generalised meshes for quantum mechanical problems. *Journal of Physics A: Mathematical and General*, 19(11):2041–2059, 1986.

[89] D. Baye and M. Vincke. Lagrange meshes from nonclassical orthogonal polynomials. *Phys. Rev. E*, 59(6):7195–7199, Jun 1999.

[90] J.P. Boyd. *Chebyshev and Fourier Spectral Methods.* Dover Publications, 2nd revised ed. edition, 2001.

[91] James T. Muckerman. Some useful discrete variable representations for problems in time-dependent and time-independent quantum mechanics. *Chemical Physics Letters*, 173(2-3):200 – 205, 1990.

[92] Kálmán Varga, Zhenyu Zhang, and Sokrates T. Pantelides. ılagrange functionsȷ: A family of powerful basis sets for real-space order-n electronic structure calculations. *Phys. Rev. Lett.*, 93(17):176403, Oct 2004.

[93] K. Varga. Multidomain decomposition in electronic structure calculations. *Phys. Rev. B*, in press, 2009.

[94] Takeo Hoshi, Masao Arai, and Takeo Fujiwara. Density-functional molecular dynamics with real-space finite difference. *Phys. Rev. B*, 52(8):R5459–R5462, Aug 1995.

[95] E. L. Briggs, D. J. Sullivan, and J. Bernholc. Real-space multigrid-based approach to large-scale electronic structure calculations. *Phys. Rev. B*, 54(20):14362–14375, Nov 1996.

[96] Thomas L. Beck. Real-space mesh techniques in density-functional theory. *Rev. Mod. Phys.*, 72(4):1041–1080, Oct 2000.

[97] M. Heiskanen, T. Torsti, M. J. Puska, and R. M. Nieminen. Multigrid method for electronic structure calculations. *Phys. Rev. B*, 63(24):245106, Jun 2001.

[98] James R. Chelikowsky, N. Troullier, K. Wu, and Y. Saad. Higher-order finite-difference pseudopotential method: An application to diatomic molecules. *Phys. Rev. B*, 50(16):11355–11364, Oct 1994.

[99] S. Datta. *Electronic transport in mesoscopic systems.* Cambridge University Press, 1997.

[100] Sergey V. Faleev, Fran çois Léonard, Derek A. Stewart, and Mark van Schilfgaarde. Ab initio tight-binding lmto method for nonequilibrium electron transport in nanosystems. *Phys. Rev. B*, 71(19):195422, May 2005.

[101] J. J. Palacios, A. J. Pérez-Jiménez, E. Louis, E. SanFabián, and J. A. Vergés. First-principles phase-coherent transport in metallic nanotubes with realistic contacts. *Phys. Rev. Lett.*, 90(10):106801, Mar 2003.

[102] K. Stokbro, J. Taylor, M. Brandbyge, J. L. Mozos, and P. Ordejn. Theoretical study of the nonlinear conductance of di-thiol benzene coupled to au(111) surfaces via thiol and thiolate bonds. *Computational Materials Science*, 27(1-2):151 – 160, 2003.

[103] San-Huang Ke, Harold U. Baranger, and Weitao Yang. Electron transport through molecules: Self-consistent and non-self-consistent approaches. *Phys. Rev. B*, 70(8):085410, Aug 2004.

[104] Eldon G. Emberly and George Kirczenow. Models of electron transport through organic molecular monolayers self-assembled on nanoscale metallic contacts. *Phys. Rev. B*, 64(23):235412, Nov 2001.

[105] Jeremy Taylor, Hong Guo, and Jian Wang. Ab initio modeling of quantum transport properties of molecular electronic devices. *Phys. Rev. B*, 63(24):245407, Jun 2001.

[106] Marco Buongiorno Nardelli, J.-L. Fattebert, and J. Bernholc. $o(n)$ real-space method for ab initio quantum transport calculations: Application to carbon nanotube˘metal contacts. *Phys. Rev. B*, 64(24):245423, Dec 2001.

[107] Yongqiang Xue, Supriyo Datta, and Mark A. Ratner. Charge transfer and "band lineup" in molecular electronic devices: A chemical and numerical interpretation. *J. Chem. Phys.*, 115(9):4292–4299, 2001.

[108] K.S. Thygesen and K.W. Jacobsen. Molecular transport calculations with wannier functions. *Chemical Physics*, 319(1-3):111 – 125, 2005.

[109] P.A. Derosa and J.M. Seminario. Electron transport through single molecules: Scattering treatment using density functional and green function theories. *J. Phys. Chem. B*, 105(2):471–481, 2001.

[110] X. Zhang, L. Fonseca, and AA Demkov. The application of density functional, local orbitals, and scattering theory to quantum transport. *Physica Status Solidi B*, 233(1):70–82, 2002.

[111] S. Sanvito, C. J. Lambert, J. H. Jefferson, and A. M. Bratkovsky. General green's-function formalism for transport calculations with *spd* hamiltonians and giant magnetoresistance in co- and ni-based magnetic multilayers. *Phys. Rev. B*, 59(18):11936–11948, May 1999.

[112] A. Garcia-Lekue and L.W. Wang. Self-consistent non-equilibrium transport using plane waves. *Computational Materials Science*, 45(4):1016 – 1024, 2009.

[113] Charles W. Bauschlicher, Jr., John W. Lawson, Alessandra Ricca, Yongqiang Xue, and Mark A. Ratner. Current-voltage curves for molecular junctions: the effect of cl substituents and basis set composition. *Chemical Physics Letters*, 388(4-6):427 – 429, 2004.

[114] Michele Gusso. Study on the maximum accuracy of the pseudopotential density functional method with localized atomic orbitals versus plane-wave basis sets. *J. Chem. Phys.*, 128(4):044102, 2008.

[115] J. S. Nelson, E. B. Stechel, A. F. Wright, S. J. Plimpton, P. A. Schultz, and M. P. Sears. Basis-set convergence of highly defected sites in amorphous carbon. *Phys. Rev. B*, 52(13):9354–9359, Oct 1995.

[116] M P López Sancho, J M López Sancho, and J Rubio. Highly convergent schemes for the calculation of bulk and surface green functions. *Journal of Physics F: Metal Physics*, 15(4):851, 1985.

[117] J. A. Driscoll and K. Varga. Convergence in quantum transport calculations: Localized atomic orbitals versus nonlocalized basis sets. *Phys. Rev. B*, 81(11):115412, Mar 2010.

[118] W.H. Miller. Beyond Transition-State Theory: A Rigorous Quantum Theory of Chemical Reaction Rates. *Accounts of Chemical Research*, 26(4):174–181, 1993.

[119] D.K. Hoffman, Y. Huang, W. Zhu, and D.J. Kouri. Further analysis of solutions to the time-independent wave packet equations for quantum dynamics: General initial wave packets. *The Journal of Chemical Physics*, 101:1242, 1994.

[120] T. Seideman and W.H. Miller. Quantum mechanical reaction probabilities via a discrete variable representation-absorbing boundary condition Greens function. *The Journal of Chemical Physics*, 97(4):2499, 1992.

[121] P.E. Hodgson. *The optical model of elastic scattering*. Clarendon Press, 1963.

[122] H.C. Baker. Non-Hermitian Dynamics of Multiphoton Ionization. *Physical Review Letters*, 50(20):1579–1582, 1983.

[123] Thomas Gramespacher and Markus Büttiker. Distribution functions and current-current correlations in normal-metal–superconductor heterostructures. *Phys. Rev. B*, 61(12):8125–8132, Mar 2000.

[124] M. Büttiker, H. Thomas, and A. Prêtre. Current partition in multiprobe conductors in the presence of slowly oscillating external potentials. *Zeitschrift für Physik B Condensed Matter*, 94(1):133–137, 1994.

[125] MS Child. Analysis of a complex absorbing barrier. *Molecular physics*, 72(1):89–93, 1991.

[126] Tamar Seideman and William H. Miller. Calculation of the cumulative reaction probability via a discrete variable representation with absorbing boundary conditions. *The Journal of Chemical Physics*, 96(6):4412–4422, 1992.

[127] Á. Vibók and GG Balint-Kurti. Parametrization of complex absorbing potentials for time-dependent quantum dynamics. *The Journal of Physical Chemistry*, 96(22):8712–8719, 1992.

[128] S. Brouard, D. Macias, and JG Muga. Perfect absorbers for stationary and wavepacket scattering. *Journal of Physics A: Mathematical and General*, 27:L439–L445, 1994.

[129] J.G. Muga, J.P. Palao, B. Navarro, and I.L. Egusquiza. Complex absorbing potentials. *Physics Reports*, 395(6):357 – 426, 2004.

[130] Georges Jolicard and Jeannette Humbert. Study of the one-channel resonance states. method without a stabilization procedure in the framework of the optical potential model. *Chemical Physics*, 118(3):397 – 405, 1987.

[131] David E. Manolopoulos. Derivation and reflection properties of a transmission-free absorbing potential. *J. Chem. Phys.*, 117(21):9552–9559, 2002.

[132] M. Büttiker, Y. Imry, R. Landauer, and S. Pinhas. Generalized many-channel conductance formula with application to small rings. *Phys. Rev. B*, 31(10):6207–6215, May 1985.

[133] M. Di Ventra, S. T. Pantelides, and N. D. Lang. First-principles calculation of transport properties of a molecular device. *Phys. Rev. Lett.*, 84(5):979–982, Jan 2000.

[134] Petr A. Khomyakov and Geert Brocks. Real-space finite-difference method for conductance calculations. *Phys. Rev. B*, 70(19):195402, Nov 2004.

[135] Julian Velev and William Butler. On the equivalence of different techniques for evaluating the green function for a semi-infinite system using a localized basis. *Journal of Physics: Condensed Matter*, 16(21):R637, 2004.

[136] T. Ando. Quantum point contacts in magnetic fields. *Phys. Rev. B*, 44(15):8017–8027, Oct 1991.

[137] P. S. Krstić, X.-G. Zhang, and W. H. Butler. Generalized conductance formula for the multiband tight-binding model. *Phys. Rev. B*, 66(20):205319, Nov 2002.

[138] Thomas M. Henderson, Giorgos Fagas, Eoin Hyde, and James C. Greer. Determination of complex absorbing potentials from the electron self-energy. *The Journal of Chemical Physics*, 125(24):244104, 2006.

[139] Mads Brandbyge, José-Luis Mozos, Pablo Ordejón, Jeremy Taylor, and Kurt Stokbro. Density-functional method for nonequilibrium electron transport. *Phys. Rev. B*, 65(16):165401, Mar 2002.

[140] N. D. Lang and Ph. Avouris. Carbon-atom wires: Charge-transfer doping, voltage drop, and the effect of distortions. *Phys. Rev. Lett.*, 84(2):358–361, Jan 2000.

[141] Brian Larade, Jeremy Taylor, H. Mehrez, and Hong Guo. Conductance, $i - v$ curves, and negative differential resistance of carbon atomic wires. *Phys. Rev. B*, 64(7):075420, Jul 2001.

[142] J. C. Slater and G. F. Koster. Simplified lcao method for the periodic potential problem. *Phys. Rev.*, 94(6):1498–1524, Jun 1954.

[143] J. C. Charlier, Ph. Lambin, and T. W. Ebbesen. Electronic properties of carbon nanotubes with polygonized cross sections. *Phys. Rev. B*, 54(12):R8377–R8380, Sep 1996.

[144] A. Einstein. Über einen die Erzeugung und Verwandlung des Lichtes betreffenden heuristischen Gesichtspunkt. *Annalen der Physik*, 17:132–148, 1905.

[145] Conyers Herring and M. H. Nichols. Thermionic emission. *Rev. Mod. Phys.*, 21(2):185–270, Apr 1949.

[146] F. Ducastelle, X. Blase, J.-M. Bonard, J.-Ch. Charlier, and P. Petit. Electronic structure. In Annick Loiseau, Pascale Launois, Pierre Petit, Stephan Roche, and Jean-Paul Salvetat, editors, *Understanding Carbon Nanotubes*, volume 677 of *Lecture Notes in Physics*, pages 199–276. Springer Berlin / Heidelberg, 2006.

[147] L. W. Nordheim. The Effect of the Image Force on the Emission and Reflexion of Electrons by Metals. *Proceedings of the Royal Society of London. Series A*, 121(788):626–639, 1928.

[148] Jean-Marc Bonard, Kenneth A. Dean, Bernard F. Coll, and Christian Klinke. Field emission of individual carbon nanotubes in the scanning electron microscope. *Phys. Rev. Lett.*, 89(19):197602, Oct 2002.

[149] Y. Saito, K. Hamaguchi, T. Nishino, K. Hata, K. Tohji, A. Kasuya, and Y. Nishina. Field emission patterns from single-walled carbon nanotubes. *Japanese journal of applied physics*, 36(10A):L1340–L1342, 1997.

[150] Y. Chen, S. Z. Deng, N. S. Xu, J. Chen, X. C. Ma, and E. G. Wang. Physical origin of non-linearity in fowler-nordheim plots of aligned large area multi-walled nitrogen-containing carbon nanotubes. *Materials Science and Engineering A*, 327(1):16 – 19, 2002.

[151] Jean-Marc Bonard, Jean-Paul Salvetat, Thomas Stöckli, Walt A. de Heer, László Forró, and André Châtelain. Field emission from single-wall carbon nanotube films. *Applied Physics Letters*, 73(7):918–920, 1998.

[152] J. P. Barbour, W. W. Dolan, J. K. Trolan, E. E. Martin, and W. P. Dyke. Space-charge effects in field emission. *Phys. Rev.*, 92(1):45–51, Oct 1953.

[153] B. Ricco and M. Ya. Azbel. Physics of resonant tunneling. the one-dimensional double-barrier case. *Phys. Rev. B*, 29(4):1970–1981, Feb 1984.

[154] A. Mayer, NM Miskovsky, and PH Cutler. Transfer-matrix simulations of field emission from a metallic (5, 5) carbon nanotube. *Ultramicroscopy*, 92(3-4):215–220, 2002.

[155] H. Ishida, D. Wortmann, and T. Ohwaki. First-principles calculations of tunneling conductance. *Phys. Rev. B*, 70(8):085409, Aug 2004.

[156] Stephan Roche, Fran çois Triozon, Angel Rubio, and Didier Mayou. Conduction mechanisms and magnetotransport in multiwalled carbon nanotubes. *Phys. Rev. B*, 64(12):121401, Sep 2001.

[157] D.J. Griffiths. *Introduction to electrodynamics*. Benjamin Cummings, 3 edition, 1999.

[158] Richard G. Forbes. Field-induced electron emission from electrically nanostructured heterogeneous (enh) materials. *Ultramicroscopy*, 89(1-3):7 – 15, 2001.

[159] Richard G. Forbes, C. J. Edgcombe, and U. Valdr. Some comments on models for field enhancement. *Ultramicroscopy*, 95:57 – 65, 2003.

[160] TE Stern, BS Gossling, and RH Fowler. Further studies in the emission of electrons from cold metals. *Proceedings of the Royal Society of London. Series A, Containing Papers of a Mathematical and Physical Character*, 124(795):699–723, 1929.

[161] M. Wang, Z. H. Li, X. F. Shang, X. Q. Wang, and Y. B. Xu. Field-enhancement factor for carbon nanotube array. *Journal of Applied Physics*, 98(1):014315, 2005.

[162] R. C. Smith and S. R. P. Silva. Interpretation of the field enhancement factor for electron emission from carbon nanotubes. *Journal of Applied Physics*, 106(1):014314, 2009.

[163] X. Q. Wang, M. Wang, P. M. He, Y. B. Xu, and Z. H. Li. Model calculation for the field enhancement factor of carbon nanotube. *Journal of Applied Physics*, 96(11):6752–6755, 2004.

[164] R. C. Smith, R. D. Forrest, J. D. Carey, W. K. Hsu, and S. R. P. Silva. Interpretation of enhancement factor in nonplanar field emitters. *Applied Physics Letters*, 87(1):013111, 2005.

[165] F.A.M. Koeck, M. Zumer, V. Nemanic, and R.J. Nemanich. Photo and field electron emission microscopy, from sulfur doped nanocrystalline diamond films. *Diamond and Related Materials*, 15(4-8):880 – 883, 2006. Diamond 2005.

[166] E. A. Deulin, V. P. Mikhailov, Yu V. Panfilov, R. A. Nevshupa, E. A. Deulin, V. P. Mikhailov, Yu. V. Panfilov, and R. A. Nevshupa. Using precise mechanisms in modern vacuum technological equipment. In R. Moreau Madylam, editor, *Mechanics and Physics of Precise Vacuum Mechanisms*, volume 91 of *Fluid Mechanics and its Applications*, pages 1–19. Springer Netherlands, 2010.

[167] K. Hata, A. Takakura, and Y. Saito. Field emission microscopy of adsorption and desorption of residual gas molecules on a carbon nanotube tip. *Surf. Sci*, 490:296–300, 2001.

[168] J. A. Driscoll and K. Varga. Time-dependent density-functional study of field emission from tipped carbon nanotubes. *Phys. Rev. B*, 80(24):245431, 2009.

[169] R. Saito, G. Dresselhaus, and MS Dresselhaus. PHYSICAL PROPERTIES OF CARBON NANOTUBES. *Carbon*, 33(7):883–891, 1995.

[170] T.W. Odom, J.L. Huang, P. Kim, and C.M. Lieber. Atomic structure and electronic properties of single-walled carbon nanotubes. *Nature*, 391(6662):62–64, 1998.

[171] Rodney Andrews, David Jacques, Dali Qian, and Terry Rantell. Multiwall carbon nanotubes: synthesis and application. *Accounts of Chemical Research*, 35(12):1008–1017, 2002. PMID: 12484788.

[172] A. G. Rinzler, J. H. Hafner, P. Nikolaev, L. Lou, S. G. Kim, D. Tomnek, P. Nordlander, D. T. Colbert, and R. E. Smalley. Unraveling nanotubes: Field emission from an atomic wire. *Science*, 269(5230):1550–1553, 1995.

[173] G. Gao, T. Çagin, and A.G. William III. Energetics, structure, mechanical and vibrational properties of single-walled carbon nanotubes. *Nanotechnology*, 9:184, 1998.

[174] R.S. Ruoff, D. Qian, and W.K. Liu. Mechanical properties of carbon nanotubes: theoretical predictions and experimental measurements. *Comptes Rendus Physique*, 4(9):993–1008, 2003.

[175] Andreas Thess, Roland Lee, Pavel Nikolaev, Hongjie Dai, Pierre Petit, Jerome Robert, Chunhui Xu, Young Hee Lee, Seong Gon Kim, Andrew G. Rinzler, Daniel T. Colbert, Gustavo E. Scuseria, David Tomnek, John E. Fischer, and Richard E. Smalley. Crystalline Ropes of Metallic Carbon Nanotubes. *Science*, 273(5274):483–487, 1996.

[176] S. Berber, Y.K. Kwon, and D. Tomanek. Unusually high thermal conductivity of carbon nanotubes. *Physical Review Letters*, 84(20):4613–4616, 2000.

[177] J. Hone, M. Whitney, C. Piskoti, and A. Zettl. Thermal conductivity of single-walled carbon nanotubes. *Physical Review B*, 59(4):2514–2516, 1999.

[178] ER Margine, M.L. Bocquet, and X. Blase. Thermal stability of graphene and nanotube covalent functionalization. *Nano letters*, 8(10):3315–3319, 2008.

[179] QH Wang, AA Setlur, JM Lauerhaas, JY Dai, EW Seelig, and RPH Chang. A nanotube-based field-emission flat panel display. *Applied Physics Letters*, 72:2912, 1998.

[180] Q. H. Wang, M. Yan, and R. P. H. Chang. Flat panel display prototype using gated carbon nanotube field emitters. *Appl. Phys. Lett.*, 78(9):1294–1296, 2001.

[181] Jean-Marc Bonard, Thomas Stöckli, Olivier Noury, and André Châtelain. Field emission from cylindrical carbon nanotube cathodes: Possibilities for luminescent tubes. *Appl. Phys. Lett.*, 78(18):2775–2777, 2001.

[182] Matthieu Mauger and Vu Thien Binh. Vertically aligned carbon nanotube arrays for giant field emission displays. *J. Vac. Sci. Technol. B*, 24(2):997–1003, 2006.

[183] Nasreen G. Chopra, R. J. Luyken, K. Cherrey, Vincent H. Crespi, Marvin L. Cohen, Steven G. Louie, and A. Zettl. Boron nitride nanotubes. *Science*, 269(5226):pp. 966–967, 1995.

[184] Xu-Hui Sun, Chi-Pui Li, Wing-Kwong Wong, Ning-Bew Wong, Chun-Sing Lee, Shuit-Tong Lee, and Boon-Keng Teo. Formation of silicon carbide nanotubes and nanowires via reaction of silicon (from disproportionation of silicon monoxide) with carbon nanotubes. *J. Am. Chem. Soc.*, 124(48):14464–14471, 2002.

[185] J. Sha, J. Niu, X. Ma, J. Xu, X. Zhang, Q. Yang, and D. Yang. Silicon nanotubes. *Advanced Materials*, 14(17):1219–1221, 2002.

[186] J. Goldberger, R. He, Y. Zhang, S. Lee, H. Yan, H.J. Choi, and P. Yang. Single-crystal gallium nitride nanotubes. *Nature*, 422(6932):599–602, 2003.

[187] G. Kresse and J. Furthmüller. Efficient iterative schemes for ab initio total-energy calculations using a plane-wave basis set. *Phys. Rev. B*, 54(16):11169–11186, Oct 1996.

[188] E. Durgun, S. Dag, S. Ciraci, and O. Glseren. Energetics and electronic structures of individual atoms adsorbed on carbon nanotubes. *The Journal of Physical Chemistry B*, 108(2):575–582, 2004.

[189] Mohammad Khazaei and Yoshiyuki Kawazoe. Effects of cs treatment on field emission properties of capped carbon nanotubes. *Surface Science*, 601(6):1501 – 1506, 2007.

[190] S. Lazar, C. Hbert, and H. W. Zandbergen. Investigation of hexagonal and cubic gan by high-resolution electron energy-loss spectroscopy and density functional theory. *Ultramicroscopy*, 98(2-4):249 – 257, 2004. Festschrift in Honor of the 70th Birthday of Professor Fang-Hua Li.

[191] L. F. J. Piper, Alex DeMasi, Kevin E. Smith, A. Schleife, F. Fuchs, F. Bechstedt, J. Zuniga-Pérez, and V. Munoz-Sanjosé. Electronic structure of single-crystal rocksalt cdo studied by soft x-ray spectroscopies and ab initio calculations. *Phys. Rev. B*, 77(12):125204, Mar 2008.

[192] S.W. Kortboyer, J.B. Goedkoop, F.M.F. De Groot, M. Grioni, J.C. Fuggle, and H. Petersen. Experimental resolution in soft x-ray monochromators. *Nuclear Instruments and Methods in Physics Research Section A: Accelerators, Spectrometers, Detectors and Associated Equipment*, 275(2):435 – 441, 1989.

[193] M. J. Fransen, Th. L. van Rooy, and P. Kruit. Field emission energy distributions from individual multiwalled carbon nanotubes. *Applied Surface Science*, 146(1-4):312 – 327, 1999.

[194] Ch. Adessi and M. Devel. Theoretical study of field emission by single-wall carbon nanotubes. *Phys. Rev. B*, 62(20):R13314–R13317, Nov 2000.

[195] D. Y. Zhong, G. Y. Zhang, S. Liu, T. Sakurai, and E. G. Wang. Universal field-emission model for carbon nanotubes on a metal tip. *Applied Physics Letters*, 80(3):506–508, 2002.

[196] Q. H. Wang, T. D. Corrigan, J. Y. Dai, R. P. H. Chang, and A. R. Krauss. Field emission from nanotube bundle emitters at low fields. *Applied Physics Letters*, 70(24):3308–3310, 1997.

[197] L. H. Chan, K. H. Hong, D. Q. Xiao, W. J. Hsieh, S. H. Lai, H. C. Shih, T. C. Lin, F. S. Shieu, K. J. Chen, and H. C. Cheng. Role of extrinsic atoms on the morphology and field emission properties of carbon nanotubes. *Applied Physics Letters*, 82(24):4334–4336, 2003.

[198] Philip G. Collins and A. Zettl. Unique characteristics of cold cathode carbon-nanotube-matrix field emitters. *Phys. Rev. B*, 55(15):9391–9399, Apr 1997.

[199] Peter Hommelhoff, Catherine Kealhofer, and Mark A. Kasevich. Ultrafast electron pulses from a tungsten tip triggered by low-power femtosecond laser pulses. *Phys. Rev. Lett.*, 97(24):247402, Dec 2006.

[200] Peter Hommelhoff, Yvan Sortais, Anoush Aghajani-Talesh, and Mark A. Kasevich. Field emission tip as a nanometer source of free electron femtosecond pulses. *Phys. Rev. Lett.*, 96(7):077401, Feb 2006.

[201] Hirofumi Yanagisawa, Christian Hafner, Patrick Doná, Martin Klöckner, Dominik Leuenberger, Thomas Greber, Matthias Hengsberger, and Jürg Osterwalder. Optical control of field-emission sites by femtosecond laser pulses. *Phys. Rev. Lett.*, 103(25):257603, Dec 2009.

[202] Wayne E. King, Geoffrey H. Campbell, Alan Frank, Bryan Reed, John F. Schmerge, Bradley J. Siwick, Brent C. Stuart, and Peter M. Weber. Ultrafast electron microscopy in materials science, biology, and chemistry. *J. Appl. Phys.*, 97(11):111101, 2005.

[203] C. A. Brau. High-brightness electron beams - small free-electron lasers. *Nucl. Instr. and Meth. A*, 407(1-3):1 – 7, 1998.

[204] Stefan Grafström. Photoassisted scanning tunneling microscopy. *J. Appl. Phys.*, 91(4):1717–1753, 2002.

[205] T Otobe, K Yabana, and J-I Iwata. First-principles calculation of the electron dynamics in crystalline sio 2. *Journal of Physics: Condensed Matter*, 21(6):064224, 2009.

[206] E. Gross, J. Dobson, and M. Petersilka. Density functional theory of time-dependent phenomena. In R. Nalewajski, editor, *Density Functional Theory II*, volume 181 of *Topics in Current Chemistry*, pages 81–172. Springer Berlin / Heidelberg, 1996. 10.1007/BFb0016643.

[207] T. Otobe and K. Yabana. Density-functional calculation for the tunnel ionization rate of hydrocarbon molecules. *Phys. Rev. A*, 75(6):062507, Jun 2007.

[208] M. Lein, E. K. U. Gross, and V. Engel. Discrete peaks in above-threshold double-ionization spectra. *Phys. Rev. A*, 64(2):023406, Jul 2001.

[209] W. Demtr
"oder. *Atoms, molecules and photons: an introduction to atomic-, molecular-, and quantum-physics.* Springer Verlag, 2006.

[210] P. Ehrenfest. Bemerkung ber die angenherte gltigkeit der klassischen mechanik innerhalb der quantenmechanik. *Zeitschrift fr Physik A Hadrons and Nuclei*, 45:455–457, 1927. 10.1007/BF01329203.

[211] Loup Verlet. Computer "experiments" on classical fluids. i. thermodynamical properties of lennard-jones molecules. *Phys. Rev.*, 159(1):98, Jul 1967.

[212] H. Niikura, F. Legare, R. Hasbani, AD Bandrauk, M.Y. Ivanov, DM Villeneuve, and PB Corkum. Sub-laser-cycle electron pulses for probing molecular dynamics. *Nature*, 417(6892):917–922, 2002.

[213] Paola Ayala, Raul Arenal, Annick Loiseau, Angel Rubio, and Thomas Pichler. The physical and chemical properties of heteronanotubes. *Rev. Mod. Phys.*, 82(2):1843–1885, Jun 2010.

[214] X. Blase, A. De Vita, J.-C. Charlier, and R. Car. Frustration effects and microscopic growth mechanisms for bn nanotubes. *Phys. Rev. Lett.*, 80(8):1666–1669, Feb 1998.

[215] Yongfeng Zhang and Hanchen Huang. Stability of single-wall silicon carbide nanotubes - molecular dynamics simulations. *Computational Materials Science*, 43(4):664 – 669, 2008.

[216] J. E. Bunder and James M. Hill. Electronic properties of silicon nanotubes with distinct bond lengths. *Phys. Rev. B*, 79(23):233401, Jun 2009.

[217] J. Tersoff. New empirical approach for the structure and energy of covalent systems. *Phys. Rev. B*, 37(12):6991–7000, 1988.

[218] J. Tersoff. Empirical interatomic potential for carbon, with applications to amorphous carbon. *Phys. Rev. Lett.*, 61(25):2879–2882, 1988.

[219] L. Lindsay and D. A. Broido. Optimized tersoff and brenner empirical potential parameters for lattice dynamics and phonon thermal transport in carbon nanotubes and graphene. *Phys. Rev. B*, 81(20):205441, 2010.

[220] J. Tersoff. Modeling solid-state chemistry: Interatomic potentials for multicomponent systems. *Phys. Rev. B*, 39(8):5566–5568, 1989.

[221] W Sekkal, B Bouhafs, H Aourag, and M Certier. Molecular-dynamics simulation of structural and thermodynamic properties of boron nitride. *J. Phys. Condens. Matter*, 10(23):4975, 1998.

[222] Veena Verma, V K Jindal, and Keya Dharamvir. Elastic moduli of a boron nitride nanotube. *Nanotechnology*, 18(43):435711, 2007.

[223] F. Benkabou, M. Certier, and H. Aourag. Elastic properties of zinc-blende g a n, a l n and i n n from molecular dynamics. *Molecular Simulation*, 29(3):201–209, 2003.

[224] Shinichi Sawada and Noriaki Hamada. Energetics of carbon nano-tubes. *Solid State Commun.*, 83(11):917 – 919, 1992.

[225] Zhiguo Wang, Xiaotao Zu, Fei Gao, and William J. Weber. Atomistic simulations of the mechanical properties of silicon carbide nanowires. *Phys. Rev. B*, 77(22):224113, 2008.

[226] R. L. Zhou, L. Wang, and B. C. Pan. Elastic and melting properties of crystalline sic nanotubes. *J. Phys. Chem. C*, 114(18):8199–8205, 2010.

[227] A.R. Setoodeh, M. Jahanshahi, and H. Attariani. Atomistic simulations of the buckling behavior of perfect and defective silicon carbide nanotubes. *Computational Materials Science*, 47(2):388 – 397, 2009.

[228] Steve Plimpton. Fast parallel algorithms for short-range molecular dynamics. *J. Comput. Phys.*, 117(1):1 – 19, 1995.

[229] Igor Žutić, Jaroslav Fabian, and S. Das Sarma. Spintronics: Fundamentals and applications. *Rev. Mod. Phys.*, 76(2):323–410, Apr 2004.

[230] S. A. Wolf, D. D. Awschalom, R. A. Buhrman, J. M. Daughton, S. von Molnar, M. L. Roukes, A. Y. Chtchelkanova, and D. M. Treger. Spintronics: A Spin-Based Electronics Vision for the Future. *Science*, 294(5546):1488–1495, 2001.

[231] S. A. Wolf, D. D. Awschalom, R. A. Buhrman, J. M. Daughton, S. von Molnr, M. L. Roukes, A. Y. Chtchelkanova, and D. M. Treger. Spintronics: A spin-based electronics vision for the future. *Science*, 294(5546):1488–1495, 2001.

[232] N. Müller, W. Eckstein, W. Heiland, and W. Zinn. Electron spin polarization in field emission from eus-coated tungsten tips. *Phys. Rev. Lett.*, 29(25):1651–1654, Dec 1972.

[233] G. Baum, E. Kisker, A.H. Mahan, W. Raith, and B. Reihl. Field emission of monoenergetic spin-polarized electrons. *Applied Physics A: Materials Science & Processing*, 14(2):149–153, 1977.

[234] Daniel T. Pierce and Felix Meier. Photoemission of spin-polarized electrons from gaas. *Phys. Rev. B*, 13(12):5484–5500, Jun 1976.

[235] Shaogang Hao, Gang Zhou, Jian Wu, Wenhui Duan, and Bing-Lin Gu. Spin-polarized electron emitter: Mn-doped gan nanotubes and their arrays. *Phys. Rev. B*, 69(11):113403, Mar 2004.

[236] Shaogang Hao, Gang Zhou, Jian Wu, Wenhui Duan, and Bing-Lin Gu. Spin-polarized electron current from mn-doped closed zigzag gan nanotubes. *Chemical Physics Letters*, 401(1-3):47 – 51, 2005.

[237] U von Barth and L Hedin. A local exchange-correlation potential for the spin polarized case. i. *Journal of Physics C: Solid State Physics*, 5(13):1629, 1972.

[238] G. Kresse and J. Hafner. Ab initio molecular dynamics for liquid metals. *Phys. Rev. B*, 47(1):558–561, Jan 1993.

[239] RE Peierls. Quantum theory of solids. 1955.

[240] Krishnan Raghavachari and J. S. Binkley. Structure, stability, and fragmentation of small carbon clusters. *The Journal of Chemical Physics*, 87(4):2191–2197, 1987.

[241] Seong Gon Kim, Young Hee Lee, Peter Nordlander, and David Tomnek. Disintegration of finite carbon chains in electric fields. *Chemical Physics Letters*, 264(3-4):345 – 350, 1997.

[242] S.C. Lim, D.S. Lee, H.K. Choi, I.H. Lee, and Y.H. Lee. Field emission of carbon-nanotube point electron source. *Diamond and Related Materials*, 18(12):1435–1439, 2009.

[243] A. Lorenzoni, H. E. Roman, F. Alasia, and R. A. Broglia. High-current field emission from an atomic quantum wire. *Chemical Physics Letters*, 276(3-4):237 – 241, 1997.

[244] Daniel Forney, Patrick Freivogel, Michel Grutter, and John P. Maier. Electronic absorption spectra of linear carbon chains in neon matrices. iv. c[sub 2n + 1] n=2–7. *The Journal of Chemical Physics*, 104(13):4954–4960, 1996.

[245] X.F. Fan, L. Liu, J.Y. Lin, Z.X. Shen, and J.L. Kuo. Density Functional Theory Study of Finite Carbon Chains. *ACS nano*, 3(11):3788–3794, 2009.

[246] Á. Rusznyák, V. Zólyomi, J. Kürti, S. Yang, and M. Kertesz. Bond-length alternation and charge transfer in a linear carbon chain encapsulated within a single-walled carbon nanotube. *Phys. Rev. B*, 72(15):155420, Oct 2005.

[247] A. Lucotti, M. Tommasini, M. Del Zoppo, C. Castiglioni, G. Zerbi, F. Cataldo, C.S. Casari, A. Li Bassi, V. Russo, M. Bogana, and C.E. Bottani. Raman and sers investigation of isolated sp carbon chains. *Chemical Physics Letters*, 417(1-3):78 – 82, 2006.

[248] M. Bianchetti, P. F. Buonsante, F. Ginelli, H. E. Roman, R. A. Broglia, and F. Alasia. Ab-initio study of the electromagnetic response and polarizability properties of carbon chains. *Physics Reports*, 357(6):459 – 513, 2002.

[249] K. S. Novoselov, A. K. Geim, S. V. Morozov, D. Jiang, Y. Zhang, S. V. Dubonos, I. V. Grigorieva, and A. A. Firsov. Electric Field Effect in Atomically Thin Carbon Films. *Science*, 306(5696):666–669, 2004.

[250] C. Oshima and A. Nagashima. Ultra-thin epitaxial films of graphite and hexagonal boron nitride on solid surfaces. *Journal of Physics: Condensed Matter*, 9:1, 1997.

[251] Claire Berger, Zhimin Song, Xuebin Li, Xiaosong Wu, Nate Brown, Ccile Naud, Didier Mayou, Tianbo Li, Joanna Hass, Alexei N. Marchenkov, Edward H. Conrad, Phillip N. First, and Walt A. de Heer. Electronic Confinement and Coherence in Patterned Epitaxial Graphene. *Science*, 312(5777):1191–1196, 2006.

[252] J. Stangl, V. Holý, and G. Bauer. Structural properties of self-organized semiconductor nanostructures. *Rev. Mod. Phys.*, 76(3):725–783, Sep 2004.

[253] Guy Furdin. Exfoliation process and elaboration of new carbonaceous materials. *Fuel*, 77(6):479 – 485, 1998. Presented at the Third Symposium on Coal Structure, 1996.

[254] Gengchiau Liang, N. Neophytou, D.E. Nikonov, and M.S. Lundstrom. Performance projections for ballistic graphene nanoribbon field-effect transistors. *Electron Devices, IEEE Transactions on*, 54(4):677 –682, 2007.

[255] John Cumings and A. Zettl. Field emission and current-voltage properties of boron nitride nanotubes. *Solid State Communications*, 129(10):661 – 664, 2004.